Enhancing Electron Transfer at the Protein/Electrode Interface: Applications in Bioderived Solar Energy Conversion and Electrochemical Biosensors

By

Evan Alexander Gizzie

Dissertation

Submitted to the Faculty of the

Graduate School of Vanderbilt University

in partial fulfillment of the requirements

for the degree of

DOCTOR OF PHILOSOPHY

in

Chemistry

May 2017

Nashville, Tennessee

Approved:

John A. McLean, Ph.D.

Eva M. Harth, Ph.D.

G. Kane Jennings, Ph.D.

David E. Cliffel, Ph.D.

For my family

ACKNOWLEDGEMENTS

This work would not have been possible without generous support from the Vanderbilt community. I would first like to acknowledge my advisor and mentor, Dr. David Cliffel, who accepted me into his research group and continually provided support and guidance during my time at Vanderbilt. I truly appreciate the many things he does to mold unrefined graduate students into critical thinking scientists.

I was very fortunate to have landed in such an embracing environment. From the onset of my career as a graduate student I interacted with many brilliant colleagues that helped to shape my development as a scientist. I am forever grateful for the infinite insights provided by peers, and later peer-mentors: Dr. Gabriel LeBlanc and Dr. Danielle Kimmel.

Dr. LeBlanc introduced me to the topic Photosystem I and trained me extensively in the research lab, but more importantly, inspired within me a passion for this unique project. His hard work undoubtedly paved the way for my research success and I owe him immensely.

Dr. Kimmel has been a great colleague and friend. Her knowledge and experience have become a guiding light for me. Her willingness to offer help with any challenge, science related or otherwise, is greatly appreciated. I am grateful for her guidance, generosity, and coarse sense of humor.

Additional group members in the Cliffel lab have been instrumental in me reaching this point in my career. Dr. David Crisostomo, Adam Ryan Travis, Aaron Daniel, Dr. Matt Casey, and Dr. Gongping Chen have been fantastic coworkers that always made themselves available for stimulating scientific discussions, help with

experiments, reviewing manuscripts, critiquing presentations, and even engaging in conversations about life, philosophy, politics, or (almost always) sports.

The entire Photosystem I project operates in a very team oriented way. I was fortunate enough to have Dr. G. Kane Jennings as a co-mentor. His kind guidance and advice during my time on the project will be appreciated forever. Also, many students in his group were key in many of the new discoveries presented in this dissertation. The efforts of Max Robinson, Siyuan Yang, and Faustin Mwambutsa are acknowledged.

Financial support for this research was provided by the National Science Foundation (DMR 0907619, EPS 1004083, DMR 1507505), the U.S. Department of Agriculture (2013-67021-21029) the Environmental Protection Agency (SU-83528701, SU-83602201), and the Research Corporation for Science Advancement. Additional support was provided by Vanderbilt University in the form of Mitchum E. Warren and Frederic LeRoy Conover Graduate Research Fellowships.

A close circle of friends has served as a true support group for me over the last five years. Beginning in my first year, I was taken in by a group of wiser, more mature graduate students that facilitated my transition into graduate school. Dr. Chris Gulka, Dr. Daniel Hermanson, Dr. Jay Forsythe, Dr. Matt O'Reilly, and Dr. Stephen Jackson were accomplished Vanderbilt Chemistry graduate students who have gone on to become distinguished professionals in their respective fields, and all were subscribers to the "work hard, play hard" mentality. I am forever thankful for their help in understanding the importance of work-life balance.

Contrary to popular belief, I have found time for other activities outside of the research lab. I feel very lucky to have been surrounded by such amazing people. Wes

Bauer and Thomas Struble, and later Andrew Kantor, have been outstanding roommates and friends. These men represent the upper echelon of class and dignity.

It is important for me to acknowledge Wes as a model graduate student whose hard work and long hours have been very inspiring. He has always been a valuable resource for me, and our many scientific discussions have been immensely helpful. He is a gentleman and scholar. Wes has also been a cornerstone member of my graduate school Wolf Pack, which is also comprised of Dr. Sarah Stow and Dr. Nichole Lareau, I am very thankful for them and the many other auxiliary members of the Wolf Pack such as Dr. Joseph Zackular and Dr. Jeannie Camarillo. Mike Turo is a great scientist, true friend, and has been a brother-in-arms since the very first day of orientation.

A few select friends back in Florida (Ray, Jared, and Julia) have always been supportive of my continuing education, and for that I am forever thankful. Although I've gotten some teasing from Ray for staying in school so long, these five years in Nashville have provided plenty of time for me to host their weekend trips. I have always enjoyed the distraction.

I feel honored to have served as player-coach-captain of the Vanderbilt Chemistry intramural volleyball team for several seasons. Although that ever-elusive IM championship has continually escaped our grasp, I can proudly say that I have played with some elite volleyballers and chemists including Dr. Kim Fong, Dorothy (aka "Dorth Vader", aka "D-Day", aka "Thundergun") Ackerman, and Mark Fulton.

The entire Vanderbilt community is established to foster innovation in many different ways. Many times, I have been a lucky beneficiary of the collaborative spirit of the Vanderbilt Chemistry department. In our highly interdisciplinary field, I have often

found my research project veering far outside of my area of “expertise”. It was during times like this that I would reach out to a colleague for guidance. Many successes, including work presented in this dissertation, can be directly attributed to those fantastic collaborators. I would like to acknowledge many of these colleagues, most of which have grown into dear friends: Dr. Jeremiah Beam, Dr. Keersten Ricks, Dr. J. Scott Niezgoda, Andrzej Balinski, and Dr. Don Stec. Additionally, the Vanderbilt Institute for Nanoscale Science and Engineering (VINSE) has been an incredible resource. The state-of-the-art facilities and world-class support staff of VINSE have made this work possible.

Although there have been plenty of stressful moments, I have enjoyed the time spent at Vanderbilt. I could not have done it without my graduate school family. Many thanks for the countless individuals that have helped me on this journey.

TABLE OF CONTENTS

DEDICATION iii

ACKNOWLEDGEMENTS iv

LIST OF FIGURES ix

LIST OF TABLES xii

Chapter

I. INTRODUCTION 1

II. EXPERIMENTAL METHODS 10
General Protocol for Extraction of Photosystem I from Spinach 10
Preparation of PSI Monolayer and Multilayer Films 12
Electrochemical Analysis of PSI Films 13

III. ELECTROCHEMICAL PREPARATION OF PHOTOSYSTEM I-POLYANILINE COMPOSITE FILMS FOR BIOHYBRID SOLAR ENERGY CONVERSION 15
Introduction 15
Experimental 18
Results and Discussion 21
Conclusions 33

IV. BIOHYBRID SOLID-STATE PHOTOVOLTAICS DERIVED FROM PHOTOSYSTEM I-POLYANILINE COMPOSITES 34
Introduction 34
Experimental 39
Results and Discussion 41
Conclusions 48

V. *IN SITU* CHEMICAL MODIFICATION OF THYLAKOID-BOUND PHOTOSYSTEM I FOR THE PREPARATION OF ORIENTED PROTEIN FILMS ON ELECTRODE SURFACES 50
Introduction 50
Experimental 56
Results and Discussion 59
Conclusions and Future Directions 62

VI. SILICON-BASED SOLID-STATE PHOTOSYSTEM I PHOTOVOLTAIC DEVICES 69
Introduction 69

Experimental 75
Results and Discussion 78
Conclusions and Future Directions 83

VII. LOW RESOURCE PHOTOSYSTEM I EXTRACTION AND ULTRA-FACILE BIOHYBRID DEVICE FABRICATION 85
Introduction 85
Experimental 88
Results and Discussion 90
Conclusions and Future Directions 93

VIII. OSMIUM POLYMER BASED ELECTROCHEMICAL BIOSENSORS FOR ORGAN-ON-CHIP SYSTEMS 95
Introduction 95
Experimental 101
Results and Discussion 105
Conclusions and Future Directions 111

IX. CONCLUSIONS AND OUTLOOK 113

REFERENCES 119

Appendix

A. NANOELECTRODE FABRICATION 135
Introduction 135
Experimental 140
Results and Discussion 144
Conclusions and Future Directions 146

B. PHOTOSYSTEM II EXTRACTION AND CHARACTERIZATION 149
Introduction 149
Experimental 149
Results and Discussion 152

LIST OF FIGURES

1.1 Structure and Energy Levels of Plant Photosystem I....3

3.1 Schematic Cross-section of PAni-PSI Film on Gold and Representative Photochronoamperometry....22

3.2 Potential Energy Diagram of PAni-PSI Composite System on Gold....23

3.3 Scanning Electron Micrographs of Pristine and PSI-loaded PAni Films....24

3.4 Polymerization Time – Photocurrent Relationship of PAni-PSI Films....25

3.5 Polymerization Time – Film Thickness Relationship of PAni-PSI Films....26

3.6 Photocurrent Density of PAni-PSI Film Prepared with Varying PSI Concentrations....28

3.7 PSI Protein Density in PAni-PSI Composite Films....30

3.8 Long-term Performance of PAni-PSI Composite Films on Gold Electrodes....32

4.1 Energy Diagram of Solid-State PAni-PSI Photovoltaic Device....38

4.2 Effect of Polymerization Time of Film Optical Density and Device Efficiency....41

4.3 Scanning Electron Micrograph Cross-section of Solid-State PAni-PSI/TiO_2 Device....42

4.4 Energy Dispersive X-Ray Spectroscopy Elemental Maps of a Typical Ag/PAni-PSI/TiO_2 Solid-State Device....43

4.5 I-V Curves of Ag/PAni-PSI/TiO_2 Solid-State Devices....44

4.6 Action Spectra of Ag/PAni-PSI/TiO_2 and Ag/PAni/TiO_2 Devices....45

4.7 Comparison of PAni-PSI/TiO_2 Devices with Ag, Au, and Al Cathodes....47

4.8 Longevity Study of Ag/PAni-PSI/TiO_2 Device....48

5.1 Competing Electrochemical Processes Derived from Oppositely Oriented Photosystem I Complexes....51

5.2 Strategy for Side-Selective Thiolation of PSI....55

5.3 Thiol/P700 Ratio for Modified PSI as Determined by Ellman's Assay....60

5.4 Photoactivity of Self Assembled Films of Native and Traut's-modified PSI.....61

5.5 Proposed Analysis of PSI Orientation by Scanning Electrochemical Microscopy 66

6.1 Band Energy Alignment Between p-Doped Si and Photosystem I.....70

6.2 CPCD Deposition of ZnO on PSI/p-Si and Representative Cross-section of ZnO/PSI/p-Si Device 72

6.3 Structures of Methyl Viologen and Poly(methylviologen).....74

6.4 Reaction Scheme for the Synthesis of Poly(p-xylylviologen).....75

6.5 Fabrication Strategy for Solid-State pSi/PSI/PxV Solid-State Devices 77

6.6 Cyclic Voltammogram of Poly(p-xylylviologen).....79

6.7 ^{1}H-NMR for Poly(p-xylylviologen).....80

6.8 Relative Energy Levels and Performance of p-Si/PSI/PxV/ITO Solid-State Devices 82

7.1 Outline of Low Resource Photosystem I Extraction.....87

7.2 SDS-PAGE of PSI Extracted with Low Resource Method 92

8.1 Redox Processes of Traditional and "Wired" Enzymatic Glucose Sensors. 98

8.2 Modified Screen Printed Electrode in Flow Chamber.....101

8.3 Cyclic Voltammogram of Os-polymer Modified SPE.....105

8.4 Multianalyte Titration of Oxidase Osmium-Hydrogel Sensors and Simultaneous Calibration Curves 107

8.5 Long-term Stability of Os-based Glucose and Lactate Sensors.....108

8.6 Air Saturated and Oxygen-free Glucose Calibrations 110

A.1 Sealing of Platinum Wire for Fabrication of Platinum Nanoelectrodes 138

A.2 Flame-assisted Carbon Nanoelectrode Fabrication 139

A.3 Sealed Quartz/Platinum Microform.....141

A.4 Micrograph of Tapered Platinum Wire after Laser Pulling.....141

A.5 Thermal Deposition of Pyrolytic Carbon in a Pulled Quartz Electrode 143

A.6 Size Determination of Platinum Nanoelectrode by Cyclic Voltammetry.....145

A.7 Micrograph of Tapered Multibarrel Quartz Capillary 147

B.1 SDS-PAGE of PSII Extracted from Spinach Leaves 152

B.2 Oxygen Evolution Assay for Extracted PSII.....153

LIST OF TABLES

4.1 Performance of PAni-PSI devices and PAni-only devices 44

7.1 Comparison of Results between PSI Extraction Types 90

Chapter I

INTRODUCTION

For billions of years, life on Earth has been sustained energetically by the Sun. Plants and other autotrophs rely on solar radiation for generating cellular energy, and in turn, these organisms become an energy source for higher organisms. While the Sun represents a seemingly infinite source of energy for life cycles, human societies have become increasingly dependent on non-renewable resources to meet growing electricity demands. Exponential world population growth has led to increased global energy demand and placed uncertainty in the future of non-renewable, status quo energy resources. This area of need was recognized by the U.S. Department of Energy and in 2011 the SunShot Initiative was established with the direct goal of reducing the solar-to-electricity costs to \$0.09 kWh^{-1} for residential photovoltaics by 2020.[1]

Since the onset of this undertaking, great strides have been made toward this goal; however, many challenges still exist. One such approach involves utilizing lower cost, environmentally benign materials for the construction of photovoltaic (PV) devices. Currently, silicon is the most widely used PV material, and although elementally abundant, the purification and fabrication of solar grade silicon wafers requires high energy input. This energy cost not only leads to increased financial burdens (and longer payoff times), but also relies on the consumption of fossil fuels for processing. To shift away from further fossil fuel dependence, new naturally abundant materials that require

minimal processing are necessary for creating low-cost solar energy conversion technologies.

Nature provides invaluable insight for effective solar energy conversion. Photosynthesis is the complex biological process by which green plants and other autotrophs utilize sunlight to generate cellular energy. Conversion of solar radiation into chemical energy is powered by two key proteins, Photosystem II (PSII) and Photosystem I (PSI), that act in series as pseudo-biological photodiodes. Following billions of years of environmental stimuli, these two proteins are highly evolved to operate with internal quantum efficiencies near unity.[2] Additionally, these proteins are conserved across many widely available green plant species, can be extracted using simple methods, and retain robust photoactivity *ex vivo*. For these reasons, the two supermolecular complexes have garnered much attention for use in bioderived photovoltaics.[3–5]

Photosystem I is of particular interest due to its innate stability. Upon photoexcitation, an electron-hole pair forms within the protein, and through a series of internal electron transport steps, electrons are shuttled from the luminal to stromal side of the thylakoid membrane. Figure 1.1A presents a structure of PSI, with the relative positions of the cofactors involved in internal electron transport.

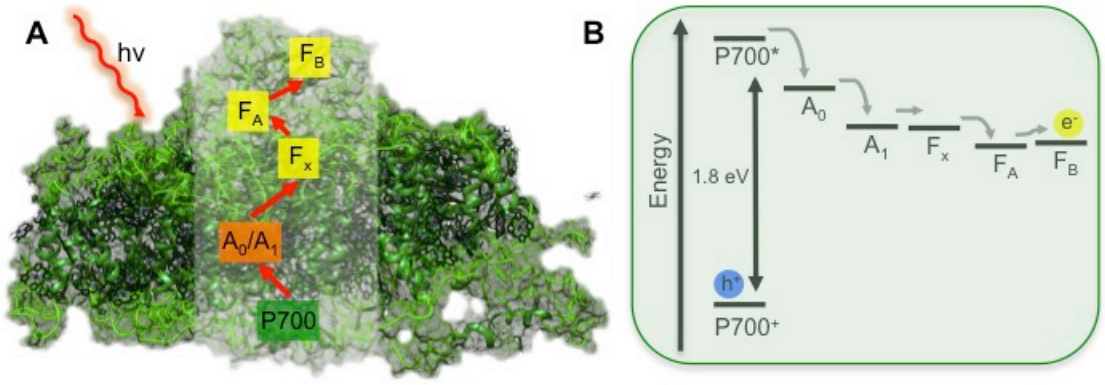

Figure 1.1. Structure and Energy Levels of Plant Photosystem I. The structure of PSI (PDB entry 2O01) is presented with approximate locations of internal redox mediators (A) along with the corresponding relative potential energies (B).

The photoactivtation process is initiated upon photoabsorption through the antenna chlorophyll network. Excited state energy transfer occurs to generate an exciton at a "special-pair" chlorophyll dimer, denoted at P700, buried within the protein. From here, an electron-hole pair rapidly forms and the excited electron is transferred from P700* to the primary and secondary internal electron acceptors A_0 and A_1. Three iron-sulfur clusters (F_x, F_A, and F_B) on the stromal side of the protein act as the terminal intra-protein electron acceptors and mediate the donation of electrons to exogenous acceptors; *in vivo* this acceptor is the metalloprotein, ferrodoxin.

PSI's intrinsic ability to rapidly generate charge separation and induce charge migration allows this protein to act as a standalone photovoltaic device. Thus, extracted PSI may represent an ideal, abundant, and naturally occurring material that could replace many costly materials in traditional photovoltaic cells. Early PSI-based research focused on proof-of-concept studies to demonstrate the viability of PSI-sensitized metallic electrodes.[6–10] Additionally, PSI has been explored as a photoabsorber to drive biological hydrogen generation.[11–16] Continual development of PSI electrodes focused on the

construction of devices capable of generating an appreciable amount of photocurrent, and through the construction of thick PSI films,[17,18] and use of semiconducting electrodes,[19,20] photocurrent output for biohybrid devices reached the μA cm^{-2} regime.

Although PSI is intrinsically stable *ex vivo*, it is a highly optimized biomolecule with a very specific native function, which presents unique challenges in utilizing this protein outside of its native environment. Uniquely, the electron transport step from F_B^- to an electrode surface is considered a rate-limiting slow step that ultimately restricts the efficiency of PSI-based photovoltaic devices.

This dissertation presents several unique strategies to improve interfacial electron transport between protein and electrode. Chapter 3 presents the development of a novel class of polymer-protein composites that can be rapidly prepared *in situ* on an electrode surface. The conductive polymer in this work (polyaniline, PAni) can easily mediate electron transfer, while also providing a three dimensional protective scaffold for protein immobilization. Proof-of-concept work is presented for PAni-PSI composites on gold electrodes in which film preparation was optimization to yield robust, PSI-loaded, conductive polyaniline films that produce photocurrents densities over 5 μA cm^{-2}. In Chapter 4, this novel polymer-protein composite material was applied to an energetically ideal semiconducting substrate, TiO_2 (Chapter 4). Once PAni-PSI was deposited on TiO_2, a metallic cathode was evaporated on the PAni-PSI side opposite the semiconductor to yield a simple, solid-state PSI-based photovoltaic device. This unique solid-state PSI device produced superior external quantum efficiency (0.009%) compared to previous PSI solid-state technologies. Additionally this device represents the current state-of-the-

art for PSI solid-state photovoltaics in terms of device performance longevity, cost, and ease of fabrication.

In addition to preparing composite materials to mediate the electron transfer between protein and electrode, there is also substantial interest in orienting the protein on electrode surfaces to uniformly direct charge transport across that interface. *In vivo* PSI is naturally oriented in the "upright" position, and the arrangement of its internal electron transport chain invariably directs electron transfer from lumen to stroma. However, once extracted from the thylakoid membrane for use in a semi-artificial biohybrid photovoltaic device, orientation control is lost. Thus, for oppositely oriented PSI supercomplexes at an electrode interface, charge separation occurs in opposite directions and the competing electrochemical reactions will yield a net electron transfer of zero, i.e. no photocurrent or photovoltage.

Chapter 5 addresses this issue by introducing an *in situ* functionalization scheme to side-selectively modify the membrane bound protein with simple amino acid-specific chemistries. This strategy utilizes the intact lipid bilayer to restrict the transport of coupling reagents to the luminal side of PSI. In this work, a short-chain thiol was selected as the linker molecule to modify stromal-side lysine residues. Thiolation on a single side of PSI allows for exploitation of the high-affinity gold-thiol bond to direct self-assembly of PSI into "inverted" films on gold electrodes, with the stromal side F_B cluster oriented at the electrode interface. Spectroscopic characterization revealed a large quantity of new thiols (ca. 40) introduced to the PSI supercomplex using this method. Additionally, self-assembled films of modified PSI on gold electrodes produced approximately 3-fold more photocurrent than unmodified PSI films, indicating improved electronic interaction

between protein and electrode. Additional studies are ongoing to 1) characterize the spatial distribution of the protein modification sites and 2) analyze orientation uniformity of the modified PSI complexes following self-assembly.

The highest reported photocurrent for PSI electrodes were achieved by LeBlanc et al. in 2012 with the introduction of p-doped silicon as the electrode material.[19] However, this unique interface required a concentrated diffusional mediator solution, and thus did not represent a long-term solution for scalable PSI-based photovoltaics. Chapter 6 addresses this fundamental restriction by using p-doped Si/PSI electrodes as the basis for fabricating solid-state photovoltaic devices. Here, emphasis is placed on developing the PSI/cathode interface with the ultimate goal of constructing an electron-mediating layer that can accept electrons from thick PSI multilayers and donate to the underlying conducting substrates.

First, ZnO is presented as one such material that was deposited onto PSI multilayer films via Confined Plume Chemical Deposition. This process utilizes infrared laser pulses to decompose a ZnO precursor confined between the film and a glass slide without inducing damage to the underlying biological material. This novel photovoltaic device yielded a remarkable output of 127 $\mu A\ cm^{-2}$, and with two distinct semiconductor/protein interfaces, represents the first device of its kind. Although this device was unique in its architecture and performance, the specialty equipment required to prepare the ZnO layers does not readily scale, which hinders further device development. For this reason, an alternative class of electron-transport materials is explored in Chapter 6 as interfacial layers between PSI and conductive anodes. Polyviologens are unique redox-active polymers that have been shown to accept electrons

from photoabsorbers such as quantum dots. Herein, poly(p-xylylviologen) (PxV) was synthesized, characterized, and deposited onto PSI multilayers on p-Si to act as a dry electron mediating film. Rudimentary solid-state p-Si/PSI/PxV/ITO devices were fabricated and tested to validate the role of the polymer in electron transport. Further optimization of this class of polymers will give way to improved efficiency in low-cost, large-scale PSI-based photovoltaics.

One of the primary appeals of using PSI as the active component in solar cells is the low-cost and availability of the protein. Although major acheivements have been made in improving device efficiency through integration with more sophisticated materials, this also increases the relative cost basis of devices per cm^2. Chapter 7 presents a facile streamlined extraction procedure that can be performed in a low resource environment, such as a rural classroom or geographic outpost away from an existing power grid. This extraction was developed to demand minimal laboratory expertise and require very modest scientific equipment. As described in this protocol, the entire extraction takes under 2 h and yields a sufficient quantity of photoactive PSI. Gel electrophoresis revealed that the rapid PSI extraction was successful, albeit with a sacrifice of total purity for ease and rapidity. This new protocol introduces new opportunities for extraction PSI for educational purposes, as well as creating modular kits for field deployment to prepare extremely low-cost solar cells to power small electronics.

Finally, the improvement of electron transfer between enzymes and electrodes is explored for a different application: biosensors. Glucose oxidase is a widely used enzyme that is immobilized on an electrode for the amperometric detection of glucose in solution. Oxidase enzymes act by turning over their respective substrates, and then donating

electrons from the turnover to a secondary acceptor, via the enzymes' bound $FAD/FADH_2$ cofactors. In traditional enzymatic biosensors, electron mediation occurs via dissolved oxygen, which is detected amperometrically as peroxide at a platinum electrode. This oxygen-mediated system has significant drawbacks that limit their operation to select environments. Notably, these sensor types require large electrode bias (+0.6 V vs. Ag/AgCl) to oxidize peroxide, making them sensitive to redox-active interferents in complex biological media. These sensors rely on the presence of dissolved oxygen, which precludes their use in *in vitro* biological systems that seek to study cellular behavior in low-oxygen environments. To address these major drawbacks, Chapter 8 uses a class of redox-active, osmium-containing hydrogels that act as both an immobilization matrix for the enzyme, and mediate electron transfer from oxidase to the electrode surface.

These redox polymers were used to prepare analyte-specific films with glucose, lactate, and glutamate oxidases on a screen printed electrode array for the independent, simultaneous detection of glucose, lactate, and glutamate. This multianalyte system is ideal for real-time analysis of flow-based, *in vitro* analyses, such as Organ-on-Chip platforms. The Os-polymers are capable of turning over these oxidase enzymes at a lower oxidation potential (+0.2 V) than traditional oxidase-based biosensors. This reduced electrode bias avoids oxidation of amperometric interferents present in complex media. Acetaminophen (APAP), with a redox potential of approximately 0.35 V vs. Ag/AgCl, is a model interferent for this study based on its clinical relevance, acute hepatotoxicity, and known redox activity. Here, individual sensors on a screen printed electrodes were modified with Os-polymer and either glucose oxidase, lactate oxidase, or glutamate

oxidase. These sensors were then validated via flow-based titrations using a series of calibrants containing increasing concentrations of glucose, lactate, and glutamate in buffer with a background of 10 mM APAP. The reduced dependence of these sensors on dissolved oxygen was also demonstrated by titration in air-saturated and oxygen-free buffer samples. These unique redox polymers have been utilized for the first time in a multianalyte platform, which is ideal for coupling with an Organ-on-Chip system or bioreactor for improved *in vitro* analyses.

Chapter 2

EXPERIMENTAL METHODS

General Protocol for Extraction of Photosystem I from Spinach

Photosystem I was extracted from fresh spinach leaves using a protocol adapted from Reeves and Hall,[21] with additional purification steps reported by Shiozawa and coworkers.[22] In short, approximately 100 g of fresh spinach leaves (*Spinacia Oleracea*) were homogenized in a household blender along with 200 mL of chilled Grinding Medium (330 mM sorbitol, 10 mM sodium pyrophosphate, 4 mM calcium chloride, and 2 mM ascorbic acid). This mixture was then coarsely filtered through 2 layers of cheesecloth, then 8 layers of cheesecloth. The filtered solution was then divided into centrifuge tubes, and spun at 8000 x g for 1 min to precipitate chloroplasts. Membranes were disrupted by resuspending the pellet in surfactant-rich media The resuspending medium was comprised of 50 mM HEPES pH = 7.6, 330 mM sorbitol, 2 mM EDTA, 1 mM magnesium chloride, 1 mM manganese chloride, and 1% Triton X-100. Once resuspended, the solution was thoroughly mixed by vortexing to ensure that intact chloroplasts were ruptured, and the thylakoids within were fully lyzed.

The solution of solubilized membrane components was then divided into centrifuge tubes and centrifuged again at 20,000 x g for 15 min. Following centrifugation, the supernatant containing solubilized PSI was separated from the pellet. This material was then loaded onto a chilled, water-jacketed hydroxylapatite column equilibrated with 20 mM phosphate buffer (pH = 7.0). Separation was carried out on the crude extract by

continually washing with Column Buffer (20 mM phosphate buffer, pH = 7.0) to remove free pigments, excess surfactant, and other non-protein components, as PSI was retained on the stationary phase. Once thoroughly washed, purified PSI was eluted from the column using Elution Buffer (200 mM phosphate buffer, pH = 7.0, with 0.05% Triton X-100). This eluent was collected and aliquoted into approximately one hundred 1 mL aliquots which were frozen and stored at -80 °C for later use.

PSI samples collected using this method were characterized by Baba Assay.[23] In this assay, the active P700 concentration is determined spectroscopically based on the absorbance difference in chemically oxidized and reduced PSI samples. The oxidized sample was prepared by combining 2275 μL of Baba Assay buffer (50 mM Tricine pH = 7.8, 100 mM sorbitol, 10 mM sodium chloride, and 0.05% Triton X-100) with 100 μL of PSI stock, and 125 μL of 1 M ferricyanide. The reduced sample was prepared by combining 2275 μL of Baba Assay buffer with 100 μL of PSI, 5 μL of a reducing stock containing 500 mM sodium ascorbate and 5 mM dithiothreitol, and 120 μL of water. The differential absorbance spectrum between the two samples was collected from 650 – 750 nm. The absorbance value at the peak near 700 nm (with respect to the isosbestic point at 725 nm) was used along with the extinction coefficient of 64 $mM^{-1}cm^{-1}$, to calculate the active P700 concentration.

Extraction PSI samples routinely produced P700 concentrations of approximately 1 μM. Samples of this concentration were typically used without further concentration or dilution except where noted elsewhere.

Preparation of PSI Monolayer and Multilayer Films

Prior to deposition of any PSI films, excess buffer salts and surfactants were removed by dialysis. Briefly, PSI samples were removed from the -80 °C freezer and quickly thawed. The defrosted stock samples (ca. 1-4 mL) were then dialyzed against 3 L of DI water using 10 kDa cutoff dialysis tubing. The dialysis proceeded for a minimum of 18 h to ensure the removal of excess phosphate salts and surfactant. Once this process was completed, the dialyzed PSI solutions were used for deposition in variety of forms.

For monolayer films of PSI, gold electrodes were first cleaned with Piranha (3:1 sulfuric acid:hydrogen peroxide) to produce a pristine, hydroxyl terminated surface free of organic contaminants. The gold wafer electrodes (ca. 1 cm x 2 cm) were then placed upright in a 15 mL conical centrifuge tube such that the gold surface could not come into contact with the sidewalls of the vessel except at the very edges of the wafer. The dialyzed PSI solution was then added to the tube to cover the entire wafer. Using this method, the delicate gold surface was protected from abrasion via contact with the container, and the upright position of the substrate prevented large aggregates of protein from gravimetrically settling on the surface. PSI was left in the refrigerator to assemble onto the gold surface typically for 1-2 days to ensure total surface saturation.

For PSI multilayer films, a vacuum assisted method described by Ciesielski et al. was utilized.[18] Clean gold or silicon substrates, were first masked using electrochemical mask (Gamry Instruments) hole punched to yield an open area of 0.282 cm^2. Masked substrates were placed into a vacuum desiccator, and then 50 μL of a dialyzed PSI solution was dropcast inside the substrate mask. The desiccator was capped, and vacuum was applied for approximately 15 minutes to remove the solvent. This process produced

thin multilayer films of PSI, and the dropcast and evaporation steps were repeated as needed to achieve a film of desired thickness.

Electrochemical Analysis of PSI Films

Monolayer and multilayer films of PSI on Au or Au/Si wafer electrodes were analyzed using a homebuilt electrochemical cell. This acrylic cell featured a liquid reservoir (ca. 2 mL) with a bored hole on the side of the cell over which the wafer was placed. An O-ring was sandwiched between the cell opening and wafer to generated a liquid-tight seal. A clamp was used to secure the wafer tightly against the cell. In this apparatus, the electrodes were restricted to a working area of 0.2 cm^2. The liquid reservoir was used to hold electrolyte mediator solutions for photoelectrochemical experiments.

A CHI 660A potentiostat was used for all electrochemical analysis, except where noted otherwise. For the three-electrode setup, the PSI modified wafer was connected as the working electrode, a platinum mesh wire was defined as the counter electrode, and a Ag/AgCl electrode was used as the reference. For two-electrode experiments, the PSI modified electrode was assembled as the working electrode, and the counter and reference lead wires were connected to the opposing electrode in the device.

In a traditional photochronoamperometric experiment, the current response over time under light and dark conditions was monitored. First, the open circuit potential (OCP) of the system was recorded in the dark for 60 s. The equilibrium dark OCP determined at the end of the 60 s trial, represents the external potential required to the negate any dark current flow in the device. In the subsequent photochronoamperometric experiment, the predetermined OCP was input as the working electrode bias. This ensures

that any current recorded during the illumination experiment is attributed only to photoactivated electron transfer events. In a typical photochronoamperometric experiment, the total experiment duration was set for 60 s, with a sampling frequency of 10 s^{-1}. During the first 20 s of the experiment, the sample was kept in the dark to establish a current baseline. At t = 20 s, the sample was illuminated for a duration of 20 s. Finally the sample returned to dark baseline when the lamp was turned off at t = 40 s, and remained in the dark for the remainder of the experiment. The reported photocurrent for each PSI electrode was determined by averaging the middle 20 data points from the steady-state region of the i-T curve.

Chapter 3

ELECTROCHEMICAL PREPARATION OF PHOTOSYSTEM I–POLYANILINE COMPOSITE FILMS FOR BIOHYBRID SOLAR ENERGY CONVERSION[a]

Introduction

Photosystem I (PSI) is one of the key enzymatic components of photosynthesis in green plants and other autotrophs. Billions of years of environmental stimuli have evolved this ~500 kDa protein supercomplex into nature's most efficient photodiode, with *in vivo* charge separation efficiency near unity.[24–26] Along with its vast natural abundance, ease of extraction, and robustness, PSI has attracted significant attention from researchers who aim to integrate the protein into highly efficient, biohybrid solar energy conversion devices.[5,27] This field of research is based upon the need to construct biohybrid electrodes and ultimately stand-alone photovoltaic devices utilizing the biological material, PSI, as the principle photoactive component. As opposed to current, state-of-the-art photovoltaics such as semiconductor photodiodes or dye-sensitized solar cells, PSI-derived devices offer advantages such as low-cost, readily abundant materials, simple processing, and scalability. For these reasons, the PSI-based photovoltaics have been widely researched in recent decades as sustainable solar energy conversion alternatives to traditional solar avenues.

Early work with PSI relied on solution-phase self-assembly of the protein on functionalized gold electrodes.[6,28,29] In subsequent work, the manual drop casting of thick

[a] Portions of this chapter are taken in part from Gizzie, E. A.; LeBlanc, G.; Jennings, G. K.; Cliffel, D. E. Electrochemical Preparation of Photosystem I - Polyaniline Films Composite Films for Biohybrid Solar Energy Conversion. *ACS Appl. Mater. Interfaces* **2015**, *7*, 9328–9335.

protein films on gold substrates proved to significantly enhance the photocurrent yields of biohybrid PSI electrodes. By increasing the overall protein loading on the surface of the electrode, multilayer PSI assemblies on traditional electrode materials are capable of achieving photocurrent densities that are significantly larger than those observed from single PSI monolayers. Current densities for PSI multilayer assemblies are often observed in the μA cm^{-2} regime;[17] however, performances are limited based on competing electrochemical processes introduced by the lack of orientation specificity associated with thick, drop cast films.[30] Moving forward in the development of the "next-generation" biohybrid photovoltaic materials, it is of extreme importance to improve the interfacial electron transfer pathways. Thus in this work, a photoactive composite material that fully incorporates PSI as its active component is constructed to facilitate the electron transfer from enzyme to electrode while circumventing the issues of poor electron transfer, aggregation and orientation. Improving the electron transfer pathways, from enzyme to electrode, is of extreme importance in development and further enhancement in biophotovoltaic devices.

The concept of immobilizing Photosystem enzymes on polymer-functionalized electrodes has demonstrated improved electron transfer by directing electron flow from enzyme to electrode through the conductive film.[31,32] Incorporating the protein into a redox-active polymer network has attracted significant attention, due not only to the improved electron transfer, but also the increased enzyme loading in the three dimensional network, de-emphasis on uniform protein orientation, and extension of enzyme lifetime.[3] Redox-active hydrogels constructed from poly(N-vinylimidazole) backbones loaded with transition metal complexes (i.e. osmium-bis(2,2'-bipyridine)-

dichloride) have been utilized for the immobilization of PSI,[33] and also for PSII,[34] with both cases producing photocurrent densities that greatly surpassed the previous performance of protein multilayers on gold. Loading hydrogels with transition metal complexes of osmium, ruthenium, or cobalt significantly enhances the electron diffusion coefficients through the film.[35] However, metal coordination compounds (specifically that of osmium) are very costly to prepare and thus are not a viable solution for scalable biohybrid, solar energy technologies. Additionally, two recent publications have demonstrated the utility of polymer-immobilized PSI devices.[36,37] However, in each case drawbacks exist from costly materials and/or extensive processing, thus these emerging technologies prohibitively lack scalability. In this work, carbon-based polymers are explored as conductive matrices for the immobilization of PSI, to expand upon recent advances in PSI composite materials.

Aside from redox-active hydrogels, there exists a class of intrinsically conductive polymers, which are categorized by their π-conjugated backbones. Polyaniline (PAni) is one such material known specifically for its low-cost, high conductivity, environmental stability, and ease of electrochemical preparation under mild aqueous conditions.[38] Other enzymes, such as glucose oxidase, have been successfully incorporated into electroactive polymers (via an electropolymerization mechanism) for use in highly specific biosensors.[39,40] Thus we have theorized that entrapment of PSI within a conductive PAni network is possible by co-electropolymerization aided by hydrogen bonding between aniline oligomers and various amino acid side chains found on the surface of the PSI supercomplex.

In this work, composite PAni-PSI films were prepared via electropolymerization from a single solution containing both aniline and PSI. These composite films were then evaluated electrochemically to verify the entrapment of PSI in the PAni network, and the retention of enzymatic activity following the entrapment process. The optimized PAni-PSI composites in this study produced external quantum efficiency near 0.005%, which is comparable to first generation PSI multilayers. However, these newly developed PAni-PSI composites were 10-fold thinner and contained 70-fold less protein material than a traditional drop cast PSI multilayer film. Based on the successful incorporation of an active and functioning form of the protein supercomplex, the scope of this work extends far beyond the construction of photoactive composites for photovoltaic applications. To our knowledge this is the first instance of successful integration of very large (>500 kDa) biomolecules, specifically integral membrane proteins, into polymer films via a rapid, controllable, surfactant-stabilized co-electropolymerization from aqueous media. The applications of this processing extend into other arenas of bionanotechnology, biomaterials, and biosensing.

Experimental

Preparation of Photosystem I-Polyaniline Composites on Gold Electrodes

For all electrochemical experiments, PAni and PAni-PSI composite films were deposited on 2 mm gold disk electrodes (area = 0.031 cm^2), which were first polished using a series of alumina powder slurries from 1 to 0.05 micron in order to obtain a smooth electrode surface, which was confirmed with an optical microscope (Olympus BX41) at 500x magnification. After polishing, the electrodes were sonicated in distilled water for a minimum of 15 min to remove any alumina powder adsorbed on the gold

surface. Electropolymerization was performed using a CH Instruments 660A electrochemical workstation three-electrode set-up with a platinum mesh counter electrode and Ag/AgCl (3M KCl) reference electrode.

For the evaluation of the polymerization time – photocurrent relationship, the PAni-PSI composite films were prepared in 1 M aniline (Fisher), 0.941 M HCl, 4 mM sodium phosphate, 0.3 μM PSI, and 0.01% (w/v) Triton X-100. The PAni control films were prepared in 1 M aniline, 0.941 M HCl, 4 mM sodium phosphate, and 0.01% (w/v) Triton X-100. At a fixed electropolymerization potential (+1.2 V vs. Ag/AgCl) the deposition time was modulated between 10-120 s, resulting in an array of film thicknesses.

For the PSI concentration study, electrodes were modified in an electropolymerization solution containing 1 M aniline, 0.941 M HCl, 4 mM sodium phosphate, and 0.01% Triton X-100. The concentration of PSI was varied between 0 – 0.3 μM. Electropolymerization was carried out at +1.2 V (vs. Ag/AgCl) for a fixed deposition time of 40 s.

For comparative purposes, PSI multilayer films were prepared. Using the previously published methods of Ciesielski et al,[18] a single 60 μL aliquot of a 1.6 μM PSI solution was drop cast onto each gold electrode. The samples were then dried under vacuum at room temperature, leaving a thin PSI film approximately 200 nm in thickness.

In order to evaluate the long-term stability of PAni-PSI films, three sample composite films were prepared potentiostatically, as described above, at +1.2 V vs. Ag/AgCl for 40 seconds. These films were prepared from a solution of 1 M aniline, 0.941 M HCl, 0.3 μM PSI, 4 mM sodium phosphate, and 0.01% Triton X-100. Three traditional

PSI films (~200 nm thick) were also prepared, as described above, for comparison to the PAni-PSI composites in the long-term study.

Film Characterization

Scanning Electron Microscopy (SEM) images were collected with a Hitachi S4200 high-resolution scanning electron microscope. The film thickness of each sample was determined using stylus profilometry, where the average step height between the underlying gold and top layer of the PAni-PSI film was recorded using a Veeco Dektak™ 150 stylus profilometer.

Electrochemical Analysis

The photoactivity of PAni controls, PAni-PSI composite films, and PSI multilayers were evaluated using photochronoamperometry with a CH Instruments 660A electrochemical workstation with a Faraday cage, equipped with a three electrode setup containing a platinum mesh counter electrode and Ag/AgCl (3M KCl) reference electrode. This three-electrode electrochemical setup allows for the evaluation of the anodic half-reaction occurring at the working electrode independent of the platinum mesh auxiliary (counter) electrode.

Photochronoamperometry experiments were carried out in 100 mM KCl (Sigma-Aldrich) with 5 mM sodium ascorbate (Sigma-Aldrich) as an electron donor and 250 μM 2,6-dichlorophenolindophenol (DCPIP) (Sigma) to catalyze the turnover of the sodium ascorbate electrolyte. The potential of the working electrode was set to the measured dark open circuit potential. The current response was then measured upon illumination of the sample with a 250W light source equipped with a 633 nm high pass filter (Leica KL 2500 LCD lamp). For each chronoamperometry trial, the reported steady state photocurrent

was sampled 10 seconds after initial illumination. External quantum efficiency was calculated for the best performing PAni-PSI composite films based on maximum photocurrent density.

In the case of the long-term stability study, the photocurrent of each replicate was sampled daily over the course of three weeks in order to monitor the day-to-day change in photocurrent.

Quantification of PSI in PAni Film

PAni/PSI films were grown electrochemically at +1.2 V for 40 s on gold electrodes, from a solution of 1 M aniline, 0.941 M HCl, 0.3 μM PSI and 4 mM sodium phosphate. Pristine PAni films were grown in an identical manner, but in the absence of PSI. Following polymerization, films were dissolved in a minimal amount of concentrated nitric acid (Fisher, TraceMetal™ Grade), and then diluted to 5% nitric acid with 18.2 MΩ-cm deionized water.

Samples were then analyzed for iron using a Perkin-Elmer Optima 7000 Inductively Coupled Plasma Optical Emission Spectrometer, calibrated for iron emission at 238.204 nm. For quantification, a three-point calibration was constructed from Fe standards (SPEX CertiPrep) ranging from 0 – 50 ppb in 5% nitric acid.

Results and Discussion

To ensure that the PSI supercomplexes were entrapped and had retained photoactivity following electropolymerization, photochronoamperometry was performed. Figure 3.1A depicts a cross-section of the composite film containing entrapped PSI within the conductive polymer network. Figure 1B represents the typical photoresponse for a PAni-PSI composite film (shown in red) with an overlay for a PAni control film

(shown in blue). For comparison, a PSI multilayer film of comparable thickness was prepared (shown in orange).

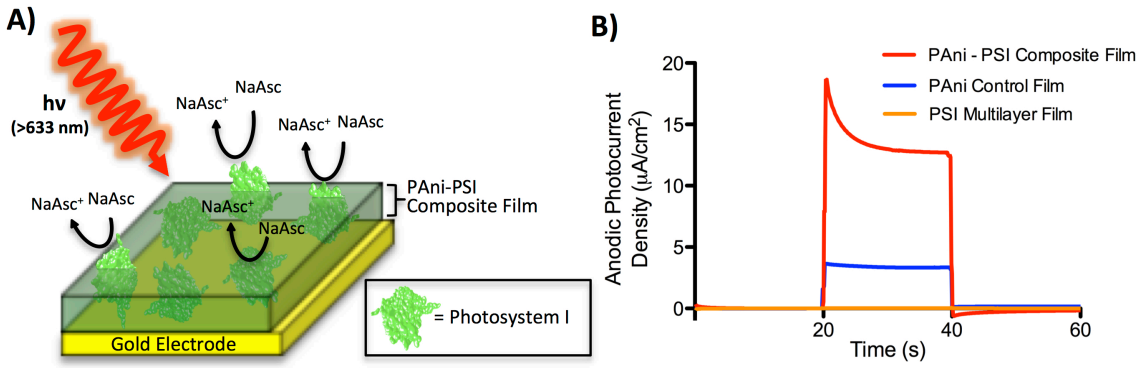

Figure 3.1. Schematic Cross-section of PAni-PSI film on Gold and Representative Photochromoampermetric Performance. A) Cross-section of a PAni-PSI composite film deposited onto a planar gold electrode, where sodium ascorbate (NaAsc) acts as a sacrificial electron donor. B) Sample current-time plots for a PAni-PSI composite film, PAni film containing no PSI, and a traditional PSI multilayer film of similar thickness (~180 nm). Electrochemical analyses were performed in aqueous media containing 5 mM sodium ascorbate, 250 μM DCPIP, and 100 mM KCl as supporting electrolyte. In every trial, each sample was held at its dark open circuit potential, and illuminated from 20-40 s.

The photocurrent density of 0.03 μA cm^{-2}, produced by the traditional multilayer, pales in comparison to the PAni-PSI composite film. The PAni-PSI composite film yields a dramatic increase in photocurrent density over the multilayer assembly.

Polyaniline has been studied in organic thin-film solar cells as a hole-conducting material,[41] and the photoactivity observed in this study is in agreement with such behavior. The delocalized positive charges on the polymer backbone act as strong electron acceptors,[42] thus requiring the rapid donation of electrons from another material (i.e. PSI or sodium ascorbate) to sustain steady photocurrent output in a photovoltaic device.

In the PSI-loaded samples, illumination results in photoactivated charge separation at the internal P700 site, which drives an electron through the protein until it

reaches the iron-sulfur cluster located on the stromal side of PSI. This process is depicted in the potential energy diagram of Figure 3.2.

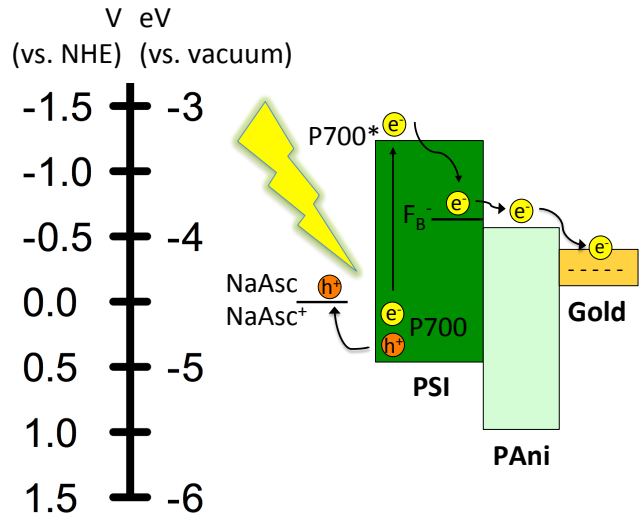

Figure 3.2. Potential Energy Diagram of PAni-PSI Composite System on Gold. When illuminated, exciton formation and charge separation occur at the P700 site, from which the electron is passed via internal mediators until reaching the conductive PAni and subsequently the underlying gold anode. PSI cofactor energies were previously reported in Ref. 24 and the band energies of PAni were determined experimentally via voltammetry.

To effectively prevent charge recombination within the protein, sodium ascorbate acts as a sacrificial electron donor by donating an electron to the $P700^+$ hole. From the rapid decay in photocurrent occurring immediately after initial illumination (Figure 3.1B) it is clear that mediator diffusion is the limiting factor in this system. This rapid decay can be modeled as Cottrell-like behavior, resulting from a diffusion-limited system. From the reduced iron-sulfur cluster, F_B^-, the electron is accepted by the PAni network and traverses through the film until it reaches the gold substrate electrode, resulting in an anodic photocurrent. The consistent polarity of the photocurrent between PSI-loaded films and PAni films indicates that the protein is acting synergistically with

the polymer network to create a photoactive, biohybrid composite film capable of producing a significant enhancement in photocurrent density.

The process of electrochemical polymerization produces relatively smooth films, which can be characterized using Scanning Electron Microscopy (SEM). Images of a pristine PAni film and PSI-loaded PAni film are presented in Figure 3.3. As expected the pristine film is smooth and generally featureless, however under the same preparation conditions, the film prepared in the presence of solubilized PSI resulted in an observable increase in roughness based on the encapsulation of protein in the polymer network.

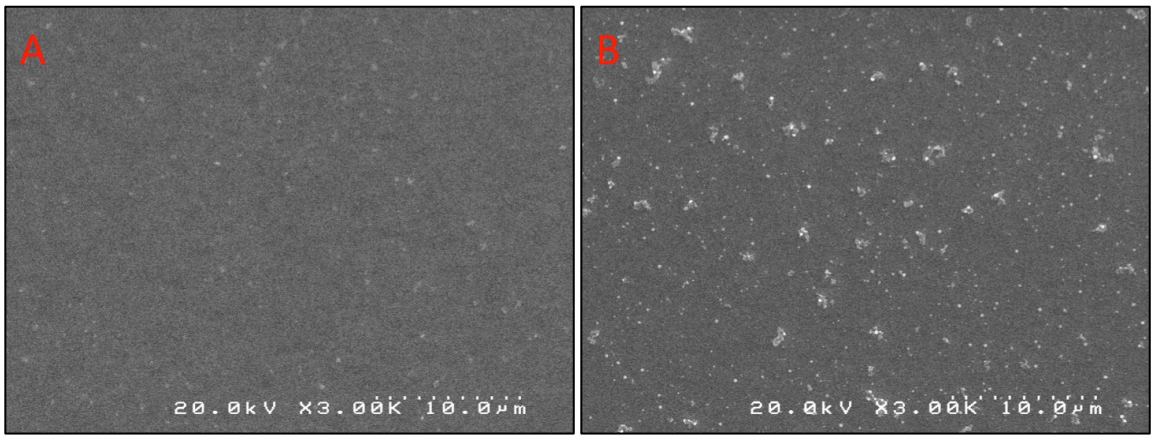

Figure 3.3. Scanning Electron Micrographs of Pristine and PSI-loaded PAni Films. Pristine PAni (A) and PAni/PSI composite (B) films prepared via electrochemical polymerization of aniline in the presence of PSI.

Present in the PAni/PSI film (Figure 3.3B), but not the pristine PAni (Figure 3.3A) are a large number of bright clusters, attributed to the embedded PSI protein aggregates in the film. The incorporation of this iron-sulfur containing protein, into a conductive organic film has resulted in a larger quantity of reflected electrons observed by the SEM. The size of these clusters is approximately 50-500 nm. The dimensions of extracted PSI are predicted to be 8.5 nm x 12 nm as estimated by previous studies,[43–45] thus a small degree of protein aggregation has occurred during the entrapment process.

Due to the potentiostatic deposition method utilized in the preparation of these films, we can study the affect of film thickness on the total photocurrent output simply by modulating the polymerization time of the composite films. Figure 3.4 depicts this relationship as pristine PAni films (shown in blue) and PAni-PSI composite films (shown in red) were prepared using polymerization times ranging from 20-120 s.

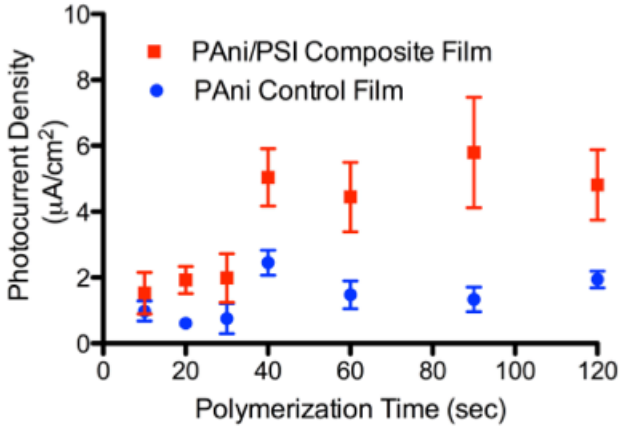

Figure 3.4. Polymerization Time – Photocurrent Relationship of PAni-PSI Films. Effect of polymerization time for PAni-PSI composites (red) and PAni control (blue) films. PAni-PSI films were prepared from a fixed PSI concentration of 0.3 μM. Each data point represents the average and standard error of six replicates sampled 10 s after initial red light illumination in an electrolyte solution of 100 mM KCl, 5 mM sodium ascorbate, and 250 μM DCPIP.

As expected, an enhancement in observed photocurrent occurs as the polymerization time increases. Over the polymerization times of 10 – 30 seconds, photocurrent output is low, approximately 2 μA cm^{-2}, and can be attributed to two key factors: the marginal optical absorbance of the thin film and the minimal quantity of entrapped PSI over the brief polymerization time. As polymerization time is increased to 40 s the photocurrent output of the composite film increases dramatically to ~5 μA cm^{-2}, indicating that (in comparison to the shorter polymerization times) either a larger quantity

of protein has been entrapped or the optical density of the film is increasing as a result of film growth.

To better understand this system it becomes important to construct a model by which polymerization time affects the film thickness of PAni. A comprehensive study was performed to correlate polymerization time to a coupled film thickness. As presented in Figure 3.5 it can be observed that rapid film growth occurs linearly from 10-40 s until a terminal thickness of approximately 200 nm is reached.

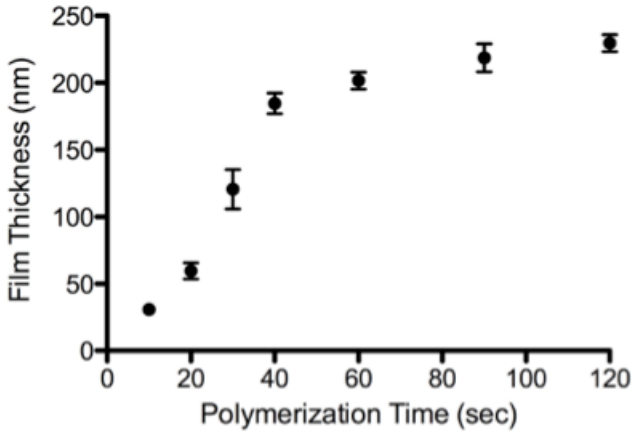

Figure 3.5. Polymerization Time – Film Thickness Relationship of PAni-PSI Films. Correlation of potentiostatic polymerization time and the subsequent film thickness of PAni-PSI films as determined by stylus profilometry. Each data point represents the average and standard error of three replicate samples at each deposition time.

Over the 10 – 40 second span in Figure 3.5 we are able to utilize linear regression analysis to accurately construct a growth equation for PAni films, as depicted below in Equation 3.1, where t is the polymerization time in seconds.

$$\text{Film thickness (nm)} = (5.2 \pm 0.4)t - (32 \pm 12) \qquad (3.1)$$

The terminal thickness achieved for this system is attributed to several factors including the high monomer and surfactant concentrations in the polymerization solution. Alternatively, the adoption of potentiometric polymerization methods should allow for thicker PAni films, as previously demonstrated in several studies using a variety of

electrode materials.[46,47] It is also worth noting that the time associated with PAni-PSI film preparation is significantly shorter than the methods previously used to prepare PSI films on solid substrates, which utilized a vacuum-assisted "drop-cast" method requiring at least 15 minutes of deposition time per ~400 nm layer of protein.[18]

After analyzing the data for film thickness with polymerization time and photocurrent output with polymerization time, it becomes apparent that the photocurrent generation of these composites follows closely with the film growth mechanism of the PAni. This is particularly evident in low photocurrent density for the 10 – 30 second samples, and the plateau in photocurrent density of the thickest composite films prepared in this study, approaching the terminal 200 nm thickness. At times below 40 seconds, the preparation time is too short to entrap an appreciable amount of solubilized PSI, thus minimal currents are observed that barely outperform the PAni controls. However, beyond this 40-second threshold, films are considerably thicker and have more time to envelope the protein in this conductive network.

After exploring the relationship between film thickness and polymerization time, the effect of PSI concentration present in the aniline solution during electropolymerization was optimized (Figure 3.6). For this experiment, a single deposition time was selected, 40 s (at +1.2 V vs. Ag/AgCl) corresponding to a film thickness of 185 ± 13 nm at each concentration of PSI.

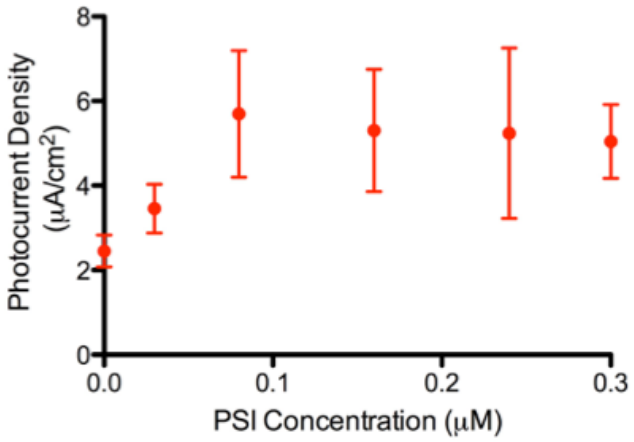

Figure 3.6. Photocurrent Density of PAni-PSI Film Prepared with Varying PSI Concentrations. PAni-PSI composites were prepared from different solutions with varying concentrations of PSI. Each data point corresponds to the average and standard error of six replicates at each PSI concentration.

A rise in photocurrent density occurs as the protein concentration in the deposition solution is increased until a maximum is reached at 0.1 μM PSI. Shortly after reaching that maximum, the net photocurrent response plateaus, which identifies that above this critical concentration threshold the PSI uptake does not increase. Specifically, beyond the 0.1 μM concentration threshold the photocurrent output is dictated by the time-dependent entrapment and film growth, but not the overall PSI concentration in the polymerization solution surrounding the electrode.

After identifying the best performing PAni-PSI electrode optimized for film thickness and initial PSI concentration, the external quantum efficiency (EQE) of this film was explored. The EQE is a useful value for analyzing the performance of photoactive materials by directly correlating the electron generation (or current density) relative to photon flux incident on the substrate. In this case, we can determine the EQE for the best performing PAni-PSI film from the photocurrent output of 5.0 ± 0.9 μA cm^{-2}

produced at a red light intensity of 189 mW cm^{-2}. Using these parameters, external quantum efficiency was calculated, as shown below in Equation 3.2:

$$\frac{Photocurrent\ Electrons}{Incident\ Photon\ Flux}\ x\ 100 = \frac{Current\ Density\ (A\ cm^{-2})/_{e}}{Power\ Density\ (W\ cm^{-2})/_{E_{\lambda}(J)}}\ x\ 100 \qquad (3.2)$$

Where, e is the elementary charge and E_λ is the photon energy, at 633 nm. Thus the EQE for our films was calculated to be 0.0052 ± 0.0009%. Although, other devices have reported efficiencies approaching 0.1% by relying heavily on the photovoltaic properties of semiconducting substrates,[20] the efficiency reported in the PAni-PSI film is comparable to the previously calculated values for thick PSI multilayer films on gold electrodes,[18] while operating with a PAni-PSI active layer that is 10-fold thinner than a PSI multilayer film.

Although the photocurrent output and efficiency produced in these newly developed PAni-PSI films fall short of the current benchmark performance of PSI multilayers on p-Si electrodes (approximately 200 μA cm^{-2} when normalized for mediator concentration),[19] our method presents superior advantages in reduced cost and film preparation time. PAni-PSI films do not rely on expensive, high-purity silicon wafers or a thick protein layer of non-specifically bound PSI to generate photocurrent. In addition to providing a novel method for the assembly of large molecular weight proteins into conductive polymer films, we have now produced a new completely organic, composite material that can be interfaced with other electronic materials to create next generation solar devices that are low-cost, scalable, and stable.

In addition to the electrochemical analyses presented above, it becomes necessary to analytically quantify the amount of protein entrapped during the electropolymerization process. Based on the known stoichiometric ratio of Fe atoms

(found in iron-sulfur clusters F_X, F_A, and F_B) to PSI, inductively coupled plasma optical emission spectroscopy (ICP-OES) was able to correlate trace amounts of Fe entrapped in the PAni/PSI composite films to a PSI protein density in the film (Figure 3.7). In this study, the best performing PAni-PSI films, prepared from 40 s polymerization in a solution containing 0.3 μM PSI, were digested in nitric acid and analyzed for Fe content.

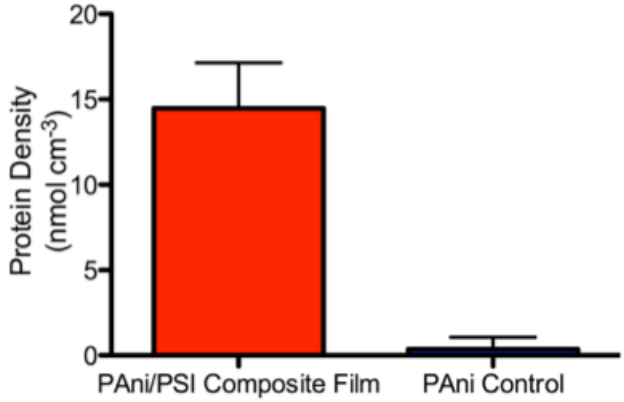

Figure 3.7. PSI Density in PAni-PSI Composite Films. The atomic iron content of PAni-PSI (red) and pristine PAni control films (blue) were determined using ICP-OES. From the known stoichiometric ratio of Fe in each PSI supercomplex, the quantity of entrapped PSI was calculated. Error bars represent the standard error of three replicates.

By quantifying the Fe content through its unique atomic emission, the stoichiometric ratio of Fe to PSI (12:1) was used to directly quantify the amount of PSI in each film. Further, using the film radius and thickness (185 nm), a cylindrical volume model was used to calculate a protein density in each film: 14.5 ± 2.7 nmol cm^{-3} for the PAni/PSI film, and 0.4 ± 0.7 nmol cm^{-3} for the pristine PAni film. For comparison, a well-packed traditional PSI multilayer film would produce a PSI density of approximately 1 μmol cm^{-3}. Thus, with approximately 1.5% of the overall PSI content of a traditionally packed multilayer film, a PAni-PSI film produces significantly more photocurrent. This enhancement can be attributed largely to the vastly improved electron transport pathway from protein to electrode through the conductive PAni matrix.

With direct quantification of PSI present in the PAni-PSI composite films, we can now calculate the ensemble turnover of the enzyme within the film and ensure that appreciable activity of the enzyme is conserved. By treating our film as an enzymatic system, dictated by Michaelis-Menten kinetics,[33] we may calculate turnover frequency, where k_{cat} is defined as the maximum rate (photocurrent flux, C/s) contributed only from the PSI, divided by the quantity of PSI in the film (Equation 3.3).

$$k_{cat} = \frac{V_{max}(^{C}/_{s})}{molecules\ of\ PSI} \times \frac{1\ electron}{1.602\ x\ 10^{-19}\ C} \qquad (3.3)$$

Thus, using the known quantity of PSI entrapped in a typical film (as determined by Inductively Coupled Plasma – Optical Emission Spectroscopy, ICP-OES) and the photocurrent contribution from PSI in that film, turnover frequency was calculated to be 1.4 ± 0.5 electrons s^{-1} PSI^{-1}. This value is in good agreement with those determined by Manocchi et. al. in 2013,[48] where PSI layers were deposited onto alkanethiol-modified gold electrodes for electrochemical analysis.

In the case of traditional PSI films, on gold or p-doped silicon, the film durability is limited due to the fundamental nature of non-specific, electrostatic binding of protein on the electrode surface, thus creating a potential drawback of such devices. Here it is theorized that encapsulation of PSI within a conductive polymer network, as performed in this work, provides superior performance longevity in photocurrent output over time. To address the issue of long-term film stability, the photocurrent output of PAni-PSI composite films was evaluated over 16 days (Figure 3.8). The long-term performance of simple PSI multilayers and pristine PAni films were also tracked over the same time span as represented in Figure 3.8.

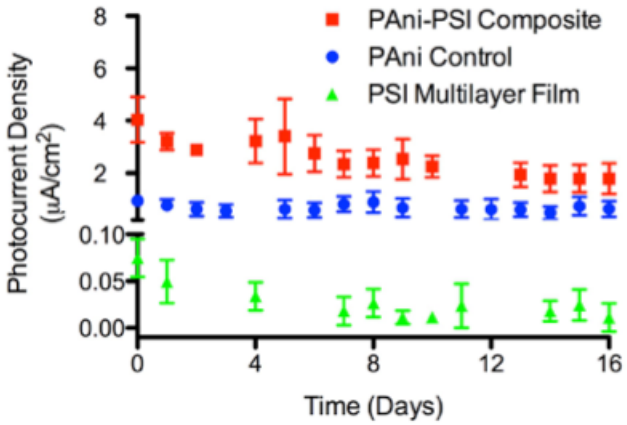

Figure 3.8. Long-term Performance of PAni-PSI Composite Films. Stability of PAni-PSI composites (red), pristine PAni films (blue), and traditional PSI multilayer films (green), as tested once daily over a period of 16 days. Each point represents the average and standard error of three replicates of the respective sample type.

From the initial sampling, the photocurrent density produced by the PSI-loaded PAni film (shown in red) was much higher than that generated by the PAni control films, or the traditional PSI multilayer films. The PAni-PSI composite film consistently yielded a steady photocurrent output, near 2 μA cm^{-2}, although a drop in photocurrent occurred following the initial photoelectrochemical evaluation on day 0. The PAni control film (shown in blue) produced marginal photocurrents, approximately 1 μA cm^{-2} over the course of the trial, which was significantly lower than the PSI-loaded PAni film during this span. For the traditional PSI film, after initial exposure to aqueous media, the protein film begins to visually degrade, as is expected for a multilayer of electrostatically bound protein. The photocurrent density produced by the PSI multilayer samples (shown in green) was significantly lower than that produced by the PAni-PSI films and the PAni control. From the onset of the trial, the output of the PSI multilayer films bottomed out near 0.01 μA cm^{-2}. In comparison to the traditional PSI multilayer film, the PAni-PSI composites still represents nearly a 200-fold improvement in photocurrent after three

weeks. This long-term performance indicates that polyaniline is an effective immobilization matrix for enhancing the lifetime of PSI biohybrid electrodes.

Conclusions

The PAni-PSI composite films prepared here introduce a rapid assembly method for integrating large molecular weight photoactive proteins into conductive polymer networks using mild electrochemical polymerization conditions without loss in enzymatic activity. A significant enhancement in photocurrent was observed for the PSI-loaded films over the PAni control films. The greatest enhancement was seen in the 185 nm thick PAni-PSI films prepared with 0.3 μM PSI in the polymerizations solution. These photocurrents (5.7 μA cm^{-2}) represent a vast improvement over multilayer PSI films of comparable thickness while incorporating 1000-fold less protein material, and rapidly assembling on a much shorter time scale. This research presents future avenues for work that incorporates PSI into conductive polymer networks, including the use of alternative substrate materials in biohybrid photovoltaic devices.

Chapter 4

BIOHYBRID SOLID-STATE PHOTOVOLTAICS DERIVED FROM PHOTOSYSTEM I-POLYANILINE COMPOSITES[b]

Introduction

The conversion of solar radiation into electricity has been integral in the effort to develop novel alternative energy solutions. Photosynthesis provides a uniquely efficient platform for the development of new solar energy conversion systems and has subsequently spawned a plethora of research strategies to develop bioinspired materials, catalysts, devices, and cell architectures to replicate the efficiency achieved in nature.[4] Alternatively, achievements have been made in directly extracting and utilizing the photoactive proteins that drive photosynthesis. Photosystem I (PSI) is a protein complex that, upon photoexcitation, generates an electron-hole pair with near unity quantum efficiency.[49] Based on this remarkable efficiency and the unidirectional electron transport vector of PSI, it has attracted attention as a biomolecular photodiode to be used in the fabrication of biohybrid photovoltaic electrodes.[3,5,27,50,51]

The development of plant based biohybrid electrodes was pioneered in the 1980's through the successful immobilization of photosynthetic components on electrodes. Agostiano et. al., in 1983, successfully immobilized PSII and PSI on platinum

---

[b]Portions of this chapter are taken in part from Gizzie, E. A.; Niezgoda, S. J.; Robinson, M. T.; Harris, A. G.; Kane Jennings, G.; Rosenthal, S. J.; Cliffel, D. E. Photosystem I-polyaniline/TiO_2 Solid-State Solar Cells: Simple Devices for Biohybrid Solar Energy Conversion. *Energy Environ. Sci.* **2015**, *8* (12), 3572–3576.

as one of the first examples presenting the viability of a semi-artificial photosynthetic device.[52] Additional pioneering work was achieved by Katz et. al. in which immobilization methods were developed for the covalent attachment and alignment of photosynthetic reaction centers on PtO,[53] and later pyrolytic carbon,[54] for directed electron transport from protein to electrode. In addition to this work, Greenbaum et. al. provided major breakthroughs with the chemical platinization of intact chloroplasts,[55] and later with isolated PSI,[43] for photodriven bio-hydrogen production. Based on these fundamental studies, subsequent decades of research have been dedicated to the creation of artificial photosynthetic devices and biohybrid electrodes as effective bio-derived solar energy conversion platforms.

When incorporated into a traditional biohybrid electrode, photoexcitation of the bound antenna chlorophylls of PSI causes an excited state energy transfer, that results in electron hole pair formation at the "special pair" chlorophyll dimer (denoted as P700) located in the interior of the protein.[56] Following charge dissociation, the excited electron is transported internally through a series of phylloquinone mediators until reaching the terminal [4Fe-4S] iron-sulfur clusters. At the final iron-sulfur cluster, F_B, an electron of -3.9 eV with respect to the vacuum level is accepted by an artificial electrochemical mediator, such as methyl viologen. Concurrent to this process, a hole is transported away from the oxidized $P700^+$ center by an electrode to reduce the special pair and turn over the system for subsequent energy transfer.

In previous generation PSI-based bioelectrodes, protein films were assembled onto metallic substrates in monolayer or multilayer forms acting as a photoactive material for direct photocurrent generation.[6,18,48,57] These biohybrid electrodes were able to

produce photocurrent densities in the μA cm^{-2} regime when coupled with an appropriate diffusional redox mediator. Through the use of semiconductor electrodes, it has been shown that favorable electron transfer is produced by the alignment between energy bands of a carefully selected semiconductor and PSI. In 2012, both LeBlanc et al.[19] and Mershin et al.,[20] demonstrated this concept by producing PSI-loaded p-doped silicon and ZnO electrodes, respectively. Performance greatly surpassed that which was previously achievable on metallic electrodes in both studies. Recently, hematite has also demonstrated particular utility as a narrow band gap semiconducting electrode material in pseudo-dye sensitized solar cells with PSI.[58] However, all of these devices have fundamental limitations, specifically the need for liquid diffusional mediators and the cost associated with the fabrication materials.

To alleviate the need for liquid electrolytes, PSI-based solar energy conversion strategies have shifted toward the development of solid-state photovoltaics, and away from wet-cell PSI-based devices. The initial feasibility of solid-state PSI films was demonstrated through the preparation of protein films on gold electrodes that retained photoactivity and electrochemical response under dry conditions.[9,29] In a study by Gordiichuk et al. in 2014, state-of-the-art solid-state biohybrid photovoltaic devices were prepared by assembling a monolayer of cyanobacterial PSI onto a TiO_2 substrate and backing the device with a polytriarylamine hole-conducting layer and MoO_3/Al cathode.[36] Those devices presented a novel breakthrough, but were limited by extensive processing, air sensitivity, and costly materials. To further enhance the performance, sustainability, and scalability of PSI solid-state photovoltaics, we have developed a novel PSI solar cell utilizing a solid polyaniline-PSI composite material as the photosensitizing

layer on a TiO_2 semiconductor anode and an evaporated Ag cathode. TiO_2 on FTO-coated glass was selected as the anodic material based on the favorable alignment of its conduction band with the terminal iron-sulfur cluster of PSI (Figure 4.1). Based on this energetic alignment, TiO_2 has demonstrated particular utility in previous studies with PSI modified electrodes.[20,59,60] Additionally, the low cost of TiO_2, ease of preparation, and transparency in the visible spectrum make it an ideal electrode material. However, previous PSI-modified TiO_2 electrodes, analogous to dye sensitized solar cells, are limited by the monolayer loading capacity of protein on the substrate.

In this study, PSI was entrapped within an electropolymerized polyaniline (PAni) film grown directly on the TiO_2 anode. This film deposition method creates a three-dimensional network of protein enveloped within a conductive matrix with high electron transport kinetics from enzyme to electrode. The photosensitizing PAni-PSI layer was prepared potentiostatically from the electropolymerization of aniline in the presence of solubilized PSI, purified from spinach leaves. The evaporation of a metallic cathode on the PAni-PSI/TiO_2 structure produced a low-cost solid-state photovoltaic device, prepared using facile methods with a bio-derived photoactive layer.

PAni has previously been shown to be an exceptional charge transfer material in redox mediated biohybrid cells.[61] For these devices, HCl-doped, emeraldine salt PAni was prepared as the polymeric matrix for the PSI films on TiO_2 due to its high conductivity and ease of preparation.[42] As compared to other conductive polymers, PAni represents the superior material for protein entrapment using electrochemical polymerization. Aniline is water soluble unlike most other organic monomers that are capable of electropolymerization. This film preparation method allows the material to act

as a solid conductor for electron transport while also providing a three-dimensional network for increased PSI-loading and light adsorption. Active PSI is entrapped in the polyaniline film during electropolymerization as represented by a protein density of approximately 15 nmol cm^{-3} determined previously via ICP-OES.

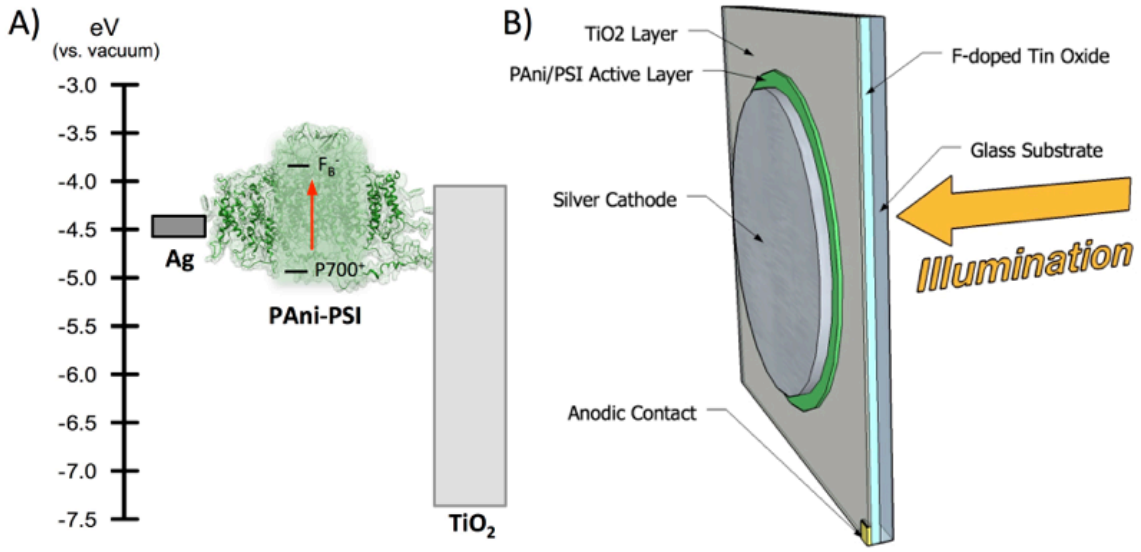

Figure 4.1. Energy Diagram of Solid-State PAni-PSI Photovoltaic Device. A) Energetic relationship between Photosystem I's energy cofactors (P700 and F_B), TiO_2 anode and silver cathode is presented. B) Schematic stack-up of the device. The silver cathode layer, PAni-PSI composite layer, and transparent TiO_2 layer on FTO/glass are labeled. Additionally, illumination through the anodic layer is depicted.

The energy diagram presented in Figure 4.1A shows the favorable energetic band alignment between the F_B site of PSI and the conduction band of TiO_2. The n-type anatase TiO_2 accepts electrons from the PAni-PSI composite with its conduction band at approximately -4.2 eV.[62] PAni plays a critical role in this device as it shuttles electrons from PSI to the anode through a chain hopping mechanism introduced by the mixed redox states of emeraldine salt polymer.[63] From the cathodic side of the device, the evaporated silver layer accepts and transports holes away from the oxidized $P700^+$ reaction center of the protein. In Figure 4.1B, a layered schematic is presented showing the complete device with silver cathode, PAni-PSI film, and transparent TiO_2 layer on an

FTO/glass substrate. Due to the inverted architecture of this device, the PAni-PSI photoactive layer is illuminated through the transparent anode.

Experimental

TiO_2 Electrode Preparation

TiO_2 substrates were prepared using a method adopted from a previously described protocol.[64] FTO coated glass substrates were cleaned with three 20-minute sonication cycles in 3% Triton X-100 in DI-water, acetone, and isopropanol, respectively. Cleaned FTO substrates were placed in a 50 mM $TiCl_4$ bath at 70 °C for 30 min. Following the bath, substrates were annealed in a tube furnace at 500 °C for 60 min. 0.155 g commercial TiO_2 paste (Dyesol 90-T) was diluted with 0.47 g ethanol and vortexed until fully dispersed. A spin coating procedure was then utilized in which 10 drops of the diluted paste were applied to the $TiCl_4$-treated FTO electrodes, while stationary, and allowed to spread. The electrode was then spun at 300 RPM for 5 seconds, followed by 1500 RPM for 45 seconds. After removing from the spin coater, an ethanol-soaked cotton swap was used to clear a corner of TiO_2 coating for an eventual contact to the underlying FTO. These electrodes were then placed on the center of a hotplate, set to 390 °C, for 30 min. A final $TiCl_4$ bath, identical to one previously mentioned, was used to treat the electrodes for 30 min at 70 °C. The electrodes were then washed thoroughly with DI water and dried under a stream of nitrogen. The samples were once again annealed with the same 500 °C tube furnace and stored for later use.

PAni-PSI Film Deposition

PAni-PSI films were prepared electrochemically from a single aqueous solution of 1 M aniline, 0.94 M HCl, 4 mM sodium phosphate, and 1.3 μM PSI. The stock

polymerization solution was prepared immediately before use. Using a CH Instruments 660A potentiostat, potentiostatic polymerization was carried out at +6.5 V for 120 seconds. In the three-electrode setup, the TiO_2 substrate was set as the working electrode (area = 1.54 cm^2) with a Pt mesh counter electrode and Ag/AgCl (3 M KCl) reference electrode. Following electrochemical film formation, the modified TiO_2 substrates were rinsed with copious amounts of DI water and dried under a stream of nitrogen.

Cathode Evaporation

The PAni-PSI modified devices were then placed face down in a custom mask for cathode evaporation that yields 0.071 cm^2 contact areas. The devices were loaded into an evaporator chamber of an Åmod deposition system (Ångstrom Engineering). Ag and Au deposition was achieved in a resistive evaporator chamber, while the Al deposition was performed with electron-beam ablation. For the Ag-only contacts, a 20 nm layer of Ag deposited at 0.2 Å/s was formed first, followed by a 280 nm Ag layer at 2.0 Å/s. For the Au contacts, a 20 nm layer of Au deposited at 0.2 Å/s was formed first, followed by a 280 nm Ag layer at 2.0 Å/s. Al-only contacts, formed in the e-beam chamber, began with a 20 nm layer of Al deposited at 0.2 Å/s, followed by a 280 nm Al layer at 2.0 Å/s.

Device Testing

I-V data was measured in ambient air with a custom LabView program run through a Keithley 2400 source-meter. The solar spectrum at AM1.5 was provided by a SolarTech xenon solar simulator to within class A spectral matching (less than 25% spectral mismatch). The lamp was calibrated to 1-sun with an NREL certified photovoltaic standard. An aperture was used to ensure illumination of only the contact

being measured, while a multiplexer filtered all cathodic leads but that of the illuminated contact.

Results and Discussion

In order to enhance the photocurrent output of the solid-state device the active layer thickness was increased by modulating the polymerization time of the PAni-PSI film. With the increased polymerization time, films with higher optical density are observed, as depicted in Figure 4.2.

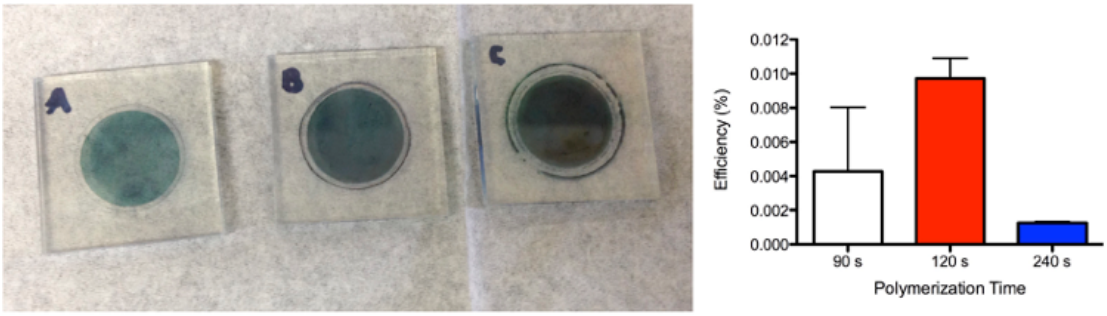

Figure 4.2. Effect of Polymerization Time of Film Optical Density and Device Efficiency. Left) Images of PAni-PSI films deposited on TiO2/FTO/glass substrates. Samples were prepared from potentiostatic polymerization at +6.5 V, for A) 90 s, B) 120 s, and C) 240 s. Right) Photovoltaic efficiency of Ag/PAni-PSI/TiO_2 devices prepared with active layer thicknesses polymerized for 90, 120, or 240 s.

As observed in Fig. 4.2, the increasing film thickness that results from the increasing polymerization time, increases the device external quantum efficiency as a thicker light absorbing active layer (with more PSI) is produced. However, as the film thickness increases beyond 120 s, a diminishing efficiency is observed. Thus 120 s was used as the ideal polymerization time in this work.

Using scanning electron microscopy (SEM) the device cross-section was imaged. Distinct layers were visually identified as the glass, FTO, TiO_2, PAni-PSI, and silver components of the device (Figure 4.3).

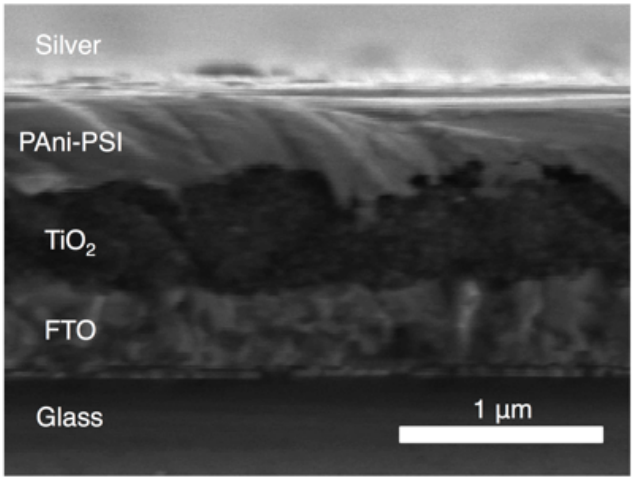

Figure 4.3. Scanning Electron Micrograph Cross-section of Solid-State PAni-PSI/TiO_2 Device. A typical cross sectional image of a PAni-PSI solid-state device as imaged by Scanning Electron Microscopy. Glass, FTO, TiO_2, PAni-PSI, and silver layers are labeled. Scale bar represents 1 µm.

The PAni-PSI layer was approximated to be 350 nm. The TiO_2 layer and FTO layer were determined to be 450 and 400 nm, respectively, which are consistent with the substrate preparation methods used in this study and elsewhere. The PAni-PSI active layer of 350 nm was prepared from 120 s of potentiostatic polymerization. A PAni-PSI composite layer of this thickness presumably reaches an optimum interplay between high optical density for maximum photon absorption while being thin enough to allow for efficient carrier diffusion in the film. Often observed in polymer-semiconductor devices with inverted architecture (similar to this device), a thick polymer active layer increases the hopping distance for holes to reach the cathode, thus diminishing photocurrent density and efficiency as the film thickness increases.[65]

The composition of each device layer was confirmed using EDS elemental mapping (Figure 4.4) thus verifying the solid-state device architecture.

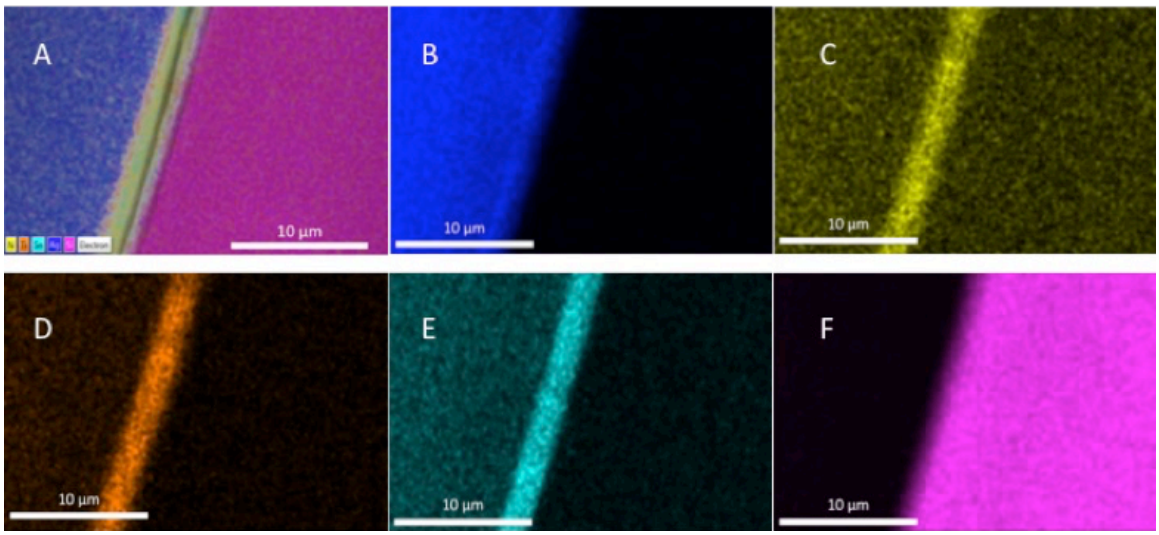

Figure 4.4. Energy Dispersive X-Ray Spectroscopy Elemental Maps of a Typical Ag/PAni-PSI/TiO_2 Solid-State Device. A) Composite image of device, and elemental maps for B) silver, C) nitrogen, D) titanium, E) tin, and F) silicon. All scale bars represent 10 µm.

The device architecture was confirmed through the use of SEM-EDS mapping. Figure 4.4B clearly presents silver, which represents the silver cathode of this solid-state device. Also shown Fig. 4.4C is a nitrogen-rich layer, corresponding to the presence of the nitrogen-containing polymer and the PSI protein. Below the PAni-PSI layer is the TiO_2 layer and FTO layer shown in Fig. 4.4D and 4.4E, respectively. Finally, Fig. 4.4F presents a silicon-rich sample indicative of the thick borosilicate glass layer of the device.

The Ag/PAni-PSI/TiO_2 solid-state devices were evaluated under solar simulation conditions. I-V curves for typical devices are shown in Figure 4.5. For the PAni-PSI devices, typical short circuit current densities (J_{SC}) of 72 µA cm^{-2} were observed. This average photocurrent density surpasses the previous state-of-the-art solid-state PSI photovoltaic device by nearly 250-fold.[36]

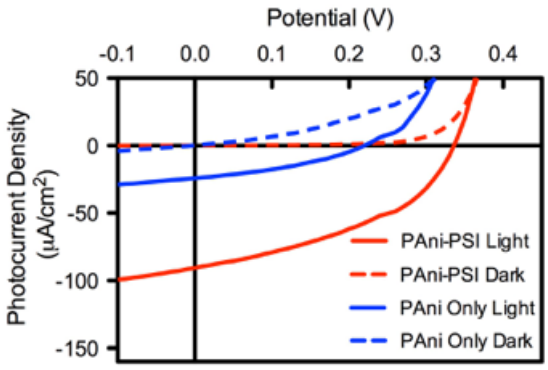

Figure 4.5. I-V Curves of Ag/PAni-PSI/TiO_2 Solid-State Devices. Using AM1.5 solar simulation conditions, Ag/PAni-PSI/TiO_2 and Ag/PAni/TiO_2 devices were tested.

In addition to the large photocurrent densities, the use of silver cathodes consistently produces open-circuit voltages (V_{OC}) of approximately 300 mV. As expected, the PAni-only devices (shown in blue) performed poorly, relative to the PSI-loaded devices. The photocurrent densities, open circuit potentials, and efficiencies of the PAni-only control devices were approximately 3-fold smaller than the PAni-PSI devices. Table 4.1 summarizes the performance metrics of J_{SC}, V_{OC}, fill factor, and external quantum efficiency (EQE) for the Ag/PAni-PSI/TiO_2 and Ag/PAni-only/TiO_2 devices.

Table 4.1. Performance of PAni-PSI devices and PAni-only devices. For each value, the average and standard error are reported.

Active Layer Type	Current Density, J_{SC} (μA cm^{-2})	Open Circuit Potential, V_{OC} (V)	Fill Factor	External Quantum Efficiency (%)
PAni-PSI (n = 13)	72 ± 3	0.299 ± 0.004	0.420 ± 0.007	0.0091 ± 0.0006
PAni-only (n = 16)	21 ± 7	0.100 ± 0.003	0.19 ± 0.05	0.0022 ± 0.0009

In order to validate the role of PSI in the solid-state devices, action spectra relating the illumination wavelength to quantum efficiency were collected for PAni-PSI and PAni-only solid-state devices. Using a Fianium Supercontinuum™ laser source, a

Ag/PAni-PSI/TiO_2 device was illuminated using monochromatic wavelengths raging from 383.5 – 740 nm, while I-V curves were collected at each wavelength selection. Internal Quantum Efficiency (IQE%) was calculated using Equation 4.1:

$$IQE\% = \frac{Current\ (A)\left(\frac{6.022 \times 10^{23} e^-}{mol}\right)\left(\frac{1\ mol}{96{,}485\ C}\right)}{\Theta_\lambda \cdot P\ (W) \cdot \frac{1}{E_\lambda}\left(\frac{photons}{J}\right)}\ x\ 100 \qquad (4.1)$$

Where θ_λ is the ratio of photons absorbed by the PAni-PSI film at the wavelength, λ, determined by the absorbance (A_λ) using the relationship, $\theta_\lambda = 1 - 10^{-A}$. P is the power of the laser in Watts at that specific wavelength, and E_λ is the energy of each photon at the same wavelength.

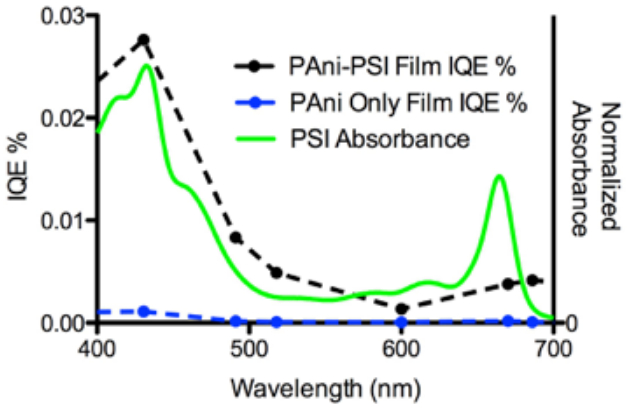

Figure 4.6. Action Spectra of Ag/PAni-PSI/TiO_2 and Ag/PAni/TiO_2 Devices. Internal Quantum Efficiencies for selected wavelength ranging from 400 – 700 nm are presented for PAni-PSI (black) and PAni-only control (blue) films. Comparatively, the normalized absorption spectrum for PSI is presented in green.

As observed in the action spectrum, a localized quantum efficiency minimum is found at between 550-625 nm, as is intrinsic of the poor absorption coefficient of PSI's antenna chlorophyll network in that range. Local IQE% maxima are observed near the 680 and 430 nm excitation wavelengths corresponding to the Q_y transition and Soret band of Chlorophyll a/b. Thus indicating both the presence of PSI in the PAni-PSI solid-state films, and its active role in the sensitization and generation of charge separation in the

device. A representative absorption spectrum for spinach PSI is presented in Figure 4.6 (shown in green). For clarity, the spectrum was normalized to the IQE% curve near 430 nm. As expected, the quantum efficiency of the PSI-loaded device correlates directly with the absorption spectrum of PSI's chlorophyll antenna, and thus indicates PSI's role in charge separation in these solid-state devices.

To better corroborate the band alignment predictions of this novel PSI-composite solid-state device, the metallic cathode material was altered. With all other components of the device kept constant, devices were prepared with an evaporated metal of lower or higher work function than silver. It was hypothesized that gold, with a work function of -5.1 eV, would perform poorly as a cathodic material because it is energetically lower than the P700/$P700^{+}$ redox site of PSI, thus making it unable to accept holes from the oxidized protein. An evaporated aluminum cathode should produce significantly less photocurrent than silver because the work function of Al (-4.08 eV) is higher than the conduction band of TiO_2. This energetic mismatch will favor electron-hole pair recombination in the PAni matrix, over the effective charge separation and migration pathway through the entrapped PSI. The comparison of silver, gold, and aluminum as cathode materials in PAni-PSI/TiO_2 devices is presented in Fig. 4.7.

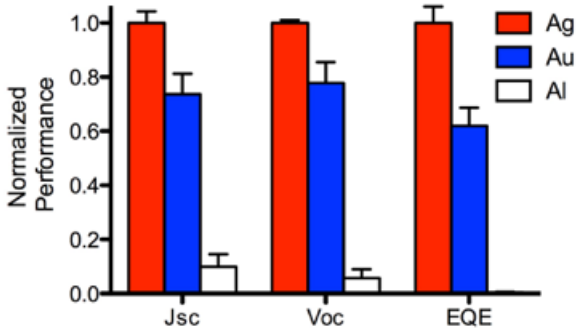

Figure 4.7. Comparison of PAni-PSI/TiO_2 Devices with Ag, Au, and Al Cathodes. Performance of Ag, Au, and Al as evaporated cathodes in PAni-PSI/TiO2 solid-state devices. For clarity, each metric was normalized to the highest performing electrode material. Error bars represent the standard error of a minimum of 4 replicates.

As predicted, the use of silver as the cathode material resulted in the highest photocurrents, open-circuit voltages, and efficiencies based on its favorable energy alignment with PSI and TiO_2.

In addition to the performance of this solid-state biophotovoltaic, there are superior advantages over previous PSI devices in cost and long-term stability. The utility of Ag/PAni-PSI/TiO_2 devices has been demonstrated here by the simple design, wide availability of PSI from spinach and other plants,[66] and low-cost device fabrication. More importantly, the stability of this device for long-term performance under real world conditions has proven great utility. By co-depositing PAni and PSI, the conductive polymer advantageously serves as a stabilizing matrix for the entrapped PSI. Operational stability is demonstrated in Fig. 4.8 where the performance of Ag/PAni-PSI/TiO_2 devices was monitored over the course of three days with 12-hour periods of light and dark.

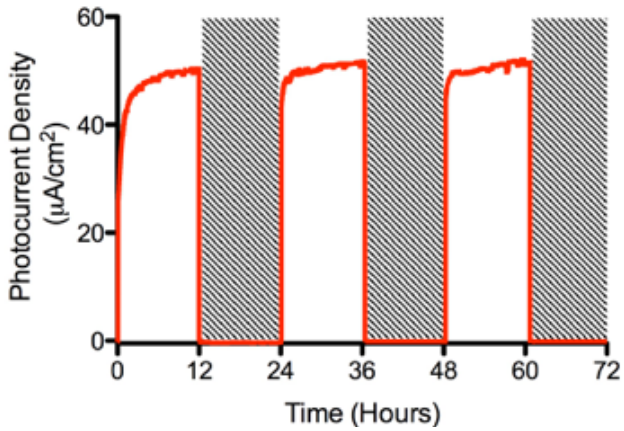

Figure 4.8. Longevity Study of Ag/PAni-PSI/TiO_2 Device. Performance of a typical solid-state PAni-PSI/TiO_2 device was evaluated under 12-hour light and dark cycles for three days. Shaded gray bars represent periods in which the sample was not illuminated.

This light cycling was intended to mimic the solar cycle found in Nature. In this three-day study, the photocurrent output did not decline between the 12-hour illumination periods nor intraday for the duration of the study. This indicates the viability of PSI-based solid-state devices in real world settings. Additionally, the long-term storage stability of Ag/PAni-PSI/TiO_2 devices was evaluated by sampling power curves daily over the course of 20 days and stored under open-air conditions at approximately 20 °C, when not in use. These devices retained greater than 85% of original photocurrent output over the course of the 20 days, which effectively demonstrates the robustness of the PAni-PSI film as an active layer in solid-state solar energy conversion devices, and presents the feasibility of further development of bio-derived solid-state photovoltaics from low-cost materials.

Conclusions

Using facile and low-cost preparation methods, the photosynthetic protein, PSI, has been successfully incorporated into a conductive polyaniline network for direct photocurrent generation. Through electrochemical polymerization, this organic, bio-

derived active layer was grown directly off of transparent TiO_2 electrodes. These photoactive electrodes were then completed with the evaporated metallic cathodes to yield stand-alone solid-state photovoltaics. Solar-simulated I-V analysis revealed that these devices yielded average photocurrent densities of 72 μA cm^{-2}, with an approximate open-circuit voltage of 300 mV, and an external quantum efficiency approaching 0.01%. This performance greatly exceeds the current state-of-the-art in PSI-derived solid-state photovoltaics by nearly 250-fold in photocurrent output, while also being lower in cost and more stable than previous PSI devices. The novel PAni-PSI/TiO_2 devices represent a major advancement in the field of biohybrid solar energy conversion based on their performance, simple cell design, low-cost fabrication materials, facile preparation methods, and operational longevity.

Chapter 5

IN SITU CHEMICAL MODIFICATION OF THYLAKOID-BOUND PHOTOSYSTEM I FOR THE PREPARATION OF ORIENTED PROTEIN FILMS ON ELECTRODE SURFACES

Introduction

In its native environment, Photosystem I operates by sequentially absorbing incident radiation, forming an exciton, dissociating the electron-hole pair, and then migrating those charges in opposite directions. PSI unequivocally shuttles electrons from lumen to stromal with *in vivo* efficiency near unity.[2] The direction of electron flow is dictated by the intrinsic protein structure, which features an organized chain of internal cofactors that move electrons spatially and energetically through a series of small steps. This energy cascade originates with electron hole-pair formation at the P700 "special pair" from which an electron is donated to a primary chlorophyll-based acceptor, denoted as A_0. Subsequently, a phylloquinone analog, denoted as A_1, serves as secondary acceptor, which ultimately donates electrons to the F_x, F_A, and F_B [4Fe-4S] redox clusters on the stromal side.[56] PSI acts in series with other transmembrane proteins to drive photosynthesis and is thus highly dependent on unidirectional orientation. In Nature, PSI spans the thylakoid membrane, with iron-sulfur clusters exposed on the stromal-side of the lipid bilayer where it can be accessed by water-soluble ferrodoxin to mediate electron transfer to later steps of photosynthesis.

However, upon removal of PSI from the thylakoid membrane during protein extraction, control of *in vivo* orientation is lost. It is postulated that oppositely oriented supercomplexes in close proximity to one another will produce zero net photocurrent and

photovoltage.[67] When considering next-generation PSI-based biohybrid photovoltaics, it becomes essential to uniformly orient proteins in films on electrode surfaces to maximize photoperformance. When immobilized within the thylakoid membrane, the iron-sulfur clusters of PSI are bound to the PsaC subunit, located on the stromal side of the lipid bilayer;[26] by standard convention this orientation is denoted as "upright." Thus, when extracted and immobilized on an electrode, a PSI complex with the P700 special pair closest to the electrode surface is in the upright orientation. This is depicted in Figure 5.1. Conversely an "inverted" PSI complex is immobilized with its F_B site closest to the electrode, and P700 site opposite the electrode.

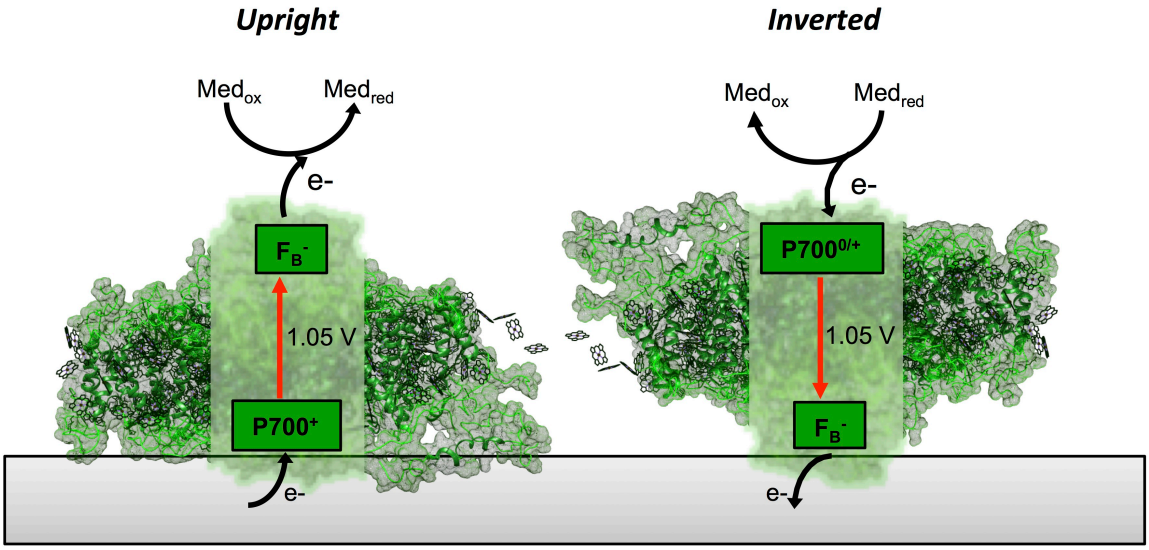

Figure 5.1. Competing Electrochemical Processes Derived from Oppositely Oriented Photosystem I Complexes. For a randomly assembled monolayer on an electrode, the most likely orientations of PSI are presented with their accompanying electron transport vectors: an upright (left) orientation with its P700 special pair in proximity to the electrode interface, and inverted (right) with its reduced iron-sulfur cluster closest to the electrode.

Previous work was successful in mitigating the competing electrochemical reactions introduced by oppositely oriented proteins through the use of semiconductor

electrodes. It was demonstrated by the Carmeli research group that semiconductor electrodes are capable of directing electron flow in a PSI device, and that this flow could be modulated by shifting the Fermi energy by introducing a p- or n-type dopant in GaAs.[68,69] Mitigation of the negative effects from random protein orientation was best demonstrated by LeBlanc et al. in 2012 when p-doped silicon was used as the underlying electrode for a PSI device.[19] In this device type, the valence band of the semiconductor was capable of donating electrons to the oxidized $P700^+$ special pair for PSI complexes found in the "upright" orientation. However, based on the Fermi energy of the p-doped silicon, the underlying material was incapable of accepting electrons from any PSI complexes present in the "inverted" orientation with their F_B clusters adjacent to the protein/Si interface. Thus, only "upright" PSI complexes in the multilayer contributed to the total electrode photocurrent, and oppositely oriented proteins did not. Although this device type produced maximum photocurrent output of 875 μA cm^{-2}, it is hypothesized that photocurrent could be further enhanced by orienting all PSI complexes in the multilayer film, such that every protein was contributing to the overall photocurrent with P700 center oriented towards the underlying silicon electrode.

Previous research efforts that sought to orient PSI on electrode surfaces have utilized gene modification (i.e. cysteine insertion, His-tagging),[20,68,70] electrophoretic deposition,[48,57] or Langmuir-Blodgett film assembly.[71,72] Although, these methods demonstrated some utility and notable performance increases, each of the methods have their own drawbacks. In the case of gene modification, the process is not readily scalable or cost effective thus making it unfit for developing widely deployable solar energy conversion platforms. Further, PSI studies with electrophoretic and Langmuir-Blodgett

depositions remain inconclusive with respect to the true uniformity of protein orientation in films prepared using these techniques.

In the present work, we seek to develop a facile modification strategy that utilizes simple chemical techniques for rapid assembly of PSI into oriented films directly on electrode surfaces. After studying the natural structure and function of thylakoid-bound PSI, three key observations were made: 1) PSI is always assembled in the upright orientation when anchored within natural thylakoid membranes, 2) PSI is an integral membrane protein that spans the entire membrane with an equatorial hydrophobic protein region and two hydrophilic polypeptide subunit regions that extend beyond the lipid bilayer on luminal and stromal sides, and 3) the thylakoid membrane acts as a natural barrier to restrict free transport of water soluble small molecules from stroma to lumen. Combining these three considerations a simple functionalization method was devised in which amino acid modifications were performed on PSI in intact thylakoid membranes. While still membrane-bound, PSI's stromal-side polypeptide subunits, e.g. PsaC, PsaD, and PsaE, are solvent exposed, making many amino acid side chains accessible to chemical modification. Advantageously, the intact lipid bilayer serves as a natural barrier to inhibit diffusion of the modifying ligand, thus selectively modifying only amino acid targets on the stromal side. Lysine was identified as a target for modification based on their abundance on the stromal side of PSI (64 residues),[25] as well as the vast sum of known amine-specific bioconjugation reactions.[73]

There are several key criteria when determining a proper modifying ligand to be used in this functionalization strategy. Most importantly, the ligand modifying must introduce some terminal chemical moiety for favorable binding with a desired surface.

Basic examples of this include: alkane thiols for gold electrodes, alkylsilanes for glass, and alkylphosphonates for metal oxides. Additionally, ligands featuring an ω-alkyne offer even greater versatility and specificity via bioorthogonal click coupling reactions in which a desired substrate is surface-modified with a complementary azide. For this study, a thiol-terminated ligand was used, which allows for the exploitation of gold-thiol affinity for proof-of-concept experiments. Opposite of the thiol terminus, the desired ligand also requires specific reactivity for its desired amino acid target, i.e. primary amines. As a photoactive protein, turnover of PSI is highly dependent on electron transport kinetics at both the donor and acceptor sides. Electron tunneling rates decay exponentially with increased distance through a molecular wire.[74] Thus, in order to maintain rapid electron transport from PSI's F_B^- site to the underlying electrode, a short chain alkane (2-6 carbon units) spanning this interface is desirable.

Considering all the aforementioned criteria, a modifying ligand with amine-specific reactivity at one terminus and thiol moiety at the opposite end, with a short chain connecting the two termini must be used. For practical reasons, the ligand must be inexpensive and water soluble to prevent transport across the intact thylakoid membrane. 2-iminothiolane, also known as Traut's Reagent, is a commonly used reagent for thiolating proteins. It is selective for amines with high specificity, and introduces a thiol terminus via a short four-carbon chain added to lysine side chain.[75] Traut's reagent was used for proof of concept experiments in which PSI was stromal-side thiolated for directed self-assembly of oriented films on gold electrodes. An outline of the stromal-side modification procedure is presented in Figure 5.2 where PSI is shown with its surface accessible lysine residues highlight in red.

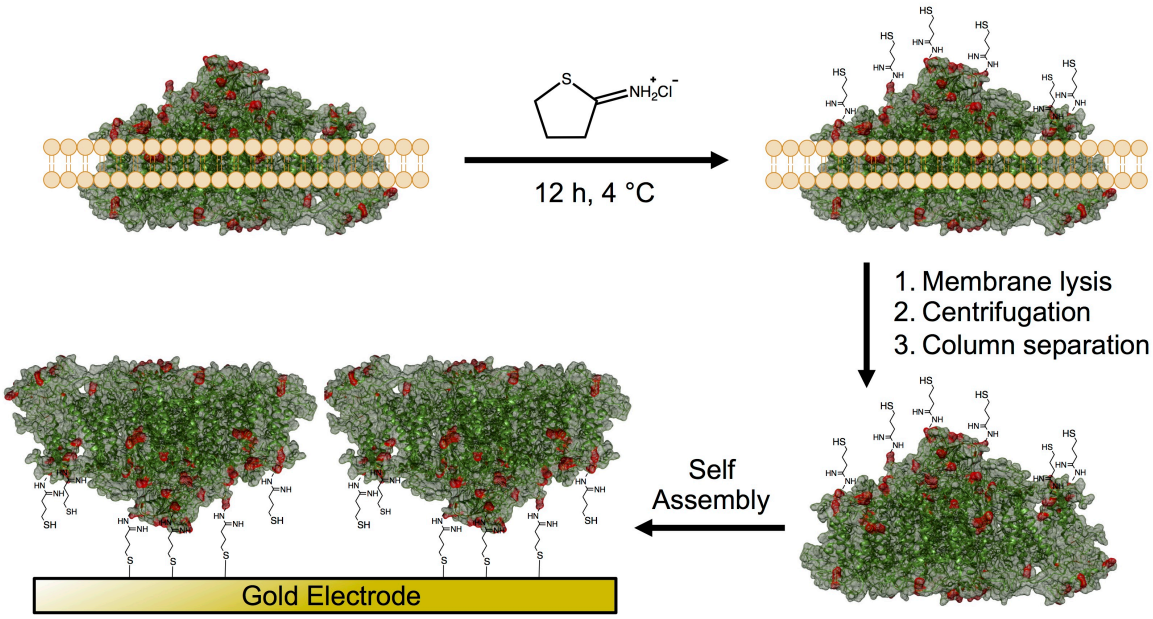

Figure 5.2. Strategy for Side-Selective Thiolation of PSI. Stromal-side modification occurs through the use of an amine specific thiolating ligand, 2-iminothiolane (Traut's Reagent). The extraction procedure carried out such that intact thylakoids are collected, then Traut's reagent is added to the suspension of thylakoids. Following amine modification, the lipid membranes are disrupted and the modified proteins are isolated. The side-segregated thiolating ligands will then produce a uniformly inverted monolayer on a gold electrode via self-assembly.

As depicted in Figure 5.2, PSI has two distinct water-soluble polypeptide regions present on the luminal and stromal sides of the thylakoid membrane, both of which are rich in lysine residues. Thus, traditional chemical modification strategies of isolated PSI lack selectivity in where modification occurs on the protein, and subsequently cannot be relied on to construct oriented protein films. However, when membrane-bound within the intact thylakoid, PSI's hydrophilic regions are separated by the lipid bilayer. This provides a unique, natural barrier to restrict chemical modification to only one hemisphere of the protein. This facile functionalization strategy began with the extraction and purification of intact thylakoids from spinach leaves. Then excess Traut's reagent was added to a solution of thylakoids and left to react overnight under refrigeration. Following reaction completion, unreacted Traut's reagent was removed, and modified

PSI complexes were extracted from the thylakoid membranes via surfactant-based lysis. Further purification was performed through centrifugation and column chromatography.

Validation of this facile modification protocol was carried out via Ellman's assay in which sulfhydryl functional groups on the PSI-Traut's conjugates were spectroscopically quantified. Additionally, improved electrochemical performance was observed in the form of enhanced photocurrent for PSI-Traut's modified gold electrodes as compared to native PSI modified gold electrodes. This protocol represents a novel method for rapid side-selective functionalization of membrane proteins for the purpose of preparing oriented, functional protein/electrode interfaces, with applications in energy conversion/storage and biosensors.

Experimental

In Situ Functionalization of Membrane-bound PSI

Approximately 100 g of deveined baby spinach leaves were macerated in a household blender along with 200 mL of Grinding Medium (330 mM sorbitol, 10 mM sodium pyrophosphate, 4 mM calcium chloride, and 2 mM ascorbic acid). This mixture was then sequentially filtered through two, and then eight, layers of cheesecloth. This filtrate was then divided into 8 tubes and centrifuged at 8000 x g for 1 min to precipitate the non-chloroplast material. The pellets were washed with additional grinding medium and centrifuged again at 8000 x g for 1 min. Finally, the pellets were resuspended in 50 mM phosphate buffer (pH = 7.0) and combined into a single suspension of thylakoid membranes (ca. 30 mL), to which 500 mg of Traut's reagent (Thermo Scientific) was added.

The thylakoid reaction mixture was mixed gently and then left in the refrigerator at 4 °C overnight. Following the reaction period, the thylakoids were centrifuged into a pellet at 8000 x g for 1 min and the supernatant containing unreacted Traut's reagent was discarded. The pellet was washed with approximately 20 mL of 50 mM phosphate buffer, and then the centrifugation process at 8000 x g for 1 min was repeated again.

The pellet containing Traut's-modified thylakoid membranes was then washed with a surfactant-rich Resuspending Medium (50 mM HEPES pH = 7.6, 330 mM sorbitol, 2 mM EDTA, 1 mM magnesium chloride hexahydrate, 1 mM manganese (II) chloride tetrahydrate, and 1% Triton X-100) in order to lyse the thylakoid lipid bilayers. The solution was excessively vortexed and then centrifuged at 20,000 x g for 15 min at 4 °C. The resulting supernatant was then loaded onto a chilled hydroxlapitite column equilibrated with 20 mM phosphate buffer (pH = 7.0). The column was continually washed with Column Buffer (20 mM sodium phosphate, pH = 7.0) to elute all non-protein components, as the PSI was adsorbed on the hydroxylapitite resin. After thorough washing, Elution Buffer (200 mM sodium phosphate, pH = 7.0) was used to elute the PSI off the column. Protein samples were collected and stored at -80 °C for later use.

Thiol Quantification by Ellman's Assay

The degree of thiolation was determined by spectrophotometric assay in which 5,5'-dithio-bis-(2-nitrobenzoic acid) was added to PSI-Traut's conjugates to react 1:1 with reduced sulfhydryl groups and induce as colorimetric change at 412 nm.[76] First, 2450 μL of phosphate buffer (20 mM, pH = 7.0) and 500 μL of modified PSI-Traut's were combined in a cuvette. A baseline absorbance spectrum was collected from 400-700 nm, using a blank comprised of 2450 μL of phosphate buffer, and 500 μL of Elution

Buffer. After collecting a baseline scan, 50 μL of a stock (5 mg mL^{-1}) of 5,5'-dithio-bis-(2-nitrobenzoic acid) (Ellman's Reagent) was added to each sample and reference cuvette and mixed thoroughly. 15 minutes elapsed to ensure reaction completion. An absorbance scan was collected again from 400 – 700 nm.

After correcting for dilution in total sample absorbance contributed by the 50 μL spike of Ellman's stock, the baseline absorbance spectrum was subtracted from the 15-minute post-spike spectrum. The change in absorbance at 412 nm for each PSI sample, and the molar absorptivity from a calibration curve prepared from a range of cysteine standards, were used to determine the concentration of thiols in each sample.

The thiol quantity in each protein sample was normalized by the total P700 concentration, as determined using Baba assay.[23] For comparison, unmodified PSI samples were also analyzed using this assay.

Self-Assembly and Electrochemical Analysis of PSI-Traut's Conjugate Films

Gold on silicon wafers were used as the substrates for self-assembly and electrochemical analysis of the PSI-Traut's conjugates. Wafers were extensively Piranha cleaned (concentrated 3:1 H_2SO_4:H_2O_2) to ensure a pristine gold surface prior to use. Clean substrates were then covered in a solution of PSI-Traut's or unmodified PSI for a minimum of 18 h. Note: all PSI stock solutions were dialyzed against 3L of DI water prior to use to remove excess buffer salts and Triton X-100. Following each self-assembly period, modified Au/Si wafers were removed from their respective solutions, rinsed with copious quantities of DI water, and gently dried with a stream of nitrogen.

Electrochemical measurements were performed in a homemade electrochemical cell in which the wafer was clamped onto the sidewall of the open aperture cell, and

sealed with an O-ring producing an electrode area of approximately 0.2 cm^2. The reservoir of the cell was filled with an electrolyte solution of 100 mM KCl, 5 mM sodium ascorbate, and 1 mM 2,6-dichlorophenolindophenol (DCPIP). A platinum mesh wire was used as the counter electrode, along with an Ag/AgCl reference electrode.

Photochronoamperometric experiments were carried out at each sample's respective dark open circuit potential. This electrode bias allows for direct measurement of the current contribution from light-dependent electrode reactions. Current over time was collected over 60 seconds in which the sample was equilibrated in the dark for 0-20 s, then illuminated for 20-40 s, then again in the dark for 40-60 s to return to baseline. Current averages for each run were collected by averaging the data points in the steady-state current region from 25-35 seconds, at a sampling interval of 0.1 s. As a negative control, bare gold electrodes were also analyzed to determine any photoactive contribution from the sodium ascorbate/DCPIP mediator system. Each sample type (bare gold, unmodified PSI, and PSI-Traut's) was repeated a minimum of three times.

Results and Discussion

Following the modification of PSI with Traut's reagent while still membrane bound, it is important to characterize the newly formed conjugates by determining the extent of thiolation. This was accomplished through the use of Ellman's Assay. This technique utilizes a reactive chromophore that changes from colorless to yellow (λ_{max}=412 nm) in the presence of reduced sulfhydryl groups. Addition of excess Ellman's reagent to a sample of PSI-Traut's produced an increase in absorbance near 412 nm. A calibration curve prepared from standards of cysteine allows for the direct analytical quantification of thiols under these assay conditions. Figure 5.3, presents the quantity of

thiols detected in each sample type, after normalization by the P700 concentration of each sample.

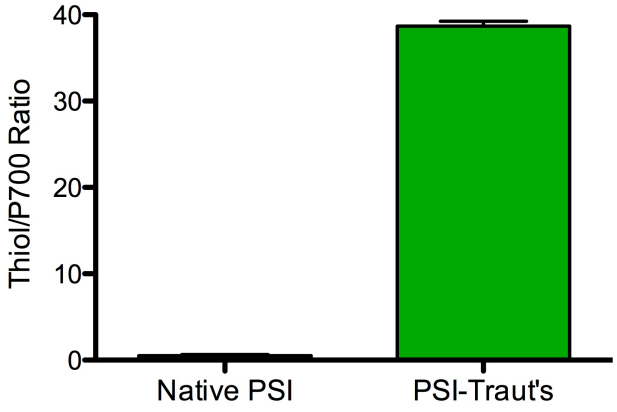

Figure 5.3. Thiol/P700 Ratio for Modified PSI as Determined by Ellman's Assay. Thiolation of modified PSI-Traut's conjugates (green) was quantified. For comparative purposes, native unmodified PSI was also evaluated (red). Each column represents the average and standard error of three replicates for each sample type.

The modified PSI-Traut's conjugates produced a much more intense colorimetric change, which corresponded to the presence of new thiol groups. The native, unmodified PSI produced a very small change in absorbance at 412 nm, which was calculated to correspond to a thiol/P700 ratio of 0.5 ± 0.3. This observation is in agreement with the known structure of PSI, which contains very few surface accessible reduced sulfhydryl moieties. Nearly all of the native cysteines present in the complex are either restricted to the interior of the protein, or dimerized in disulfide bridges. Ellman's assay is specific for reduced thiols and not disulfides.

Comparatively, the modified PSI-Traut's conjugates yielded a thiol/P700 ratio of 36.6 ± 1.0, which is considerably more than the unmodified PSI. Thus, this simple assay indicates that the *in situ* modification protocol performed prior to membrane lysis has successfully thiolated PSI. Additionally, the 36 new thiols introduced via this protocol is in good agreement with the theoretical number of modification sites, i.e. 66 lysine

residues on the stromal side. This number of thiols is expected to be acceptable degree of functionalization as it optimizes the interplay between maximizing the number of sites for surface binding, without over modifying the protein and disrupting its natural structure and function.

Further characterization was performed on the PSI-Traut's conjugates by photochronoamperometry. Using this method, the photoactivity of the protein can be accessed when self-assembled into monolayers on gold electrodes. This strategy allows for the determination of the self-assembly properties, and also the photoactivity following chemical modification of the protein. Electrochemical analysis was carried out in a mediator solution of sodium ascorbate and DCPIP, which can donate electrons to the oxidized P700 center of PSI to turnover the photocatalytic cycle.

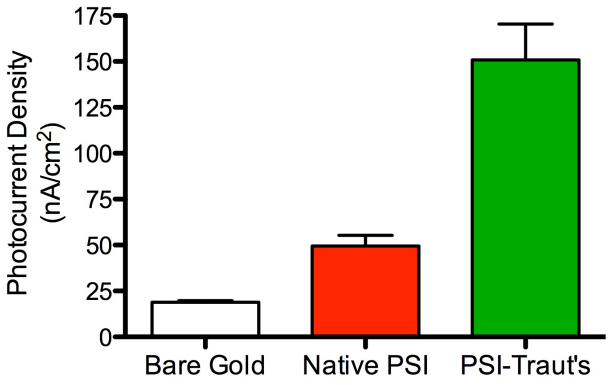

Figure. 5.4. Photoactivity of Self-Assembled Films of Native and Traut's Modified PSI. Photochronoamperometric analysis was used to evaluate the photocurrent output of gold electrodes modified with self-assembled monolayers of native PSI (red) and preextraction-functionalized PSI-Traut's conjugates (green). Bare gold was also tested a negative control. Samples were tested in an electrolyte solution of 100 mM KCl, 5 mM sodium ascorbate, and 1 mM DCPIP. Each bar represents the average and standard deviation of a minimum of three replicates.

From the photoelectrochemical analysis presented in Figure 5.4, it becomes apparent that the modified PSI (150 ± 40 nA cm^{-2}, n = 5) performed significantly better than the traditional unmodified PSI (49 ± 10 nA cm^{-2}, n = 3). Additionally, the bare gold

only produced a modest photocurrent density of 19 ± 2 nA cm^{-2} (n = 6), which corresponds to the photocurrent contribution from only the photoactivity of the mediator solution without any PSI present.

The 3-fold enhancement in photocurrent density of films of PSI-Traut's over the films of native PSI indicates superior electron transport from enzyme to electrode. Most likely, this can be attributed to the direct electronic connection introduced through the many gold-thiol bonds anchoring the protein to the underlying electron. The native PSI, which does not feature many surface cysteine residues, binds non-specifically to the pristine gold surface with little or no orientation specificity. This enhancement is also indicative of preferential film orientation presented by the modified PSI-Traut's conjugates during self-assembly. This enhancement was predicted for a self-assembled monolayer in which a film assembly preferentially favors one orientation (inverted or upright), and the competing electrochemical reactions from the opposite orientation are minimized.[67]

The increased photocurrents represent a vast improvement in current monolayer PSI films, and are indicative of oriented assembly accompanied with direct electronic connection of protein and electrode. However, additional validation is required to fully characterize and quantify the degree of protein orientation.

Conclusions and Future Directions

A new protocol has been developed for the *in situ* modification of Photosystem I prior to membrane lysis. By thiolating the protein while still membrane bound, the modification sites are restricted to only the solvent accessible sites on the stromal-side of the thylakoid membrane. Thiolation was chosen as the proof-of-concept functionalization

strategy because it offers the ability to directly bind the protein to gold electrodes with high affinity and specificity. This was carried out using the low-cost, water soluble Traut's Reagent, which is amine reactive and grafts a reduced sulfhydryl moiety on the end of the short four-carbon alkane chain.

In order to characterize the modified PSI conjugates, the quantity of new thiol groups was determined using the thiol-specific Ellman's Assay. This analysis validated that the thiolation was successful, and introduced 36.6 ± 1.0 thiols to each protein. Additionally, electrochemical analysis of self-assembled films, in the form of photochronoamperometry, revealed 1) PSI-Traut's conjugates successfully self-assembled into films on pristine gold electrodes, 2) those films of PSI-Traut's retained photoactivity following extensive chemical modification, 3) photocurrents generated by the modified PSI-Traut's films were significantly higher than unmodified PSI films, possibly indicating some preferential orientation of PSI.

Two key questions still remain about this protein functionalization strategy. First, we must analyze the subunits, and subsequent amino acid sequence, to identify the sites of modification. Understanding which positions on the protein were modified would validate the hypothesis that all thiolation is restricted to a single side of the protein. Using known structural information (PDB entry: 2O01) the presence of thiolating ligands on stromal-side associated polypeptide subunits (i.e. PsaC, PsaD, or PsaE) and the absence on other subunits would validate successful segregation of thiolation sites. This will be accomplished by separating the 12 subunits of the supercomplex, followed by analysis with mass spectrometry. Subunits modified with Traut's reagent will feature a mass addition of approximately 100 Da per ligand. Additional information could be elucidated

by sequencing the polypeptide sequences to examine which lysine residues are most commonly modified. Digestion of the modified protein followed by LC-MS/MS analysis would aide in this analysis.

In conjunction with identifying the thiolated positions with spatial resolution on the protein, it is essential to demonstrate that the Traut's modification actually provides a favorable vector for surface coupling to the electrode, and that this binding gives rise to films with a high degree of orientation. This analysis may be performed using a variety of techniques. Ideally, a scanning probe microscopy (SPM) method with the ability to resolve individual proteins (on the scale of 10 nm) would allow for imaging of protein films as well as the elucidation of orientations of single proteins within an entire film. Scanning Tunneling Microscopy (STM) and Atomic Force Microscopy (AFM) represent two of the most common scanning probe methods, and are capable of collecting topographical images as previously demonstrated for films and crystals of PSI.[36,43,44,48,57,77–79] However, there are many practical restrictions that make this characterization very challenging. In principle, these two methods are ideal for non-contact topographical imaging, which is well suited for analyzing macromolecular assemblies with high resolution. In determining a protein's orientation (i.e. upright versus inverted PSI) from a topographical map, sub-nanometer 2D resolution would be required in order to discern asymmetries based solely on protein structure. Thus, an enhanced SPM method that can topographically map a protein film, and also discriminate between different regions of the same protein, based on chemical activity/reactivity, is desired for this application. Scanning electrochemical microscopy (SECM) is an SPM technique that can map electrochemical activity of 2D surfaces with a nanometer-scale tip electrode that

raster scans over a substrate electrode. SECM exists as a possible technique to record electrochemical signals with x-y spatial resolution. In the analysis of PSI films, ultra-small nanoelectrodes must be fabricated with working electrode diameters of 10 nm or less. In-house fabrication of nanoelectrodes is described in Appendix A. A proposed experiment to assess the orientation of individual PSI complexes in a monolayer film is depicted in Figure 5.5.

First, monolayers of the modified protein will be self-assembled onto planar gold electrodes. Following protein binding, backfilling with a long-chain alkane thiol must be performed to complete the film assembly process and ensure that all electron movement through the film occurs through the photoexcitable electron transfer pathways within PSI. This modified planar gold electrode will serve as the substrate electrode in this two-electrode SECM experiment. A mediator solution of ferricyanide, $Fe(CN)_6^{3-}$ will be used in this analysis because the species in the present, oxidized state cannot readily donate electrons to PSI's photoexcited $P700^+$ redox cluster.

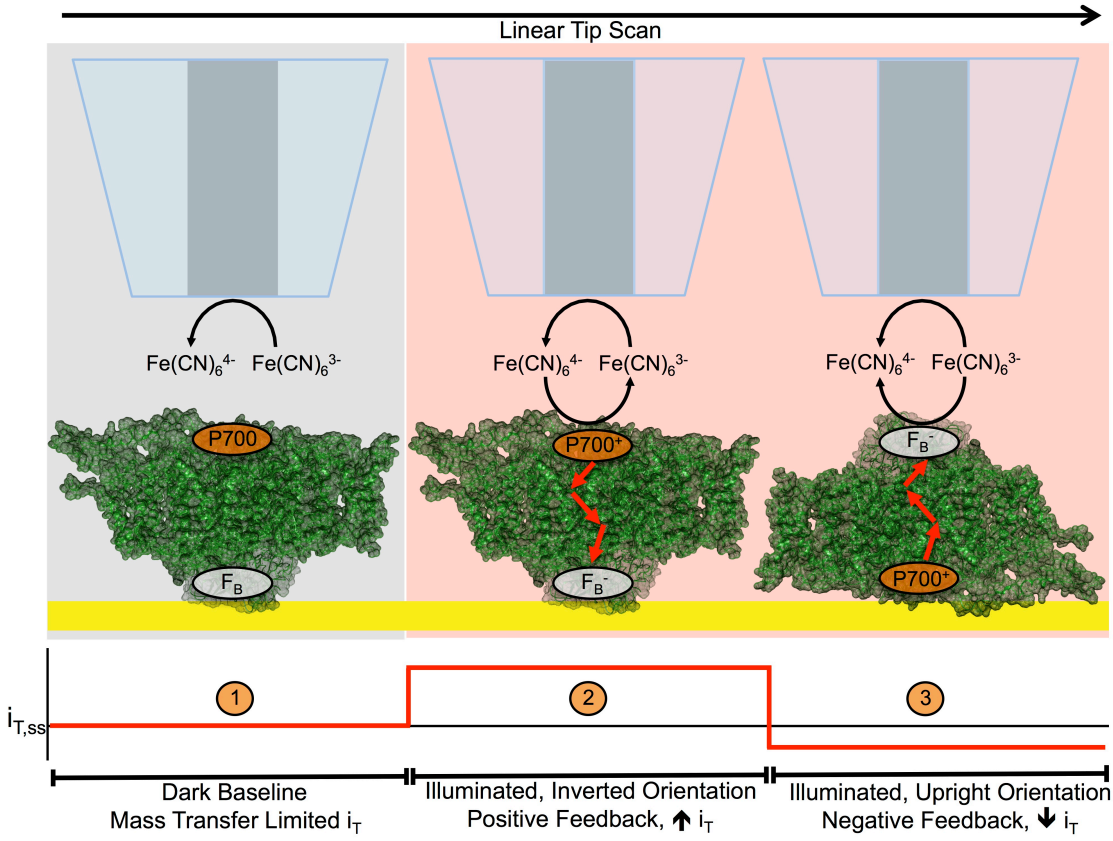

Figure 5.5. Proposed Analysis of PSI Orientation by Scanning Electrochemical Microscopy. Individual PSI complexes will be characterized when self-assembled into films to assess the orientation in either the upright or inverted positions. PSI under dark and light conditions (and in inverted and upright orientations) are pictured with their predicted relative changes in observed tip current (i_T). Using ferricyanide as the mediator, and a nanoelectrode biased at a reducing potential, a mass transfer limited, steady-state tip current will be observed when positioned over the non-illuminated PSI film (1), which acts as an insulating surface. Upon illumination, a positive feedback loop will be generated between tip and inverted PSI complexes (2), and a negative feedback loop will occur between tip and upright PSI complexes (3). These feedback changes will result in positive and negative perturbations in the steady-state tip current, respectively.

When the nanoelectrode tip is positioned over the protein film, the distance separating the electrode and substrate will be approximately equal to 3-5x the diameter of the tip electrode. At this very close distance, the tip electrode, biased at a potential reducing to the ferricyanide, will collect current from the mass-transfer limited reduction of ferricyanide to ferrocyanide. In the dark, the non-photoactivated protein layer will act

as an insulating substrate, and the tip current will be dictated by the diffusion of bulk ferricyanide reaching the tip electrode surface. This is depicted in Figure 5.5, and the accompanying current response is presented in Region 1 of the current-distance scan.

When the substrate is illuminated, and PSI's electron-transport pathways are activated, the locally generated ferrocyanide will be oxidized back to ferricyanide by PSI complexes oriented in the inverted position, such that their $P700^+$ clusters are found at the protein/solution interface. The generation of this positive feedback loop will result in an increase in I_T, as depicted in in Region 2 of the current distance scan of Figure 5.5.

Finally, when the raster-scanning tip encounters an illuminated, upright PSI complex, where the F_B cluster is present at the protein/solution interface, the tip current is expected to dramatically decrease below the dark baseline. This is predicted because ferricyanide will act as an electron acceptor from the donor side of PSI, thus creating a reaction that directly competes with the reduction of ferricyanide to ferrocyanide at the SECM tip. This direct competition will reduce the local concentration of ferricyanide available at the tip below the previous mass transfer limit seen in the dark baseline. The negative feedback loop between tip and upright Photosystem I complex is shown in Figure 5.5, and the predicted current output is shown in Region 3.

With this SECM experimental setup, and a sufficiently small nanoelectrode, an entire self-assembled PSI film can be topographically mapped, and based on the resulting spatially resolved photocurrents the orientation of individual proteins in the film can be determined. This advanced analytical technique, along with information about the degree and structural position of thiolation sites on the modified protein, would provide

conclusive insight into the effectiveness of our novel *in situ* functionalization strategy for orienting large biomolecules on surfaces.

In addition to the thiolation performed in this proof-of-concept study, many other modification types could be performed to attach proteins to functional surfaces. Future work on this subject must accommodate a broader range of bioconjugation methods in order to apply this technology to a larger set of applications. Examples of this include the modification of alkylphosphonate ligands to a protein for self-assembly on conductive metal oxide films with possible optoelectronics applications in biosensing.

Chapter 6

SILICON-BASED PHOTOSYSTEM I SOLID-STATE PHOTOVOLTAIC DEVICES[c]

Introduction

In the development of more efficient PSI derived biophotovoltaic devices, many alternative electrode materials and device architectures have been explored. Traditional proof-of-concept studies have traditionally been carried out on gold electrodes due to its conductivity and inert nature. However, many semiconducting materials provide superior advantages for interfacing with PSI based on their chemical availability, tunable energetic properties, and/or transparency. As previously demonstrated in Chapter 4, TiO_2 makes an excellent electrode substrate for PSI.[80] This superior performance is largely derived from the electronic properties of the TiO_2 anode, which acts an ideal n-type material to accept electrons from the PSI photoactive layer.

Prior to the use of TiO_2 as a cathodic electrode, LeBlanc et al. demonstrated the utility of interfacing PSI with semiconductor electrodes.[19] Specifically, PSI was deposited onto p-doped silicon substrates, which outperformed PSI deposited on metallic electrodes as well as n-type silicon. The success of this material is attributed to the energetic match between the Fermi level of the p-doped silicon and PSI's oxidized $P700^+$ redox cluster. This energy match is showcased in Figure 6.1, where the approximate energies of the

[c] Beam, J. C.; LeBlanc, G.; Gizzie, E. A.; Ivanov, B. L.; Needell, D. R.; Shearer, M. J.; Jennings, G. K.; Cliffel, D. E.; Lukehart, C. M. Construction of a Semiconductor-Biological Interface for Solar Energy Conversion: P-Doped Silicon/Photosystem I/ZnO. *Langmuir* **2015**, *31*, 10002–10007.

conduction and valence bands p-Si are shown relative to the known redox potentials of PSI's cofactors.

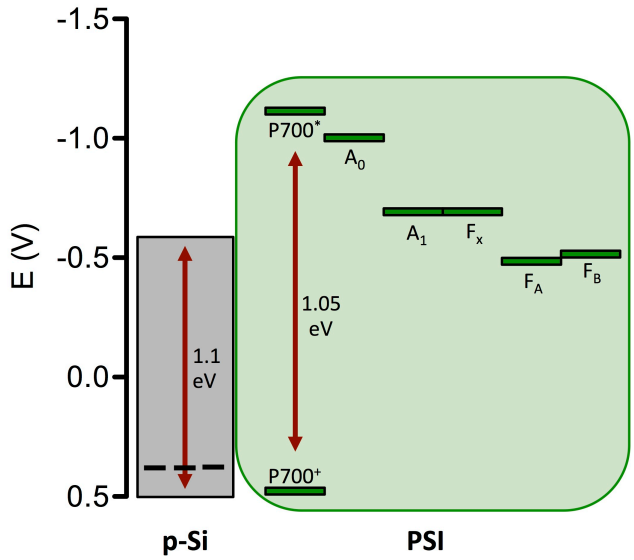

Figure 6.1. Band Energy Alignment Between p-Doped Si and Photosystem I. P-doped silicon (left) is presented beside PSI (right) where the relative positions of PSI's redox cofactors can be compared to the band energies of the semiconductor. The Fermi energy (dashed line) of the p-doped Si is in a favorable position to donate electrons to the oxidized $P700^+$ reaction center. Further, the conduction band of silicon is higher in energy (approximately -0.6 V) than the terminal and penultimate reduced iron-sulfur clusters of PSI (-0.55 V).

From the energy diagram in Figure 6.1, the favorable energy alignment between PSI and p-Si becomes apparent. The Fermi energy of p-doped silicon is predicted to be more negative than the valence band of silicon, which resides at approximately +0.5 V vs. NHE. At this position, the p-type semiconductor can favorably donate electrons to the P700 reaction center following exciton formation and charge separation. Comparatively, the conduction band is more negative than the F_B electron donor site of PSI, thus making the material a poor electron acceptor from the protein. Using p-Si as the underlying electrode, PSI multilayer films produced very large photocurrents (875 μA cm^{-2}) using an electrolyte solution of 200 mM methyl viologen.

Although, this currently represents the highest reported photocurrent density for a PSI electrode, the use of liquid electrolytes, especially with high mediator concentrations, does not represent a long-term solution for low-cost, scalable, bioderived photovoltaic devices. In order to create solid-state photovoltaics, the p-doped silicon/PSI photoelectrode must be outfitted with a dry electron accepting material and/or anode to complete the photovoltaic device. Ideally, a second semiconducting layer would be selected such that the conduction band of that semiconductor was favorably aligned with the terminal iron-sulfur cluster, F_B, of PSI. This type of device was first conceptualized and developed by LeBlanc and Beam in 2015, where a p-Si/PSI/ZnO device was constructed.[81] This study represents the first known device where PSI is interfaced with two different semi-conductors to create a solid-state photovoltaic device.

The non-trivial task of depositing ZnO directly onto a biological material was achieved using the novel Confined Plume Chemical Deposition (CPCD). In this process a suspension of a ZnO precursor is dropcast onto the PSI multilayer film, which is then confined under a glass plate, and then irradiated with a pulsed IR laser. A majority of the IR radiation is absorbed by the precursor layer, which then rapidly decomposes. The rapid cooling of the confined reaction plume leads to surface-nucleated growth of zinc oxide crystals directly on the PSI surface. A schematic for the device fabrication is presented below in Figure 6.2.

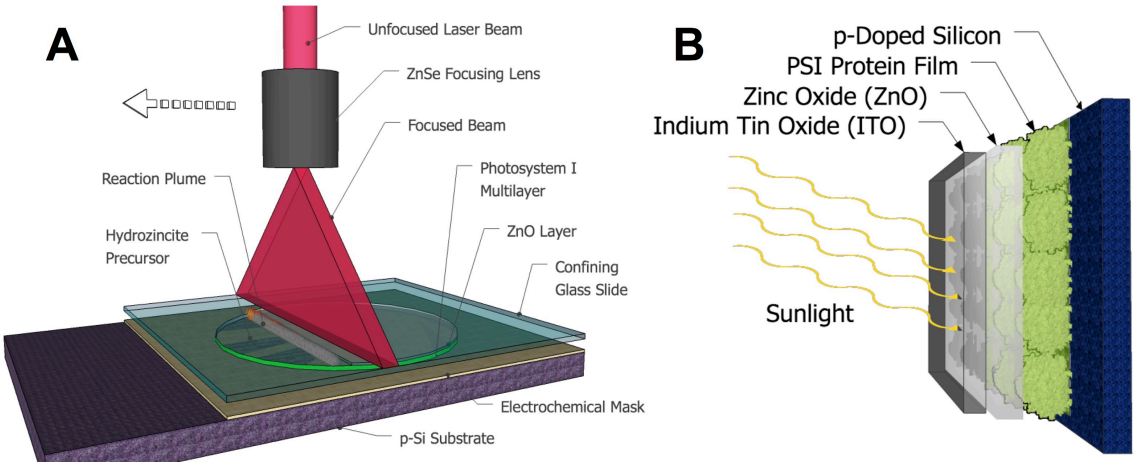

Figure 6.2. CPCD Deposition of ZnO on PSI/p-Si and Representative Cross Section of ZnO/PSI/p-Si Device. A) ZnO is deposited on PSI multilayer on p-doped silicon by CPCD. A ZnO precursor is drop cast onto the PSI film, then confined under a glass slide prior to rastered IR laser pulses. B) A layer-by-layer cross section is depicted for a ZnO/PSI/p-Si device. The p-Si wafer acts as the cathodic substrate upon which a PSI multilayer is deposited. A thin film of ZnO is deposited onto the PSI layer, and then an ITO layer acts as the conductive anode. Illumination of this device occurs though the transparent ITO/ZnO layer.

The method for depositing ZnO directly onto PSI to develop a dual PSI/semiconductor interface represents one of the most effective solid-state PSI photovoltaic devices. Figure 6.2A depicts the fabrication process in which a pulsed IR laser decomposes a precursor, confined under a glass slide, into a thin, transparent metal oxide film. A stack up of the device is presented in Figure 6.2B. The device is backed by a p-doped silicon wafer, which acts as the device cathode. Upon this wafer, a multilayer of PSI is deposited utilizing previously described vacuum deposition methods. CPCD (Figure 6.2A) is then performed to deposit the thin film of ZnO, which act as the electron-accepting layer of the device. A layer of ITO/PET is then added as a conductive backing for the ZnO layer, which also adds structural support for electrical contact. This device yields the highest reported photocurrent density (127 μA cm^{-2}) among all solid-

state PSI-based photovoltaics. These devices also performed with great stability when tested over a period of 14 days.

The technology presented here is a major advancement in solid-state biophotovoltaics. Its hallmark ZnO layer was rapidly prepared from low-cost precursor materials. However, the use of a pulsed IR laser system to fabricate the film is not a facile method to prepare PSI-based devices. Thus, we now seek to develop a similar performing device featuring an electron transport layer that can be rapidly assembled and scaled.

Polyviologens are a unique class of organic polymers with tunable redox properties first reported in 1971.[82] Monomeric viologens have been widely used as diffusion mediators in wet-cell PSI device based on their ideal redox potentials for accepting electrons from F_B^-. Most commonly, methyl viologen is used with PSI films due to its 2+/1+ redox couple at -0.453 V vs. NHE. However, the redox potential of the viologen can be tuned by altering the N-alkyl groups on the 4,4'-bipyridine. Polyviologens possess very similar properties to their monomeric counterparts with the added advantage that they can be used to prepare dry films that can shuttle electrons in the solid state. Structures for methyl viologen and poly(methylviologen) are presented in Figure 6.3.

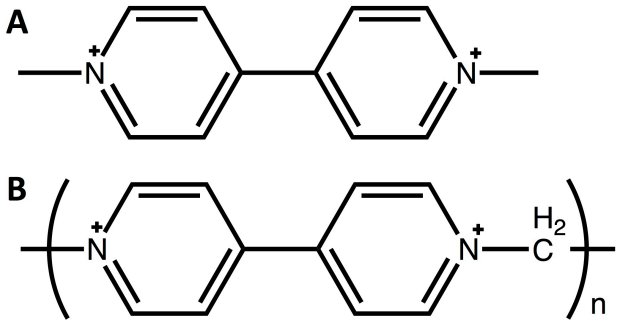

Figure. 6.3. Structures of Methyl Viologen and Poly(methylviologen). Methyl viologen (A) is used commonly as a diffusional redox mediator for PSI systems. Poly(methylviologen) (B) can be synthesized to have similar redox properties to the monomeric form, but the higher molecular weights allow for the formation of robust dry films.

Structurally, the small molecule methyl viologen and the repeating units of the polymer are homologous based on their central 4,4'-bipyridine moiety. Quaternization of the nitrogen atoms on the bipyridine yields two positive charges localized on the ring system, giving rise to the intrinsic metal-free redox activity of the polymer. Altering the substituent groups attached to the nitrogen atoms will cause a shift in the redox potential of the compound, corresponding to the electron donating or withdrawing nature of the substituent group. For instance, an alkyl group added to the bipyridine will act as an electron-donating group, which shifts electron density toward the heterocycle, thus creating a greater energetic boundary for the acceptance of another electron. The result is a negative shift in the reduction potential. The alternative is true for an electron-withdrawing group bound to the quaternary nitrogen. In such a case, a positive shift in the redox potential is predicted. In addition to the tunability, polyviologens are also water-soluble, are easily synthesized from low-cost starting materials, and the products can easily be purified and processed into thin films. These key attributes make them interesting materials for interfacing with PSI.

Polyviologens first attracted attention as photoinitiated electron-transfer materials when quenching was observed for photoluminescent ruthenium complexes in the presence of polyviologens.[83] The quenching phenomenon indicates that polyviologens rapidly accept excited state electrons from a primary donor. This property was further exploited by the Weiss Group, which prepared composite films of CdSe quantum dots and poly(p-xylylviologen).[84,85] These critical studies provided several key insights on the behaviors or polyviologens: 1) electron transfer from particle to polymer occurs in solid-state thin films, 2) photoelectron transfer from quantum dot to polyviologen occurs on an ultrafast time scale (<10 ps), 3) reduced polyviologens are capable of subsequent electron donation to a secondary acceptor. These findings, along with the favorable thermodynamic redox potentials, indicate that polyviologens are a class of materials that are suitable electron transport layers in PSI solid-state photovoltaics.

In the studies presented in this chapter, poly(p-xylylviologen) (PxV) (Figure 6.4) was selected as the preliminary polyviologen to use in proof-of-concept experiments. The polyviologen was synthesized, characterized, and deposited into films on p-Si/PSI to act as a simple electron-transport layer in p-Si/PSI/PxV/ITO solid-state devices.

Experimental

Synthesis and Characterization of Poly(p-xylylviologen)

Poly(p-xylylviologen) was synthesized using the scheme described by Factor and Heinsohn,[82] as outlined in Figure 6.4.

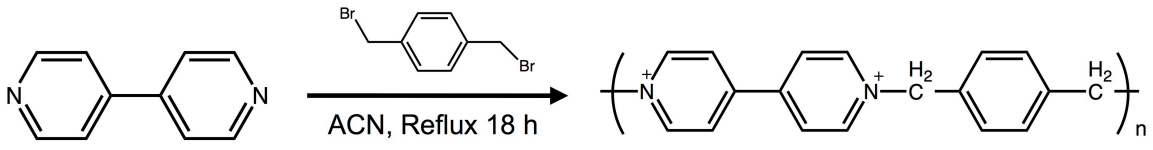

Figure 6.4. Reaction Scheme for the Synthesis of Poly(p-xylylviologen).

Equimolar quantities of 4,4'-bipyridine and α,α'-dibromo-p-xylene were dissolved in dry acetonitrile in a round bottom flask with a reflux condenser attached. Shortly after onset of the reflux, a yellow precipitate formed. The reaction mixture was held at reflux for approximately 18 h to ensure completion. The crude product was separated on a sintered glass vacuum filter, and washed with copious amounts of dry acetonitrile. The purified yellow solid was dried under vacuum for 30 minutes.

The redox properties of the synthesized PxV were determined by cyclic voltammetry performed using a CH Instruments 660A workstation. A 1 mg/mL solution of the product was prepared, and supplemented with 100 mM KCl. This sample was then argon purged for 20 minutes to remove any residual oxygen in the solution, which would mask the characteristic viologen reduction peak. A 2mm glassy carbon disk was used as the working electrode, along with a platinum mesh counter electrode and an Ag/AgCl reference electrode. Cyclic voltammograms were collected by scanning from 0 to -0.6 V at a scan rate of 0.01 V/s.

^{1}H-NMR was performed on the PxV product, approximately 50 mg/mL in D_2O, using a Bruker 400 MHz NMR.

Poly(p-xylylviologen) Deposition and Solid State Device Fabrication

Solid-state p-Si/PSI/PxV/ITO devices were assembled as outlined in Figure 6.5. The process began with hydrofluoric acid etching of lightly p-doped <100> silicon wafers (University Wafer, Boston, MA). HF etching was performed by submersion of the substrate in a freshly prepared aqueous 2% HF solution for 1 minute. After removing the surface oxide, the substrate was masked with electrochemical mask to yield an exposed area of 1 cm^2.

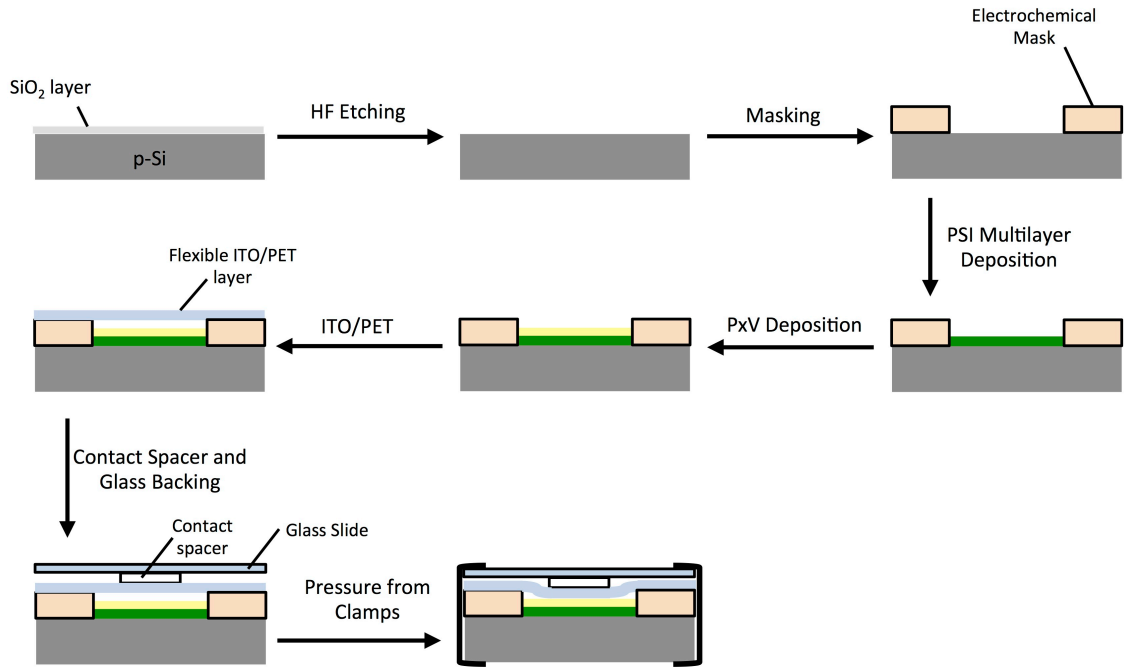

Figure 6.5. Fabrication Strategy for Solid-State pSi/PSI/PxV Solid-State Devices. Facile assembly occurred through a sequence of HF etching, masking, PSI deposition, polyviologen deposition, layering with flexible ITO/PET, and finally, pressing the conductive ITO onto the polyviologen, aided by a transparent contact spacer.

A PSI multilayer film was then deposited on the silicon substrate by drop casting approximately 100 µL of dialyzed PSI into the etched, unmasked area of the wafer. The solvent, and the protein precipitated into a film by sealing in a vacuum desiccator at reduced pressure for 15 minutes. This process was repeated 5 times to yield PSI multilayer films approximately 1 µm thick. An aqueous suspension of 10 mg/mL PxV was dropcast onto the PSI film within the electrochemical mask and the vacuum evaporation process was again performed. The PxV deposition process was repeated twice to ensure sufficient layer coverage of polymer on the protein film.

The device was completed with a conductive ITO film on flexible PET to act as the device anode. This was accomplished by resting the flexible metal oxide film on the mask, such that it was bridging the unmasked working electrode area but without

contacting it. Then a thin plastic spacer (2mm thick) was pressed into the backside of the PET, which was then topped with a glass slide. Binder clips forced the spacer into the ITO/PET layer to make secure electrical contact with the PxV layer without short-circuiting.

Device Testing

Solid-state p-Si/PSI/PxV/ITO devices were tested using previously described photochronoamperometric methods with brief modifications. Due to the solid-state nature of these devices, no liquid electrolyte was required, and thus a three-electrode setup was not appropriate. The reference and counter electrode lead wires from the potentiostat were connected to each other and attached to the ITO anode. The underlying silicon substrate was connected as the working electrode.

Similar to previous experiments, the dark open circuit potential was first determined for each device, and then this potential was used during photochronoamperometry experiments. After a 20 second period of dark baseline current measurement, samples were illuminated through the transparent glass/ITO layer.

Results and Discussion

Following the synthesis of PxV, the electrochemical properties of the material were evaluated in order to predict its usefulness when paired with PSI. An ideal electron accepting material for PSI would possess a redox potential slightly positive of the terminal F_B^- iron-sulfur cluster. Cyclic voltammetry revealed the redox potential of the $PxV^{2+/1+}$ couple to be -0.399 V vs. Ag/AgCl, as depicted in Figure 6.6.

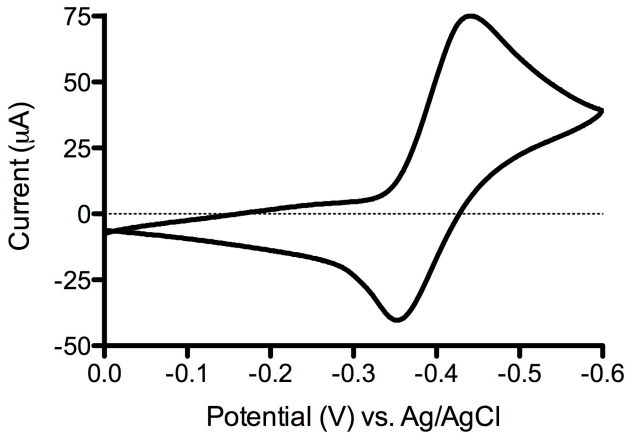

Figure 6.6. Cyclic Voltammogram of Poly(p-xylylviologen). Voltammogram was collected for aqueous solution of polyviologen supplemented with 100 mM KCl. Scan rate = 0.01 V/s, deoxygenated with bubbling argon.

The observed redox potential for PxV is in agreement with previous studies.[82] The value determined from Figure 6.6 corresponds to a potential of -0.202 V vs. NHE, which is energetically more positive than the reduced iron-sulfur cluster of PSI. This indicates that the synthesized polyviologen should act as a mediator from protein to polymer based on the favorable energy cascade. The ΔE_p between cathodic and anodic peaks is 90 mV, which indicates electrochemical reversibility. The reversibility of this system is essential in rapidly shuttling electrons from the protein to underlying ITO anode.

The polymer was also characterized via ^{1}H-NMR, shown in Figure 6.7, to identify the product, elucidate structural information about the material, and estimate average chain length.

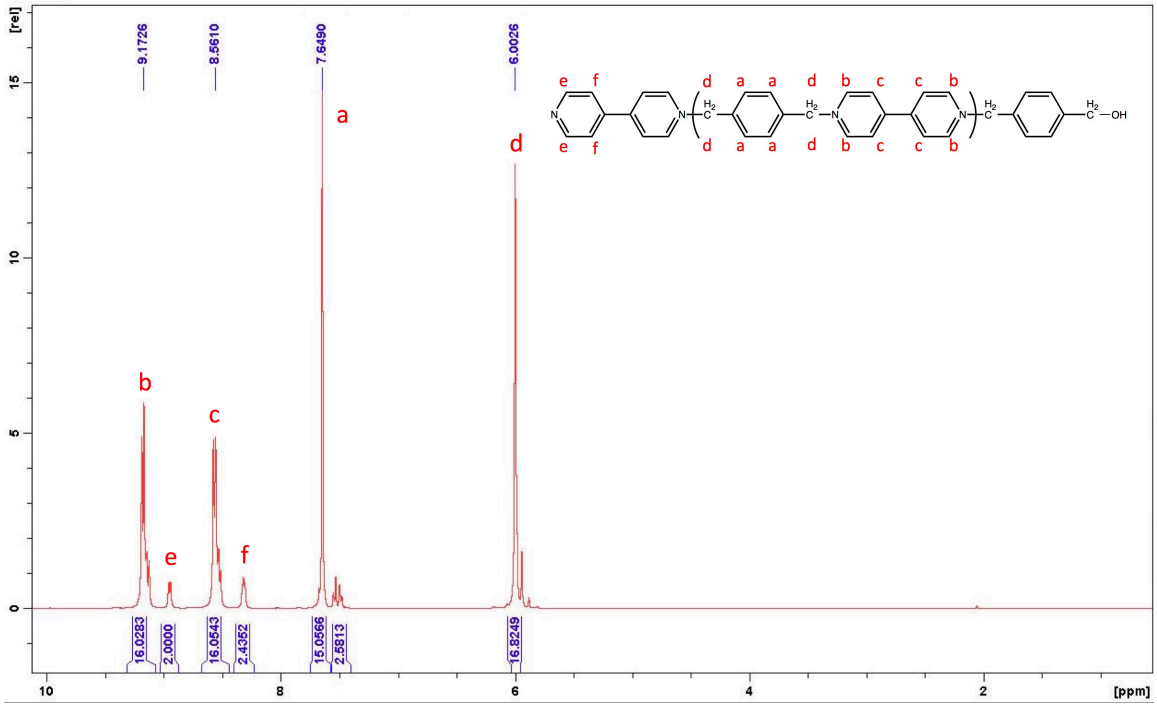

Figure 6.7. ^{1}H-NMR for Poly(p-xylylviologen). Spectrum was collected using 400 MHz spectrometer, with sample prepared in D_2O. Inset: structure of PxV with proton labels corresponding to the label peaks (a-f) in the spectrum.

From the NMR spectrum, four clear proton peaks are present which correspond to the four distinct proton types in the molecular structure (see inset). Peak a (δ 7.65 ppm) corresponds to the four equivalent protons belonging to the xylyl group in the repeating chain of the polymer. Peaks b (δ 9.17 ppm) and c (δ 8.56 ppm) represent the aromatic protons on the bipyridine system. Peak d present in the spectrum at 6.00 ppm represents the protons on the methyl groups bridging the two aromatic systems. Peaks a, b, c, and d all integrate to account for approximately the same relative number of protons in the sample, which correlates to the predicted polymer composition, and indicates that a copolymer with equimolar concentrations of each monomer type was synthesized.

For analytical purposes, the number average molecular weight (M_n) was calculated from the NMR spectrum. The proton signals corresponding to chain termini

were identified as peaks e and f, which arise from a bipyridine group ending the polymer chain. The integrations for these signals were normalized to 2 (the number of equivalent protons for each end group). This normalization resulted in an integration value of approximately 16 for peaks a, b, and c, all of which contain 4 equivalent protons. Based on the calculated proton ratios, the polymer sample as synthesized contains an average chain length of 8 repeating units. With a molecular weight of 260 g/mol for each repeating unit it was calculated that this polymer batch has approximate number average mass (M_n) of 2000 Da.

The PxV was used as prepared to fabricate solid-state p-Si/PSI/PxV/ITO solar cells. This proof-of-concept study first sought to determine if a solid film of PxV could act in series with PSI to provide an electron-mediating layer from protein to ITO and generate substantial photocurrent. This experiment set was carried out by layering PxV on top of PSI multilayers for solid-state devices, and as a negative control p-Si/PSI/ITO devices were tested without any PxV layer. It was hypothesized that the devices without any polymer layer would not produce substantial photocurrent.

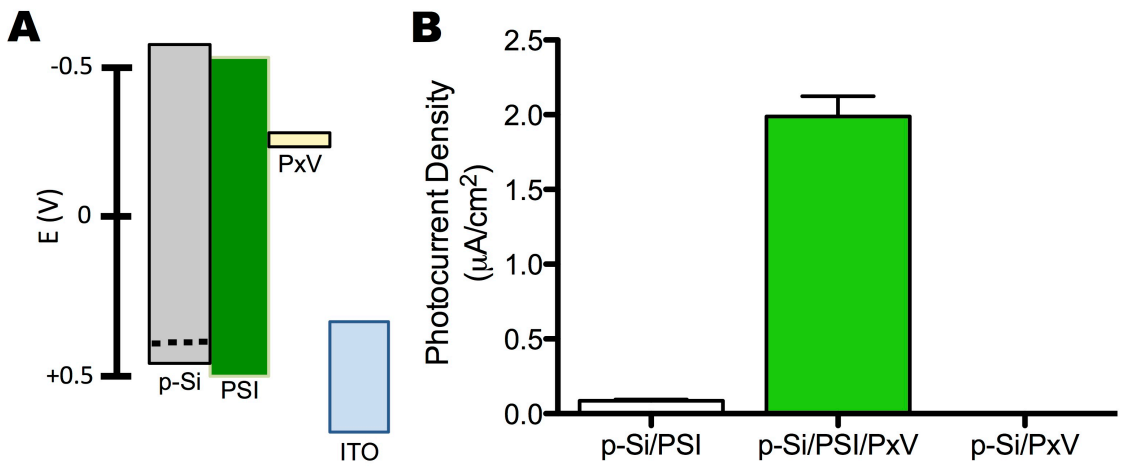

Figure 6.8. Relative Energy Levels and Performance of p-Si/PSI/PxV/ITO Solid-State Devices. A) Alignment of band energies for layers in the PSI/PxV solid-state devices. Band energies for Si and ITO and redox potential for PxV are presented relative to PSI. B) Photocurrent density for complete p-Si/PSI/PxV/ITO (green) and also control devices without PxV mediating layer (white), and without PSI layer (red).

As expected, the inclusion of the mediating layer between the PSI multilayer film and the ITO anode produced a significant amount of photocurrent (Figure 6.8B). As depicted in the relative energy diagram in Figure 6.8A, the position of the redox couple for PxV below PSI makes it a favorable energy transition. The cathodic polarity of the photocurrents in this experiment are in agreement with the predicted flow of electrons from silicon, through the PSI and PxV layers, and exiting the device through the ITO anode. The negative control experiments also validate the role of PxV in this device. For the device constructed without the PxV layer, very little photocurrent was produced (86 ± 9 nA cm^{-2}), likely due to the lack of charge mediation and poor electrical contact between the protein and the ITO electrode.

An additional negative control was added to the study, in which a p-Si/PxV device without PSI was tested. This study allows for the evaluation of photocurrent contributions that are directly derived from photoabsorption/excitation events that happen in the silicon or polyviologen layers. The photocurrent density (450 ± 70 pA cm^{-2}) for

this device type is presented in Figure 6.8B, where it barely rises above baseline. This minimal photocurrent response indicates that all photoactivated electron transfer processes are derived from the PSI layer and that PxV has virtually no photoactivity in the visible spectrum.

The use of a polyviologen analog to mediate electron transfer with PSI was also demonstrated by Yehezkeli et al, in which layers monolayers of PSI were assembled into a film with alternating layers of the redox active polycation.[86] However, this previous technology was constructed as a liquid cell requiring an exogenous, sacrificial electron donor. The newest proof-of-concept device presented in this chapter outperforms the previous state-of-the-art PSI/polyviologen type device, and also operates as a standalone solid-state unit. Elsewhere, viologen and polyviologen derivatives have been used as interfacial charge transport layers in polymer solar cells, thus indicating their future use in broad-scale photovoltaic development.[87–89]

Conclusions and Future Directions

A simple polyviologen, poly(p-xylylviologen), was synthesized and then characterized electrochemically to predict its electronic matching with PSI. When fabricated into simple devices, photocurrent generation was tested, and the role of the polymer in mediated electron transport was validated. In control devices where no polymer was deposited, there was a significant suppression of photocurrent.

Many additional studies must be performed to fully explore PxV, and other polyviologens, in this application. Specifically, film thickness optimization of the PSI and PV layers, as well as improving uniform surface coverage of the PV layer on the PSI film to maximize photoelectron transfer. Additionally, further device efficiency could be

improved with alternative viologens with tuned redox properties and electron diffusion coeffecients. This could be accomplished by modifying the N-alkyl linkers in the polymeric units, or adding electron donating or withdrawing substituents to the 2,3 position(s) of the bipyridines.

With the preliminary data collected on these novel, solid-state PSI/PxV devices, there appears to be great promise for polyviologens as an avenue for constructing simple solid-state biophotovoltaics. Further improvement in these devices can be found enhancement of the robustness of these devices. This could potentially be achieved by moving away from flexible ITO layers held on the device by force clamping, and instead RF sputtering a thin ITO film onto the PV layer. This anode deposition would introduce new opportunities for creating new, stand-alone, large-scale (100 cm^2), deliverable photovoltaic devices.

Chapter 7

LOW RESOURCE PHOTOSYSTEM I EXTRACTION AND ULTRA-FACILE BIOHYBRID DEVICE FABRICATION

Introduction

Major advances have been made in Photosystem I-based photovoltaic devices in the last decade, and many of these technological breakthroughs have utilized increasingly sophisticated materials. These materials can often be expensive, rare, or difficult to manufacture. Solar-grade silicon has been used in several PSI device types and although elemental silicon is not rare, it requires energetically intensive industrial processing to produce a pure form of the material for this application. Interestingly, it was previously determined that for a p-Si/PSI/ZnO/ITO device (Chapter 6), greater than 90% of the material cost of the entire device was derived from the silicon wafer.

PSI is an attractive material to use in new photovoltaic technologies because of its natural abundance and simplicity. Since it can be extracted from a wide variety of plant materials found in many environments, PSI has the potential to be implemented on a global scale for low-cost solar energy conversion. Currently, PSI is harvested from commercially available plant sources, using an extraction protocol that requires extensive laboratory knowledge and specialized equipment.

Thus when considering the cost of some materials used in state-of-the-art devices, and the intensive nature of the PSI extraction procedure, it becomes apparent that PSI-based solar cells are not in an advantageous position for low-cost scalability. This goal of this chapter is to develop a streamlined, modified extraction procedure for PSI that could

be carried out by an individual with limited chemistry knowledge and experience, and eventually interface the extracted PSI with low-cost materials with minimal processing to develop a simple photovoltaic device.

Applications for this research are found in a variety of low resource settings. Most practically, this information will be distributed to local metro and rural schools where students can carry out the rapid extraction and device fabrication for educational purposes. Ideally, the extraction protocol should demand practical chemical expertise of a high school-level student, and require only materials that can be procured from local grocery, home improvement, or craft stores. The long-term goal for the ultra facile PSI extraction is to deploy this technology in modular form into low resource settings. This would allow for the extraction of PSI from any locally sourced green plants, and subsequent utilization of that PSI in the fabrication of small solar energy conversion devices constructed in the field and used to power small electronics.

First, the current extraction methods must be addressed. Currently, the process involves simple maceration, filtration, two centrifugation steps, and column chromatography. The biggest restrictions on this process are found in the high speeds required for the centrifugation steps, 8,000 x g and 20,000 x g, and the column separation. The two centrifugation steps are present in the current protocol to pellet the chloroplasts, and precipitate the insoluble material after membrane lysis. Thus, a new streamlined protocol needs to eliminate at least one of the spin cycles, and reduce the required rotor speed, which in turn would eliminate the need for a more costly instrument. Precipitation of the spinach sub-organelles can be achieved at a relatively low speed, and thus can be reasonably accomplished using a low-grade commercial

centrifuge. Alternatively, the second centrifugation cycle at 20,000 x g requires a specialized centrifuge apparatus and the necessity of this step is minimal when the desired outcome of the extraction is speed and ease, not purity.

Finally, the use of hydroxylapatite as a stationary phase is very simple in the current extraction format. The isocratic elution conditions using a high concentration of phosphate is very user-friendly. However, the scale of this column separation needs to be downsized to make it faster and more reliable. To solve this, an improvised flash column, made from a Pasteur pipet packed, with less than 0.5 g of hydroxylapatite will serve as the separation column. A basic outline for the new extraction method is depicted in Figure 7.1.

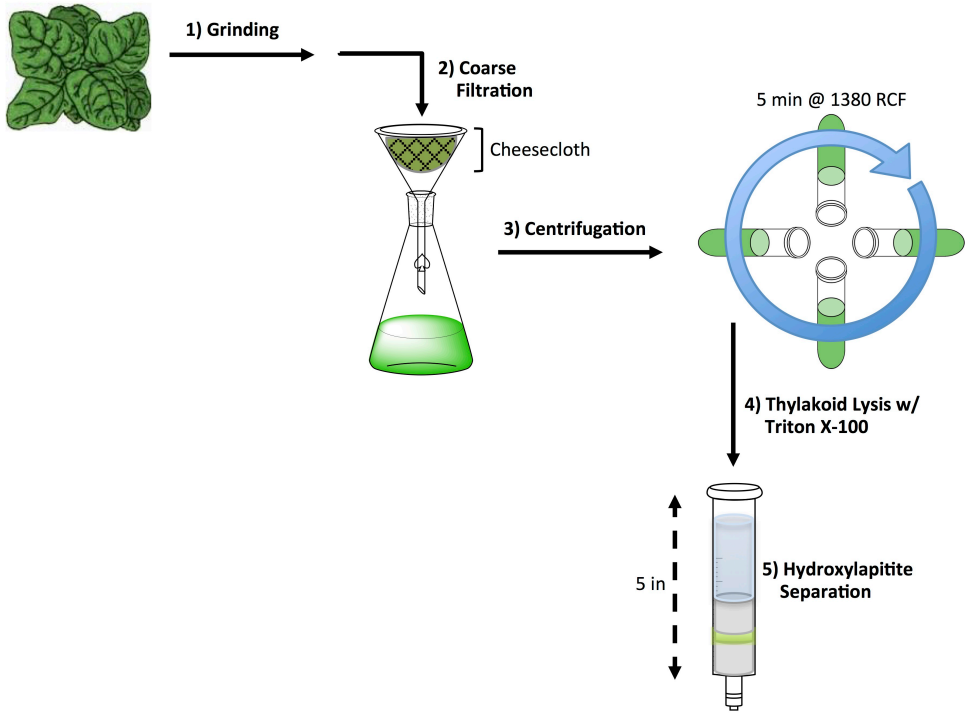

Figure 7.1. Outline of Low Resource Photosystem I Extraction. The process involves 1) grinding of the spinach leaves, 2) filtration with layers of cheese cloth, 3) low speed centrifugation to precipitate chloroplasts, 4) PSI solubilization with Triton X-100, and 5) hydroxylapatite separation using a Pasteur pipet or syringe body as an improvised column.

With these simple protocol modifications, we have altered the procedure for PSI extraction and created a more practical approach. This chapter outlines the newly developed method and describes future plans for rapidly fabricating simple photovoltaic devices from the extracted protein.

Experimental

Rapid Extraction of Photosystem I

This extraction was designed with careful consideration for the materials, reagents, and equipment required to carry out the process, as well as time and expertise required by the operator. Reagents can all be easily obtained from chemical vendors at minimal cost, are considered to be environmentally benign, and have long shelf lives. Most materials could be procured from local craft or hardware stores. The centrifuge used in this extraction was a Fisher Centrific™ Model 228, which is a rudimentary tabletop centrifuge usually available for less than $300. These centrifuges are very robust, with maximum RCF of 1,380 x g, and are commonly found in teaching laboratories of high schools and undergraduate institutions. The total extraction was targeted for a completion under time 2 h.

Approximately 48 g of spinach leaves were placed in a household blender with 100 mL of Grinding Medium (330 mM sorbitol, 10 mM sodium pyrophosphate, 4 mM calcium chloride, and 2 mM ascorbic acid). The spinach was ground into a smooth homogenized mixture. This mixture was then coarsely filtered through 8 layers of cheesecloth. The filtrate was divided into 4 centrifuge tubes, balanced by approximate volume, and then loaded into a Fisher Model 228 centrifuge. The samples were spun at

1,380 x g for 1 min. After the centrifugation cycle was complete, the supernatant was discarded.

The pellets of broken chloroplasts were resuspended using a minimal volume (approximately 1 mL) of Resuspending Medium (50 mM HEPES pH = 7.6, 330 mM sorbitol, 2 mM EDTA, 1 mM magnesium chloride, 1 mM manganese chloride, and 1% Triton X-100). This surfactant-rich media is used to lyse the thylakoids and solubilize the PSI. All of the resuspended pellets were combined into a 15 mL centrifuge tube and shaken vigorously. The suspension was allowed to incubate with the surfactant solution for 15+ minutes while the improvised separations column was set up.

A 5-3/4" Pasteur pipet was clamped securely in the vertical position such that it could be used as a makeshift vessel to hold the hydroxylapatite resin. A small piece of glass wool was pushed all the way to the neck to the pipet to keep the resin in the column. 0.3 g of hydroxylapatite was slurried with Column buffer (20 mM phosphate buffer, pH = 7.00). The slurry was then poured into the pipet and allowed to settle into a packed resin bed. Column buffer was continually added atop the stationary phase to ensure proper packing.

Once the column was prepped, the membrane lysate was loaded into the column, and allowed to flow over the hydroxylapatite. Column buffer was continually added to wash through any non-bound material. The initial green eluent was collected and later discarded. Occasionally, a pipet bulb was loosely affixed to the top of the pipet and compressed to pressurize the headspace of the column and force buffer through the column. Once the eluent returned to colorless, the buffer was switched to Elution buffer (200 mM phosphate buffer with 0.05% Triton X-100, pH = 7.00). The Elution buffer was

continually added to collect the purified PSI from the column. This eluent was collected as purified PSI. The bulk PSI solution was aliquoted into smaller volumes and stored at -80 °C for later use.

A P700 concentration assay was performed on the PSI collected using this new protocol, with the methods described in Chapter 2.

Results and Discussion

The newly developed extraction procedure was comparatively very streamlined, over the traditionally used method (Chapter 2). The entire process can be completed in less than 2 hours, which is a vast improvement over the 6+ hours required for running a large-scale extract with a traditional hydroxylapatite column. A table summarizing the results of this new rapid extraction procedure, and comparisons to the traditional method, are presented in Table 2.

Based on the column format, and limited resin bed volume, only a modest amount of purified PSI (by volume) was harvested. In this extraction, approximately 10 mL of PSI was collected. In using 0.3 g of hydroxylapatite, it is expected that the resin quickly became saturated, and a majority of the protein that entered the column did not interact with the stationary phase. However, this could be remedied easily by increasing

Table 7.1. Comparison of Results between PSI Extraction Types

Extraction Type	Time Required, Hours	Yield, mL	[P700], µM
Traditional	> 6	Approx. 200	0.5-2
Rapid, Low-Resource	< 2	Approx. 10	1.7

the amount of hydroxylapatite and/or using a larger column. This `optimization comes at the sacrifice of time required to complete the extraction procedure. Thus in order to maintain the rapidity of this purification strategy, a minimal amount of hydroxylapatite was used.

The final separation stage of this rapid extraction could potentially be further improved by switching from a glass Pasteur pipet (I.D. = 5.76 mm) to a small plastic syringe body with the plunger removed. This format allows for a wider column, which could handle a larger volume of hydroxylapatite, or the same 0.3 g quantity of resin with a decreased the column length. The accompanying plunger could also be used to apply gentle pressure to the separation column for improved separation time and more concentrated PSI eluent.

PSI collected using this modified procedure was evaluated by a typical Baba Assay, in which the active P700 concentration of the sample was determined. The assay revealed that active PSI was extracted using this streamlined procedure, and that PSI was collected in a concentration of 1.7 μM, which is comparable to the previously used, full-scale extraction procedure.

Further characterization was performed using SDS-PAGE. This method allows for the qualitative assessment of protein subunits present in the extracted sample. For comparative purposes Photosystem II, extracted using a different method, was also analyzed. The gels are presented in Figure 7.2.

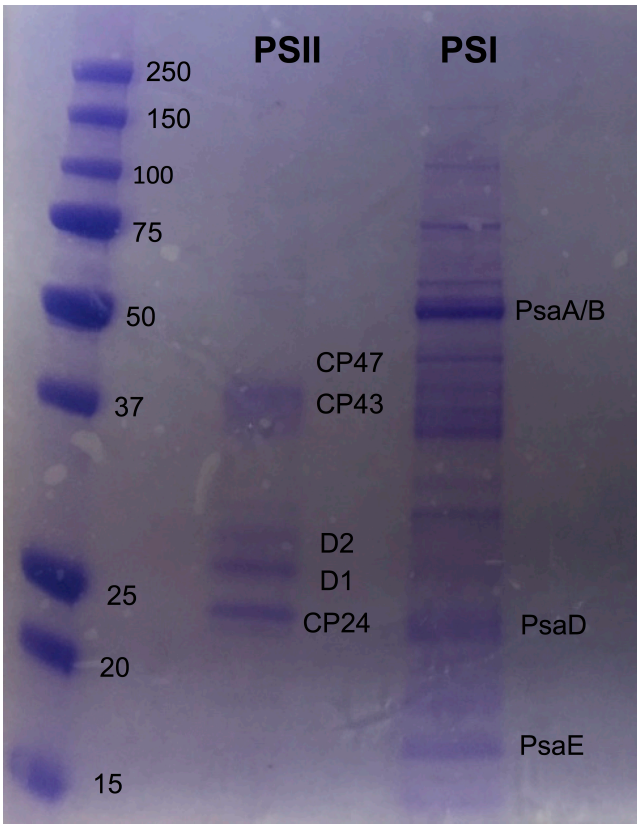

Figure 7.2. SDS-PAGE of PSI Extracted with Low Resource Method. PSI was extracted using the novel rapid extraction protocol. The concentrated band near 50 kDa is representative of the PsaA and PsaB subunit heterodimers specific to PSI. Other smaller peripheral protein subunits of PSI are also present in the lower mass regions. PSII was also loaded onto the gel for comparative purposes.

SDS-PAGE of PSI indicates several of the key PSI-specific protein bands. Uniquely, a dark band appears near 50 kDa, which corresponds to the hallmark PsaA and PsaB heterodimer subunits. This is a clear indicator that a substantial quantity of intact PSI was collected using this new extraction method. Additionally, some smaller subunits of PSI have been identified in the gel, i.e. PsaD and PsaE. It is worth noting that many other bands are present in the gel lane. This can be attributed to the hastiness of purification in this process. The rapidity of the extraction compromises absolute purity in the final product, which is to be expected.

There are bands present in the PSI lane that could be attributed to residual PSII that was not removed by high-speed centrifugation (20,000 x g for 15 min). However, there are not bands present in the PSII same near 50 kDa, indicating that the protein sample extracted using this new method contains high molecular weight polypeptides, which likely belong to PSI. This data in conjunction with the photoactivity assay indicates that our modified extraction procedure was successful in harvesting photoactive, chlorophyll-containing protein complexes.

Conclusions and Future Directions

In this chapter, a new method for the extraction of PSI from spinach leaves was presented. This protocol greatly streamlines the process by eliminating a high speed centrifugation step, and also downsizes the column separation to that of a 0.3 g hydroxylapatite resin bed in a Pasteur pipet. A adequate amount of PSI was extracted through this method, and it was assayed to determine an active P700 concentration of 1.7 μM, which is comparable to PSI extracted using the previously devised full scale protocol.

With this newly developed method for PSI extraction, the immediate objective is develop a small-scale photovoltaic cell that can be built using the extracted protein. Utilizing low-cost materials for this fabrication are key. Some materials to be explored include: organic polymers, metal oxides, and carbonaceous substrates. Future studies that seek to continue this project can construct simple devices using the PSI extracted from the methods in this chapter. Metal cathodes have been shown to interface very well with PSI in previous studies. Gold was one of the earliest materials for PSI devices,[90,91] and later solid-state devices utilized silver or aluminum cathodic layers.[36,80] Thin metallic

foils are available at craft stores and are a low cost option for crude biohybrid devices. The proposed device will be fabricated by first affixing a metal foil, such as gold leaf, to a glass slide for structural support. Upon this substrate, a multilayer of extracted PSI will be deposited. An interfacial electron transport layer such as poly(p-xylylviologen) will then be added onto the PSI multilayer. This can be rapidly assembled into a very thin layer by spray coating a solution of polymer onto the protein film using an airbrush purchased at a craft store. Finally, ITO with a flexible polymer backing will be pressed onto the polyviologen layer to act as the transparent device anode.

Ideally, modular kits will be assembled that include all the components required to extract PSI from any locally available green plant, and then assemble a PSI solar cell. This project has immense broader impacts in the enrichment of science students through hands-on demonstrations that can be performed in any classroom setting. Additionally, a modular, deployable kit for fabricating solar cells from green plants would be invaluable for powering small electronic devices in low resource environments where traditional power grids do not exist.

Chapter 8

OSMIUM-POLYMER BASED ELECTROCHEMICAL BIOSENSORS FOR ORGAN-ON-CHIP SYSTEMS

Introduction

Based on the liver's role as a metabolic center of mammalian systems, understanding the behavior of this organ is of unique importance in studying the way therapeutics are processed. A number of drug candidates fail due to toxicity, the majority of which is centralized in the liver or induced through the generation of toxic secondary metabolites.[92] Thus many chemical-based therapies pose a particular risk to liver health. These failures can be severely consequential for researchers, pharmaceutical companies, and trial participants, alike, providing the impetus that has pushed the development of improved preclinical *in vitro* models to reduce enormous financial and ethical burdens that often plague drug development.[93]

For an *in vitro* preclinical system to be effective, it must allow for cellular-level changes to be observed and modeled in response to an influx of drug/toxin. Optical and fluorescence-based cytometry in screening have proven to be powerful assay tools, but these methods can also be costly and time consuming. Electrochemical screening, however, represents a much more rapid methodology for real-time bioenergetic profiling.[94] The use of electrochemical methods to monitor real-time cellular responses has been utilized for a wide variety of biological systems. Glucose is the most widely monitored metabolite via electrochemical methods, as evidenced by the breadth of glucose sensing technologies developed in the last decades, most notably rapid glucose

diagnostics in the form of single-use test strips for hypo/hyperglycemia.[95] Most commonly, glucose sensing is carried out amperometrically using an enzyme, glucose oxidase (GOx), immobilized on an electrode. Electrons from substrate oxidation and are harvested by the sensor electrode and transduced as a signal. Based on their generally low-cost, availability, and facile fabrication, enzymatic biosensors have been widely used in electrochemical measurements.[96]

Additionally, the use of multiple enzymatic biosensors on a single sensor array has provided a multiplexed approach to studying analyte changes in a dynamic biological system in real time. Noteworthy examples of multianalyte, electrochemical biosensing have studied stimulated endocrine responses,[97] macrophage immunoresponses,[98] neuronal responses to ischemia,[99] and metabolic cellular responses to cholera toxin exposure.[100] Major advances in electrochemical metabolic profiling were made through the creation of the MicroClincal Analyzer, a modular analytical component of an Organ-on-Chip system outfitted for the real-time measurement of glucose, lactate, oxygen and extracellular acidification.[101,102] Although versatile in studying a wide variety of novel systems, it is currently incompatible with Liver-on-Chip systems.

Due to the nature by which hepatocytes process xenobiotic compounds through oxidative, reductive, and/or hydrolytic pathways, many compounds of relevance to liver health demonstrate inherent redox activity.[103] Consequently, redox active drugs, toxins, and small molecules of interest to liver systems act as amperometric interferents during *in vitro* studies. To this extent, acetaminophen (APAP) is a model compound due to its clinical relevance, acute hepatotoxicity, and known redox activity. The known redox activity of APAP makes this compound problematic for traditional enzymatic biosensors

that utilize high amperometric detection potentials. These sensors rely on immobilized oxidase enzymes for specific analyte quantification through the production of hydrogen peroxide upon substrate (e.g. glucose) oxidation. As depicted in Figure 8.1, GOx oxidizes glucose to produce glucono-δ-lactone (GDL). Meanwhile, dissolved oxygen in proximity to the enzyme acts as coreactant and electron acceptor to the enzyme, producing H_2O_2. Subsequently, the oxidation of localized hydrogen peroxide at the electrode surface is observed as an amperometric signal. Based on the high electrode bias required to oxidize hydrogen peroxide, the oxidation of electroactive APAP, present in complex biological matrices, to N-acetyl-p-benzoquinone imine (NAPQI) will mask any relevant analyte changes.

An effective strategy to circumvent the interference of redox active compounds present in biological matrices is voltammetric discrimination of analyte and interferent.[104] This is accomplished by catalytically minimizing the overpotential required for analyte detection to a potential window in which interferents are not redox active. In the case of APAP, an electrode potential less than +0.3 V (vs. Ag/AgCl) must be utilized to negate any signal contributions from the background reaction. A popular route to achieve this is accomplished through the use of various metallic or metallized substrates to catalyze the reduction of peroxide at a lower overpotential; Au, Pd, Ru, Rh and their alloys have yielded promising results.[105–107] However, these material are often unstable or prohibitively expensive, leaving doubts about their widespread implementation in analytical detection systems.

In this work, we utilize a low detection potential bias for the simultaneous, amperometric sensing of changes in multiple analytes in media containing a high

concentration of APAP. The concentration of APAP used in these studies is 10 mM, which is far beyond clinically relevant limits. This level was selected for later studies of acute induced hepatic necrosis. This is achieved through the inclusion of a wired, redox hydrogel that serves as an immobilization matrix for the enzyme and provides and a tethered redox mediator between enzyme and electrode.

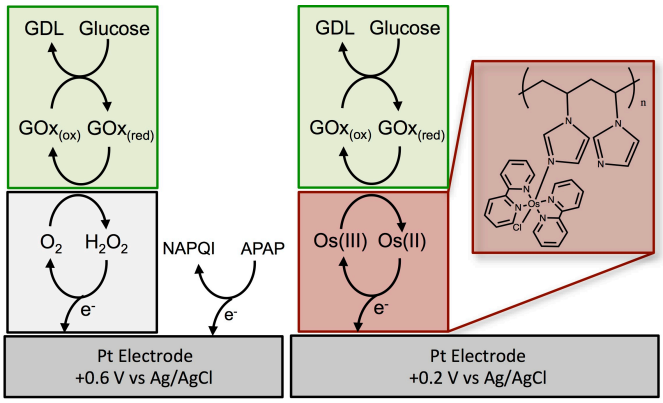

Figure 8.1. Redox Processes of Traditional and "Wired" Enzymatic Glucose Sensors. Left: a traditional sensor is depicted where electron transfer between enzyme and electrode is mediated by dissolved oxygen. Right: the enzyme is crosslinked within a wired redox polymer network, which facilitates interfacial electron transfer, at a lower oxidation potential. The high electrode potential required to transduce a peroxide signal in the traditional system also readily oxidizes acetaminophen (APAP) in the matrix. The electrode bias of 0.2 V required for the GOx/Os-polymer system mitigates any oxidative signal from APAP present in the sample.

Osmium containing redox polymers were first developed by Heller et al. in the late 1980s for use primarily as glucose biosensors.[108] These metallopolymers are highlighted by a water-soluble polyvinylpyridine (PVP), or polyvinylimidazole (PVI), backbone with osmium-bis(2,2'bipyridine)chloride complexes coordinated to the polymer through the nitrogen atom of the heterocycle side chain. Covalently linking of GOx into a redox active hydrogel provides an enhanced pathway for electron transfer from the FAD/$FADH_2$ cofactor of the enzyme, thus improving sensitivity and selectivity

of the enzymatic sensor. In this sensor type, analyte quantification is determined by the amperometric signal transduced by the turnover of the $Os^{3+/2+}$.

The advantage of using tethered osmium complexes is found in the unique and tunable redox potential of the hydrogel-bound mediators. For this application an Os-polymer with a redox potential of approximately +0.2 V is desired. This specific potential is ideal for accepting electrons from a reduced $FADH_2$ cofactor of an oxidase enzyme to yield $[Os(bpy)_2Cl(PVI)]^{2+}$. The reduced Os-complex can then be reoxidized back to its +3 state by applying an electrode bias that is slightly oxidizing relative to the redox potential of the coordination complex. This detection potential is below the onset oxidation potential of APAP and avoids possible amperometric interference.

In studying an *in vitro* Organ-on-Chip system, it is desirable to concurrently monitor multiple analyte changes to better understand modes of action and elucidate the pathways responsible for hepatotoxicity. To this end, glucose, lactate, and glutamate were chosen as the three analytes of interest due to their relevance in basal and trauma-induced metabolic activity and widely available enzyme oxidases (i.e. glucose oxidase, lactate oxidase, and glutamate oxidase). Glucose and lactate play active roles in several key metabolic processes in liver cells, including glycolysis, glycogenolysis, and gluconeogenesis.[109]

Where as glucose and lactate fluxes can be used to monitor metabolic changes in normal hepatic cell proliferation, glutamate flux can be used as a marker for stress in hepatic systems under induced acute toxicity. In a clinical setting, an assay of aspartate aminotransferase/alanine aminotransferase (AST/ALT), and their relative ratio, in patient serum is used to identify hepatotoxicity. Increased levels of AST and ALT stand as a

marker for hepatocellular necrosis. Both aspartate and alanine aminotransferase yield L-glutamate as a product of their substrate turnover,[110] thus increased concentrations of L-glutamate found downstream from a liver bioreactor or Liver-on-Chip system would indicate the presence of AST and/or ALT, and the prerequisite hepatocyte necrosis. Several electrochemical assays for AST/ALT have been developed that utilize glutamate oxidase to quantify changes in sample media. However, based on the dependence of these sensor types on the oxidation of hydrogen peroxide to yield an amperometric signal, the effect of electroactive drugs/toxins (e.g. APAP) and the effect on AST/ALT release have not been studied due to the likely interferent effects introduced by background oxidation signals.

In the present work, we present a multianalyte sensor platform, which utilizes glucose, lactate, or glutamate oxidase coupled to redox hydrogels to independently quantify glucose, lactate, and glutamate signals in real time, at a low oxidation potential, over a background of 10 mM APAP. Together these tools represent a new method to rapidly analyze Liver-on-Chip systems to electrochemically monitor cellular viability, perform toxicity screenings, and possibly elucidate metabolic pathways. Herein, real-time changes in the concentrations of three analytes were simultaneously recorded and calibrated using a series of standards spiked in buffer. The calibrations performed in this work cover biologically relevant dynamic ranges. Additionally, selectivity assays were performed to demonstrate that this multianalyte sensor platform is insensitive to high concentrations of APAP, and longevity studies of sensor performance were also carried out to validate this platform's ideality for interfacing with continuously operational Liver-on-Chip systems.

Experimental

Apparatus

Screen printed electrodes (SPE), described elsewhere,[111] serve as the underlying multianalyte sensor head for this platform. Briefly, this SPE features three parallel 1.5 mm diameter disk platinum working electrodes, a 2 x 10 mm rectangular platinum bar that serves as the auxiliary/counter electrode, and a very small 0.08 mm^2 electrode that was silver-plated to serve as a reference electrode. This entire electrode array is then sealed into a 26 µL flow chamber for flow-based electrochemical analysis. Each working electrode was modified for a specific analyte of interest to allow for the independent monitoring of changes in each concentration over time. Figure 8.2 presents a model of the modified SPE assembled in the flow chamber.

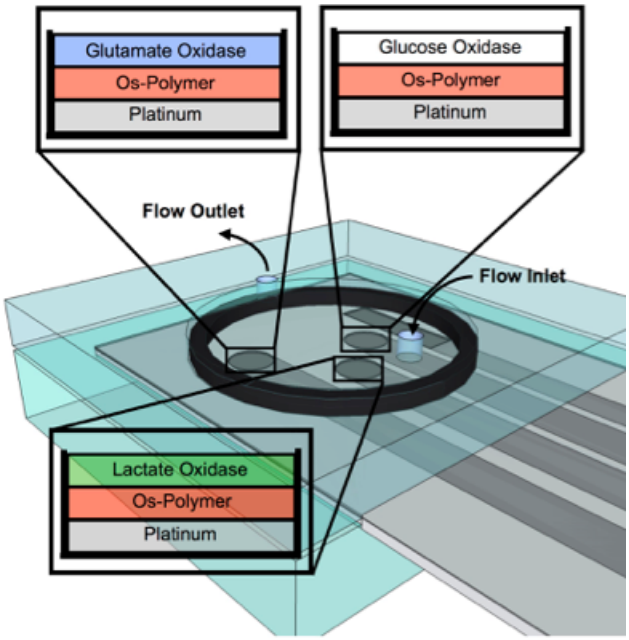

Figure 8.2. Modified Screen Printed Electrode in Flow Chamber. Representation of the assembled flow chamber apparatus used for this study. Three independent working electrodes are used on the chip, each with diameter of 1.5 mm. The compositions of glucose, lactate, and glutamate sensitive electrodes are shown in the insets for each respective electrode type. A platinum bar electrode (0.19 cm^2) serves as the auxiliary electrode.

Materials

N-vinylimidazole, azobisisobutyronitrile (AIBN), 2,2'-bipyridine, ammonium hexachloroosmate(IV), and polyethylene diglcidyl ether (PEGDGE), were purchased from Sigma Aldrich. Glucose oxidase (GOx) (152.54 U/mg) and lactate oxidase (LOx) (11.29 U/mg) were purchased from Applied Enzyme Technology. L-glutamate oxidase (EOx) was purchased from Yamasa Corporation. The N-vinylimidazole monomer was purified via vacuum distillation prior to use. However, all other reagents were used as received and without any additional purification.

Preparation of Os-loaded Metallopolymer

Osmium-containing redox polymer, $Os(bpy)_2Cl$-PVI was prepared according to various protocols described previously.[112] Poly(N-vinylimidazole) (PVI) was prepared through free radical polymerization using AIBN as the initiator. Freshly distilled N-vinylimidazole monomer was combined with AIBN (60:1 ratio of monomer to initiator) in absolute ethanol in a N_2 purged flask. The reaction mixture was heated to 70 °C for 12 h to induce complete polymerization. The resulting solid was purified by dissolution in additional ethanol overnight, and then precipitation in rapidly stirring diethyl ether. The solid was separated on a coarse frit, followed by additional washes with diethyl ether, and drying under vacuum.

Osmium[bis(2,2'-bipyridine)dichloride] ("$Os(bpy)_2Cl_2$") was synthesized by refluxing ammonium hexachloroosmate(IV) with 2-molar equivalents of 2,2'-bipyridine in ethylene glycol for 2 h.[113] Excess aqueous sodium dithionite (approx. 0.1 g/mL in DI water) was then added dropwise to the stirring reaction mixture to ensure that all Os-complexes were present in the Os(II) state. The reaction mixture was then chilled on dry

ice and filtered using a fine (4-5.5 μm) sintered glass funnel. Once filtered, the product crystals were washed with three small volumes of cold water and then dried on the frit under vacuum for 1 h, and in an oven at 65 °C overnight.

The prepared $Os(bpy)_2Cl_2$ was loaded onto the PVI side chains by refluxing together (in 3:4 Os to imidazole ratio) in absolute ethanol for 5 d. Following the reflux period, the reaction mixture was added dropwise to a stirring volume of diethyl ether. This polymer-ether mixture was then chilled on dry ice and the precipitate was filtered on a fine sintered glass funnel. The $Os(bpy)_2Cl$-PVI product was then washed with excess volumes of cold ether to remove unbound $Os(bpy)_2Cl_2$ and subsequently dried under vacuum for 15 min. The product was then dried further by transferring to a round bottom flask and holding under vacuum ($<10^{-4}$ Torr) overnight.

Electrode Modification

To prepare a sensor chip capable of flow-based electrochemistry, one of the electrodes on the sensor array was modified to act as a reference electrode. This was accomplished by depositing a thin layer of Ag/AgCl onto the small 0.08 mm^2 electrode on the chip. The plating solution was comprised of an solution of 0.3 M $AgNO_3$ and 1 M NH_4OH, An external Ag/AgCl (3M KCl) reference electrode and Pt mesh counter electrode were used for the silver deposition. First, a preconditioning step was applied with a bias of +0.95 V (vs. Ag/AgCl) for 30 s, which was then immediately followed by galvanostatic plating at a cathodic current density of 6.5 mA/cm^2 for 450 s. Following plating, the AgCl layer was generated on the freshly plated silver by soaking in 50 mM $FeCl_3$ for 1 min.

Enzyme films were prepared using a dropcast method in which 0.5 μL aliquots of a metallopolymer-enzyme solution were deposited onto the 1.5 mm diameter disk electrodes intended for amperometric analyte detection. Films were dried at room temperature, prior to being moved to the refrigerator for overnight crosslinking at 4 °C. Glucose specific electrodes were modified with a stock solution 5 mg/mL glucose oxidase, 20 mg/mL $Os(bpy)_2Cl$-PVI, and 1% (v/v) PEGDGE. Lactate specific electrodes were prepared similarly, except 5 mg/mL lactate oxidase was used in the stock solution. Further, glutamate specific electrodes were prepared from a nearly identical stock metallopolymer-enzyme solution with glutamate oxidase at a concentration of 1 mg/mL.

Titrations

Amperometric titrations were performed using the modified screen printed SPEs assembled into a magnetically sealed acrylic flow chamber, with an O-ring sandwiched tightly onto the SPE chip face to provide a defined flow chamber volume. A downstream syringe pump operating in pulling-mode drove flow in this setup. Thus, the pump operated by drawing solution from each vial of standard. The syringe pump operated at a flow rate of 100 μL/min for all experiments. A CH Instruments (Austin, TX) 1440 multichannel potentiostat was used to record three independent amperometric signals (glucose, lactate, and glutamate). For the amperometric channels, the electrode bias was held at 0.2 V (vs. quasi-Ag ref) at a sampling frequency of 1 sec^{-1}. Standards were prepared in phosphate buffer (1 mM, pH = 7.00) with 120 mM KCl and 10 mM APAP. Each calibrant solution contained an increasing quantity of glucose, lactate, and glutamate such that simultaneous calibrations could be performed for each analyte. The

analyte ranges used in this study were: glucose 0 – 25 mM, lactate 0 – 3 mM, and glutamate 0 - 1 mM.

Results and Discussion

$Os(bpy)_2Cl$-PVI synthesized using the aforementioned protocol was characterized by cyclic voltammetry to verify its utility in this sensor type. A redox potential of approximately 0.2 V vs Ag/AgCl is optimal for accepting electrons from the oxidase enzymes. Further a low electrode potential required to oxidize the Os-complexes, and turnover the enzyme would avoid interference from electroactive compounds in the matrix, i.e. acetaminophen. A cyclic voltammogram for a handcast film of Os-polymer crosslinked with GOx is presented in Figure 8.3

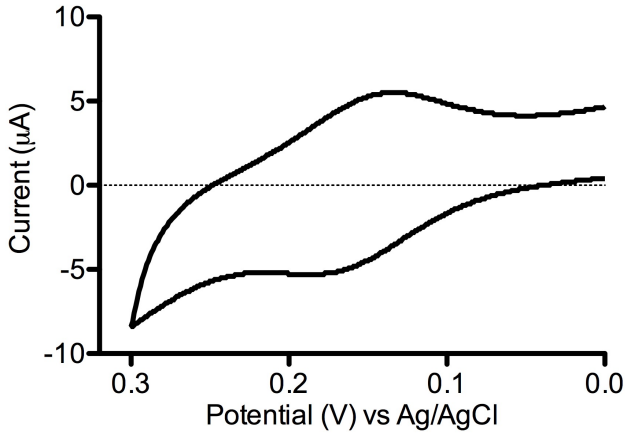

Figure 8.3. Cyclic Voltammogram of Os-polymer Modified SPE. Os-polymer immobilized on an SPE working electrode along with GOx, and characterized in the presence of 10 mM APAP. Scan was performed with assembled 26 μL flow chamber using integrated auxiliary and Ag/AgCl reference electrodes on the chip. Scan rate was 100 mV/s.

The redox peak near 0.18 V corresponds to the osmium complexes tethered within the hydrogel network. This voltammogram was collected in APAP-rich buffer, such that the onset of APAP oxidation can be observed near 0.25 V. The separation of

osmium and APAP oxidation events indicates that this redox polymer is an ideal choice for this biosensor type and that an electrode bias of 0.2 V will induce the turnover of the Os-polymer immobilized on the electrode surface without oxidizing APAP in the bulk solution.

Through the modification of the SPEs with enzyme films and osmium containing redox polymers, calibrations were performed for glucose, lactate, and glutamate in PBS spiked with a high concentration of acetaminophen. The titration was carried out by simultaneously recording independent amperometric signals under constant sample flow. A typical multianalyte calibration is presented in Figure 8.4, where the current was recorded over a total span of 1500 s, during which calibration solutions with increasing glucose, lactate, and glutamate were switched every 300 s. By utilizing the electrode bias of 0.2 V for glucose, lactate, and glutamate sensors, the interferent effects of APAP have been mitigated. Additionally, the observation of an anodic (negative) current in these sensors confirms the predicted electron flow mechanism, in which electron donation occurs from $FADH_2$ of the oxidase enzyme to Os^{3+}. Subsequently, the donation of electrons from the reduced osmium complex to the underlying electrode is observed as anodic current.

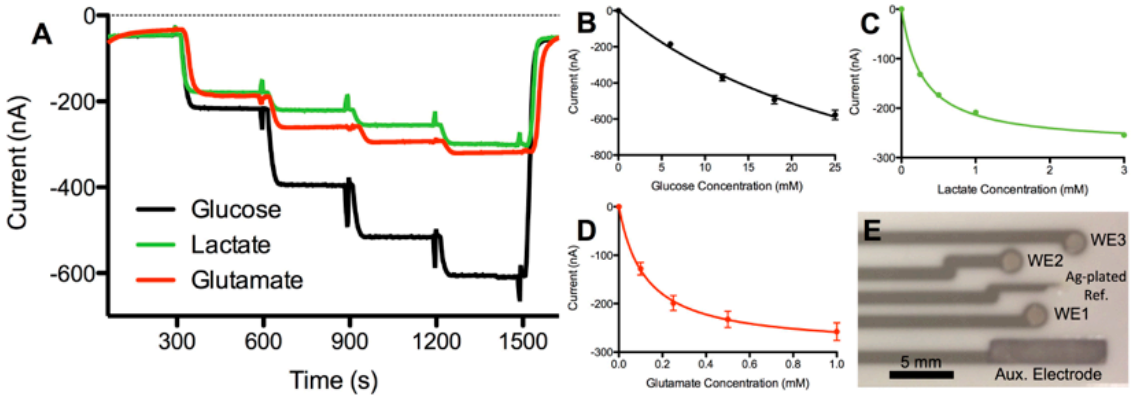

Figure 8.4. Multianalyte Titration of Oxidase Os-Poly Sensors and Simultaneous Calibration Curves. A) A typical multianalyte titration carried out using a three electrode SPE modified with GOx Os-polymer, LOx Os-polymer, and EOx Os-polymer. Following a 300 s equilibration period with a baseline buffer solution of 0 mM glucose, lactate, and glutamate, standard solutions with increasing concentrations of each analyte were introduced into the flow cell. Calibration standards were switched every 300 seconds. Calibration curves for glucose (B), lactate (C), and glutamate (D) were extracted from the titration curves. The error bars at each point represent the standard error from at least 3 replicate titrations. E) Magnified image of the SPE chip with three working electrodes (WE), silver-plated reference electrode, and platinum counter electrode. Scale bar represents 5 mm.

From a minimum of three sequential titrations, calibration curves have been created for each analyte (Figure 8.4B-D). As expected, the enzymatic sensors follow traditional enzyme kinetics, as evidenced by the Michaelis-Menten modeling; using this model, dynamic ranges were observed for glucose concentrations up to 25 mM, lactate concentrations up to 3 mM, and glutamate concentrations up to 1 mM. All of these concentration ranges represent biologically relevant thresholds.

When considering the utility of this new sensor platform in tandem with a continuously operational Organ-on-Chip system, the longevity of sensor performance must be taken into consideration. Calibrations were carried out daily to monitor the change in baseline signal (without analyte) and the signal produced from the highest calibration solution, i.e. 25 mM glucose and 3 mM lactate. Figure 8.5 presents the day-to-

day variances for glucose and lactate sensors. When not in use, modified SPEs were stored in 10 mM PBS at 4 °C.

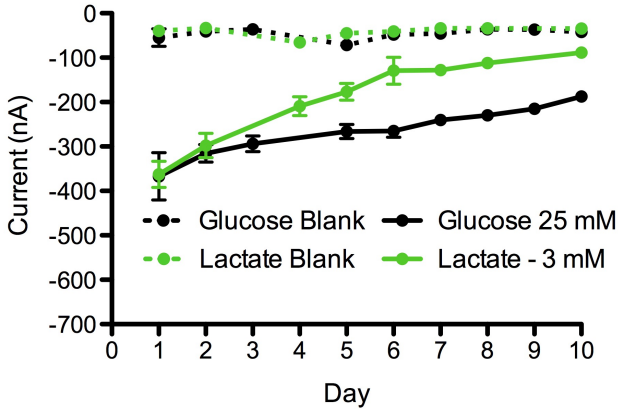

Figure 8.5. Long-term Stability of Os-based Glucose and Lactate Sensors. Glucose (black) and lactate (green) sensors were calibrated once daily over a ten-day period, and the calibration signal maximum (solid) and blank baseline signals (dashed) are presented. Each data point represents the average current and standard deviation of three sensors of that type.

A reasonable amount of stability was observed over the ten-day period for the glucose and lactate sensors. As expected, signal sensitivity is lost over time, and this can be attributed to degradation of the osmium polymer, leeching of the enzyme out of the polymer, or loss of enzyme activity. In the glucose sensor, this performance is observed to be relatively stable; the 10-day sensor generated over 200 nA at 25 mM glucose. As for lactate, the signal decays steadily from the onset of the trial, and continues to Day 10 where only a small (< 100 nA) difference in signal can be observed between blank and 3 mM. These preliminary studies indicate that these sensors maintain appropriate day-to-day reproducibility over short time spans.

Additional studies must be included to accommodate long-term studies of glutamate oxidase-based sensors. Initial studies have shown that sensor performances diminish dramatically within the first 48 hours, thus making them unsuitable for

repetitive use. This will be remedied through the use of more PEGDGE crosslinker to better fix the Os-polymer film or by using an Os-polymer with a higher quantity of unmodified imidazole side chains that may participate in the crosslinking reactions. This increase in free imidazole side chains directly correlates to the reduction of the total quantity of osmium in the hydrogel which ultimately will give rise to slower electron diffusion through the film and subsequently will yield lower analytical sensitivities for the sensor. This compromise between robustness and sensitivity of the sensor will be explored and optimized.

An added benefit to the Os-polymer/enzyme system is a diminished dependence on dissolved oxygen to mediate electron transfer in this system. With redox active osmium complexes tethered to the oxidase enzyme, the electron from the enzyme turnover can be carried to the electrode for signal transduction. This reduced oxygen dependence is explored in Figure 8.6 where an SPE was modified with Os-polymer/GOx on all three working electrode, and tested in normal (air saturated) and oxygen-free standards containing increasing concentrations of glucose. For this experiment set, the small 0.08 mm^2 electrode was left as a bare Pt electrode, and not plated with Ag, such that it could be used to amperometrically measure the concentration of dissolved oxygen in the 26 μL sensor chamber in real time. The platinum auxiliary electrode was plated with a thin layer of silver using methods described above, to create a combined counter/quasi-ref electrode.

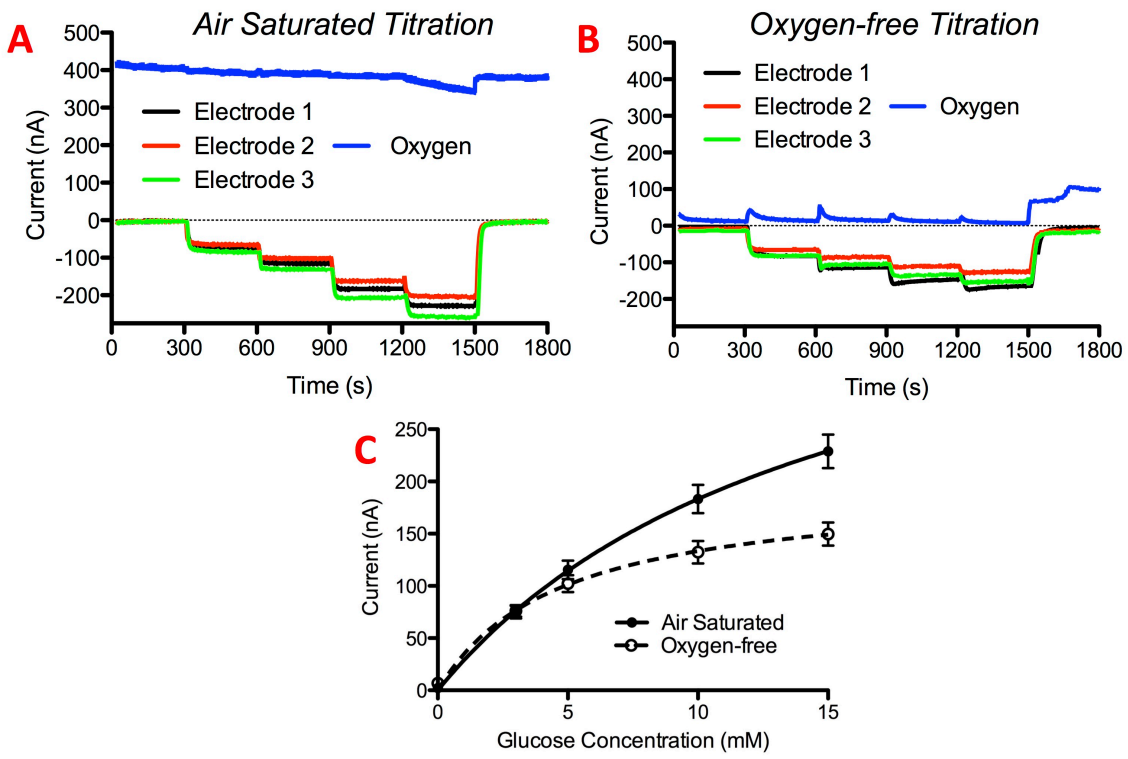

Figure 8.6. Air Saturated and Oxygen-free Glucose Calibrations. Titrations were performed in (A) air saturated buffer solutions containing increasing concentrations of glucose, and then in (B) oxygen-free solutions. Three identical sensors were modified on each SPE denoted as Electrodes 1-3 (black, red, and green). Following a 300 s equilibration period, standards were changed every 300 s in order of ascending glucose concentration from 0 - 15 mM glucose. In both experiments, dissolved oxygen in the flow chamber was tracked using an unmodified 0.08 mm^2 platinum electrode (blue). Calibration curves for the air saturated (solid) and oxygen-free (dashed) titrations are presented in C.

This study was carried out by first performing the titration in normal, air saturated glucose standards (Figure 8.6A). Upon completion of this titration, all standards were purged with N_2 for 30 minutes, and the apparatus was placed inside of a glove bag, which was also flushed with N_2. After removing oxygen from the system, the titration was then performed again (Figure 8.6B). The small, unmodified platinum electrode on the SPE was biased at -0.45 V to detect dissolved oxygen amperometrically during both runs. It can be seen that the purging process was successful at removing dissolved oxygen,

because the oxygen reduction signal decreases significantly between the two titrations, from approximately 400 nA to 10 nA. From the respective titrations, calibration curves were prepared (Figure 8.6C). As expected, the air-saturated signal produced a reasonable anodic current response with increasing concentration of glucose, and the signal begins to saturate at higher concentration as dictated by Michaelis-Menten kinetics. As the oxygen is removed from the system, the Os-polymer becomes the dominant electron carrier between enzyme and electrode. From 0 - 5 mM, the oxygen-free system behaves similarly to the typical air saturated system, as the low concentration regions of both calibration curves are virtually identical. This concentration range is acceptable for a variety of biological and clinical applications, and the oxygen insensitivity of this sensor type makes this ideal for use in ischemic *in vitro* analyses.

Beyond the concentration of 10 mM glucose, the current for the oxygen-free system reaches signal saturation, which is expected with a limited number of osmium complexes fixed in the film. Increasing the amount of osmium complexes in the film would increase this expected saturation current due to the introduction of more electron carriers, and subsequently increase the apparent electron diffusion coefficient. Since the electron diffusion rate is dictated by the self-exchange collision rate between tethered complexes, and increasing the number of osmium complexes in the same film would decrease the average distance between complexes would decrease, then a rate increase in electron transfer is expected.

Conclusions and Future Directions

The redox active polymer, $Os(bpy)_2Cl$-PVI, was synthesized and used to prepare enzymatic sensors for glucose, lactate, and glutamate that could be operated at a reduced

electrode bias to avoid amperometric interference from acetaminophen. A specialized screen printed electrode array was modified with Os-polymer/enzyme composites for independent, simultaneous multianalyte detection in real time. This flow-based electrochemical apparatus was validated by performing titrations from co-solutions of glucose, lactate, and glutamate in phosphate buffer with 10 mM acetaminophen.

The stabilities of these Os-polymer/enzyme sensors were explored, and the glucose and lactate-specific sensor performances degraded slowly over time. These operational time scales represent reasonable sensor lifetimes for biological applications; however, further robustness is desired for permanent use in continuously operational Organ-on-Chip systems.

Finally, the oxygen insensitivity for these sensors was demonstrated by performing air saturated and oxygen-free glucose titrations for Os-polymer/GOx sensors. Over biologically relevant concentrations (0 – 5 mM) these sensors responded comparably, and further inclusion of additional osmium complexes in the hydrogel network would likely improve the dynamic range of the oxygen-free titrations.

For the first time, these redox polymers have been utilized for a multianalyte platform. These sensors have proved to be selective and sensitive for glucose, lactate, and glutamate without interference from acetaminophen, thus making them ideal for use in *in vitro* hepatocellular systems. The oxygen insensitivity provides additional versatility for observing the effects of ischemia in oxygen deprived *in vitro* systems.

Chapter 9

CONCLUSIONS AND OUTLOOK

Summary

In this dissertation, we have addressed the enzyme electrode interface with respect to improving electron transfer across this gap, with special regard to the photoactive protein, Photosystem I (PSI). Previous studies of PSI had demonstrated a fundamental viability of PSI immobilized on metallic and semiconductor electrodes. However, these PSI electrodes were limited in photovoltaic efficiency based on poor electron transfer at the protein/electrode interface. The various studies presented here seek to develop the next generation of PSI composite materials that are capable of appreciable photoefficiencies.

In Chapter 3, a novel class of conductive polymer-protein hybrids were constructed by *in situ* electrochemical polymerization of a co-solution of aniline and PSI. These films, grown directly off gold electrodes, served as an immobilization matrix for the protein, and also as a conductive material to aid in electron transport from PSI to the underlying gold. These proof-of-concept composites yielded a modest 5.7 $\mu A\ cm^{-2}$, but the material represented the first of its kind with its ability to rapidly entrap high molecular weight photoactive proteins.

These novel composite films were later used as the photosensitizing layer of solid-state photovoltaic devices as described in Chapter 4. Utilizing the previously optimized methods for *in situ* polymerization and film growth, these composites were

fabricated on TiO_2 substrates. This semiconducting material represents an energetically favorable substrate that can efficiently accept electrons from the PAni-PSI film based on the position of its conduction band. Simple photovoltaic devices were fabricated from PAni-PSI/TiO_2 by evaporating a thin silver layer on the backside of the PAni-PSI layer. When tested under standard solar simulation conditions, these simple devices produced a quantum efficiency of 0.009%, which currently represents the highest reported efficiency for any solid-state PSI-based photovoltaic device.

Additionally, the orientation of PSI at electrode interfaces plays a large role in photovoltaic output. PSI operates *in vivo* by unidirectionally shuttling electrons across the thylakoid membrane from lumen to stroma. Hence, when the protein is removed from the lipid bilayer, orientational control is lost, and there is no alignment for PSI's charge transport vectors. Chapter 5 introduces a new fundamental strategy in which PSI can be functionalized during the extraction process, giving rise to chemical modification restricted to one side of the protein. This side-selective modification strategy allows for the directed surfaces coupling of PSI in the "inverted" orientation with the F_B cluster nearest the electrode surface. Ideally, the uniformity of a PSI film with all electron transport vector aligned will maximize photocurrent in PSI-derived photoactive layers by minimizing competing electrochemical reactions and charge recombination events.

PSI-based photovoltaic devices were further studied in Chapter 6, which focuses on electron transport layers that can rapidly be assembled on p-Si/PSI electrodes. Previously, ZnO was deposited on the PSI active layer using Confined Plume Chemical Deposition. This technique established a thin film of ZnO on the PSI, which is an ideal electron accepting material for a solid-state cell. To further advance this device type, an

organic material that could be synthesized and deposited in a more facile manner was desired. The metal-free redox polymer, poly(p-xylylviologen), was synthesized and cast into film ontop of PSI on p-Si. ITO was pressed onto the polyviologen layer to construct a very simple photovoltaic device. These polymers represent a unique avenue for future development and optimization of scalable PSI solar cells.

In regards to streamlining the PSI device development process, a new protocol for the extraction of the protein from green plants was introduced in Chapter 7. This process was successful in redesigning the protocol procedure to require less intensive user ability and call for only easily accessible/inexpensive chemicals and equipment.

Finally, the goal of improving electron transfer across the protein/electrode interface was brought to a new application: biosensors. Enzymatic biosensors, such a glucose biosensors, are commonly found in a variety of biomedical applications. However, these sensor types are fundamentally restricted based on their dependence for dissolved oxygen to mediate electron transfer from enzyme to electrode for signal transduction. In Chapter 8, osmium-containing redox polymers are used as a immobilization matrix for oxidase enzymes on screen printed electrodes.

The screen printed electrode array was designed for the simultaneous amperometric measurement of three analytes, and for this study the electrodes were modified with Os-polymer and either glucose, lactate, or glutamate oxidase. The osmium complexes within the hydrogel act as electron hopping sites to mediate transfer from enzyme to electrode, and also require a lower electrode bias to turnover the substrate. This lower bias (0.2 V) avoids amperometric interference from electroactive species commonly found in *in vitro* liver systems. To this extent, the newly developed

multianalyte biosensor was calibrated to a range of concentrations for glucose, lactate, and glutamate over a background of 10 mM acetaminophen.

Perspectives and Outlook

Nature has provided researchers with a model for efficient solar energy conversion. PSI currently stands not only as a model for inspiration, but rather is a complete entity that can be harvested and integrated directly into emerging alternative energy technologies. Previously the research teams at Vanderbilt, along with other groups around the globe, have made great strides in studying the protein, incorporating into rudimentary films, and even integrating the protein in prototype solar cells. The PSI-based solar cells produced thus far still fall short of commercial viability. There is a significant journey ahead before PSI photovoltaics can reach practicality with photocurrent densities greater than 10 mA cm^{-2} and efficiencies higher than 1%.

Returning again to the model of natural photosynthesis, it is worth noting that although PSI operates individually with high internal quantum efficiency, the overall process of photosynthesis occurs through a series of functional proteins that act in series to carry out a much larger biological function. It then becomes apparent that PSI, with its highly specialized *in vivo* function, is not idealized to operate alone. When designing PSI-based solar energy conversion systems for the future, the integration of the natural protein with complementary components and materials seems imminent. The future of the field is dependent on the design and fabrication of composite materials and conjugates with PSI.

For instance, PSI is naturally found in thylakoid membrane electronically downhill from PSII. A series of small molecules and proteins mediate photoactivated

electron transfer from PSII to PSI. When used together, a PSII/PSI hybrid system could provide a very large potential energy gap between the hole generated by $P680^+$ (of PSII) and F_B^- (of PSI) of approximately 1.8 V. Future biohybrid technologies that seek to exploit these natural series photodiodes could utilize the protein functionalization and orientation strategies introduced in Chapter 6 to "wire" PSII and PSI complexes together in a head-to-tail fashion on a surface for bioderived water splitting electrodes.

PSI's chlorophyll network is highly adapted to absorb red light with a local maximum near 680 nm. However, this means that the protein is insensitive to many wavelengths in the green-region of the solar spectrum. These non-absorbed photons will count against any overall device efficiency, and to maximize any device output, PSI could be coupled to another photosensitizing component.

Quantum dots (QDs) are an interesting material that could be used in a tandem device with PSI. These very small particles can be easily synthesized, and feature unique size-dependent optoelectronic properties. As a model example, CdSe particles can be size-tuned to have optical band gaps ranging from 2.1-2.3 eV, making the particles green absorbing. When coupled with appropriate electron donors and acceptors, QDs can initiate charge separation with relatively high efficiency. Interfacing PSI with carefully selected QDs may introduce a new type of tandem biohybrid device capable of absorbing a broader range of solar wavelengths.

Finally, graphene is one of the most fascinating electronic materials for interfacing with PSI. Two hallmark studies involving PSI on graphene-based materials have already demonstrated the effective electronic interaction between the two organic components.[114,115] PSI devices utilizing graphene are very desirable because of the

prospect of preparing an organic, metal-free photovoltaic device. Future goals for PSI with graphene involve layering the protein within doped graphene stacks on substrates. This way, the PSI can be organized and oriented into multilayer films with charge collecting layers of p- or n-type graphene sandwiching the PSI film.

Photosystem I is a natural protein supercomplex that is vital to photosynthesis. This protein is a key component that powers nearly all life on earth. However, its robustness has also proven it to be useful in biohybrid solar-to-electricity conversion. Nature has provided a fantastic model for solar energy conversion for billions of years, and also has provided the natural components for harvest and construction of semi-artificial, low-cost solar cells.

REFERENCES

(1) DOE Pursues SunShot Initiative to Achieve Cost Competitive Solar Energy by 2020 http://energy.gov/eere/sunshot/articles/doe-pursues-sunshot-initiative-achieve-cost-competitive-solar-energy-2020 (accessed Jan 1, 2016).

(2) Arnon, D. I. Quantum Efficiency of Photosynthetic Energy Conversion. *Proc. Natl. Acad. Sci.* **1977**, *74* (8), 3377–3381.

(3) Badura, A.; Kothe, T.; Schuhmann, W.; Rogner, M. Wiring Photosynthetic Enzymes to Electrodes. *Energy Environ. Sci.* **2011**, *4*, 3263–3274.

(4) Boghossian, A. A.; Ham, M. H.; Choi, J. H.; Strano, M. S. Biomimetic Strategies for Solar Energy Conversion: A Technical Perspective. *Energy Environ. Sci.* **2011**, *4*, 3834–3843.

(5) LeBlanc, G.; Gizzie, E. A.; Yang, S.; Cliffel, D. E.; Jennings, G. K. Photosystem I Protein Films at Electrode Surfaces for Solar Energy Conversion. *Langmuir* **2014**, *30*, 10990–11001.

(6) Ko, B. S.; Babcock, B.; Jennings, G. K.; Tilden, S. G.; Peterson, R. R.; Cliffel, D.; Greenbaum, E. Effect of Surface Composition on the Adsorption of Photosystem I onto Alkanethiolate Self-Assembled Monolayers on Gold. *Langmuir* **2004**, *20* (10), 4033–4038.

(7) Kincaid, H. A.; Niedringhaus, T.; Ciobanu, M.; Cliffel, D. E.; Jennings, G. K. Entrapment of Photosystem I within Self-Assembled Films. *Langmuir* **2006**, *22* (19), 8114–8120.

(8) Ciobanu, M.; Kincaid, H. A.; Lo, V.; Dukes, A. D.; Jennings, G. K.; Cliffel, D. E.

Electrochemistry and Photoelectrochemistry of Photosystem I Adsorbed on Hydroxyl-Terminated Monolayers. *J. Electroanal. Chem.* **2007**, *599* (1), 72–78.

(9) Carmeli, I.; Frolov, L.; Carmeli, C.; Richter, S. Photovoltaic Activity of Photosystem I Based Self-Assembled Monolayer. *J. Am. Chem. Soc.* **2007**, *129*, 12352–12353.

(10) Lee, I.; Lee, J. W.; Stubna, A.; Greenbaum, E. Measurement of Electrostatic Potentials above Oriented Single Photosynthetic Reaction Centers. *J. Phys. Chem. B* **2000**, *104*, 2439–2443.

(11) Ihara, M.; Nishihara, H.; Yoon, K.-S.; Lenz, O.; Friedrich, B.; Nakamoto, H.; Kojima, K.; Honma, D.; Kamachi, T.; Okura, L. Light-Driven Hydrogen Production by a Hybrid Complex of a [NiFe]-Hydrogenase and the Cyanobacterial Photosystem I. *Photochem. Photobiol.* **2006**, *82*.

(12) McTavish, H. Hydrogen Evolution by Direct Electron Transfer from Photosystem I toHydrogenases. *J. Biochem.* **1998**, *123*.

(13) Utschig, L. M.; Dimitrijevic, N. M.; Poluektov, O. G.; Chemerisov, S. D.; Mulfort, K. L.; Tiede, D. M. Photocatalytic Hydrogen Production from Noncovalent Biohybrid Photosystem I/Pt Nanoparticle Complexes. *J. Phys. Chem. Lett.* **2011**, *2* (3), 236–241.

(14) Gust, D.; Moore, T. A.; Moore, A. L. Solar Fuels via Artificial Photosynthesis. *Acc. Chem. Res.* **2009**, *42* (12), 1890–1898.

(15) Leblanc, G.; Chen, G.; Jennings, G. K.; Cliffel, D. E. Photoreduction of Catalytic Platinum Particles Using Immobilized Multilayers of Photosystem I. *Langmuir* **2012**, *28* (21), 7952–7956.

(16) Lubner, C. E.; Applegate, A. M.; Knörzer, P.; Ganago, A.; Bryant, D. A.; Happe, T.; Golbeck, J. H. Solar Hydrogen-Producing Bionanodevice Outperforms Natural Photosynthesis. *PNAS* **2011**, *108* (52).

(17) Ciesielski, P. N.; Hijazi, F. M.; Scott, A. M.; Faulkner, C. J.; Beard, L.; Emmett, K.; Rosenthal, S. J.; Cliffel, D.; Jennings, G. K. Photosystem I - Based Biohybrid Photoelectrochemical Cells. *Bioresour. Technol.* **2010**, *101* (9), 3047–3053.

(18) Ciesielski, P. N.; Faulkner, C. J.; Irwin, M. T.; Gregory, J. M.; Tolk, N. H.; Cliffel, D. E.; Jennings, G. K. Enhanced Photocurrent Production by Photosystem I Multilayer Assemblies. *Adv. Funct. Mater.* **2010**, *20* (23), 4048–4054.

(19) LeBlanc, G.; Chen, G.; Gizzie, E. A.; Jennings, G. K.; Cliffel, D. E. Enhanced Photocurrents of Photosystem I Films on P-Doped Silicon. *Adv. Mater.* **2012**, *24*, 5959–5962.

(20) Mershin, A.; Matsumoto, K.; Kaiser, L.; Yu, D.; Vaughn, M.; Nazeeruddin, M. K.; Bruce, B. D.; Graetzel, M.; Zhang, S. Self-Assembled Photosystem-I Biophotovoltaics on Nanostructured TiO2 and ZnO. *Sci. Rep.* **2012**, *2*.

(21) Reeves, S. G.; Hall, D. O. Higher Plant Chloroplasts and Grana: General Preparative Procedures (Excluding High Carbon Dioxide Fixation Ability Chloroplasts). *Methods Enzymol.* **1980**, *69*, 85–94.

(22) Shiozawa, J. A.; Alberte, R. S.; Thornber, J. P. The P700-Chlorophyll a-Protein, Isolation and Some Characteristics of the Complex in Higher Plants. *Arch. Biochem. Biophys.* **1974**, *165*, 388–397.

(23) Baba, K.; Itoh, S.; Hastings, G.; Hoshina, S. Photoinhibition of Photosystem I Electron Transfer Activity in Isolated Photosystem I Preparations with Different

Chlorophyll Contents. *Photosynth. Res.* **1996**, *47* (2), 121–130.

(24) Brettel, K.; Leibl, W. Electron Transfer in Photosystem I. *Biochim. Biophys. Acta* **2001**, *1507*, 100–114.

(25) Amunts, A.; Drory, O.; Nelson, N. The Structure of a Plant Photosystem I Supercomplex at 3.4 Angstrom Resolution. *Nature* **2007**, *447* (7140), 58–63.

(26) Barber, J. Structure of Photosystem I. *Nat. Struct. Mol. Biol.* **2001**, *8*, 577–579.

(27) Yehezkeli, O.; Tel-Vered, R.; Michaeli, D.; Willner, I.; Nechushtai, R. Photosynthetic Reaction Center-Functionalized Electrodes for Photo-Bioelectrochemical Cells. *Photosynth Res* **2013**.

(28) Ciobanu, M.; Kincaid, H. A.; Jennings, G. K.; Cliffel, D. E. Photosystem I Patterning Imaged by Scanning Electrochemical Microscopy. *Langmuir* **2004**, *21* (2), 692–698.

(29) Das, R.; Kiley, P. J.; Segal, M.; Norville, J.; Yu, A. A.; Wang, L. Y.; Trammell, S. A.; Reddick, L. E.; Kumar, R.; Stellacci, F.; et al. Integration of Photosynthetic Protein Molecular Complexes in Solid-State Electronic Devices. *Nano Lett.* **2004**, *4* (6), 1079–1083.

(30) Ciesielski, P. N.; Cliffel, D. E.; Jennings, G. K. Kinetic Model of the Photocatalytic Effect of a Photosystem I Monolayer on a Planar Electrode Surface. *J Phys Chem A* **2011**, *115* (15), 3326–3334.

(31) Maly, J.; Masojidek, J.; Masci, A.; Cianci, E.; Foglietti, V.; Vastarella, W.; Pilloton, R. Direct Mediatorless Electron Transport between the Monolayer of Photosystem II and Poly(mercapto-P-Benzoquinone) Modified Gold Electrode—new Design of Biosensor for Herbicide Detection. *Biosens. Bioelectron.* **2005**, *21*,

923–932.

(32) Yehezkeli, O.; Tel-Vered, R.; Wasserman, J.; Trifonov, A.; Michaeli, D. Integrated Photosystem II-Based Photo-Bioelectrochemical Cells. *Nat. Commun.* **2012**, *3* (742).

(33) Badura, A.; Guschin, D.; Kothe, T.; Kopczak, M. J.; Schuhmann, W.; Rogner, M. Photocurrent Generation by Photosystem 1 Integrated in Crosslinked Redox Hydrogels. *Energy Environ. Sci.* **2011**, *4* (7), 2435–2440.

(34) Badura, A.; Guschin, D.; Esper, B.; Kothe, T.; Neugebauer, S.; Schuhmann, W.; Rogner, M. Photo-Induced Electron Transfer Between Photosystem 2 via Cross-Linked Redox Hydrogels. *Electroanalysis* **2008**, *20* (10).

(35) Heller, A. Redox Hydrogel-Based Electrochemical Biosensors. *Biosensors*. 2nd ed. Oxford University Press: USA 2004.

(36) Gordiichuk, P. I.; Wetzelaer, G. A. H.; Rimmerman, D.; Gruszka, A.; De Vries, J. W.; Saller, M.; Gautier, D. a.; Catarci, S.; Pesce, D.; Richter, S.; et al. Solid-State Biophotovoltaic Cells Containing Photosystem I. *Adv. Mater.* **2014**, *26* (28), 4863–4869.

(37) Baker, D. R.; Simmerman, R. F.; Sumner, J. J.; Bruce, B. D.; Lundgren, C. A. Photoelectrochemistry of Photosystem I Bound in Nafion. *Langmuir* **2014**, *30*, 13650–13655.

(38) Vidal, J.-C.; Garcia-Ruiz, E.; Castillo, J.-R. Recent Advances in Electropolymerized Conducting Polymers in Amperometric Biosensors. *Microchim. Acta.* **2003**, *143*, 93–111.

(39) Foulds, N. C.; Lowe, C. R. Enzyme Entrapment in Electrically Conducting

Polymers. *J . Chem. Soc., Faraday Trans.* **1986**, *1*, 1259–1264.

(40) Poet, P. D. T. Du. Direct Electron Transfer with Glucose Oxidase in an Electropolymerized poly(N-Methylpyrrole) Film on a Gold Microelectrode. *Anal. Chim. Acta* **1990**, *235*, 255–263.

(41) Bejbouji, H.; Vignau, L.; Miane, J. L.; Dang, M.-T.; Oualim, E. M.; Harmouchi, M.; Mouhsen, A. Polyaniline as a Hole Injection Layer on Organic Photovoltaic Cells. *Sol. Energy Mater. Sol. Cells* **2010**, *94*, 176–181.

(42) Molapo, K. M.; Ndangili, P. M.; Ajayi, R. F.; Mbambisa, G.; Mailu, S. M.; Njomo, N.; Masikini, M.; Baker, P.; Iwuoha, E. I. Electronics of Conjugated Polymers (I): Polyaniline. *Int. J. Electrochem. Sci.* **2012**, *7*, 11859–11875.

(43) Lee, J. W.; Lee, I.; Laible, P. D.; Owens, T. G.; Greenbaum, E. Chemical Platinization and Its Effect on Excitation Transfer Dynamics and P700 Photooxidation Kinetics in Isolated Photosystem I. *Biophys. J.* **1995**, *69*, 652–659.

(44) Fotiadis, D.; Muller, D. J.; Tsiotis, G.; Hasler, L.; Tittmann, P.; Mini, T.; Jeno, P.; Gross, H.; Engel, A. Surface Analysis of the Photosystem I Complex by Electron and Atomic Force Microscopy. *J. Mol. Biol.* **1998**, *283*, 83–94.

(45) Boekema, E. J.; Wynn, R. M.; Malkin, R. The Structure of Spinach Photosystem I Studied by Electron Microscopy. *Biochim. Biophys. Acta* **1990**, *1017*, 49–56.

(46) Cota, A.; Lakarda, S.; Dejeub, J.; Rougeotb, P.; C. Magneneta; Lakarda, B.; Gauthier, M. Electrosynthesis and Characterization of Polymer Films on Silicon Substrates for Applications in Micromanipulation. *Synth. Met.* **2012**, *162*, 2370–2378.

(47) Plesu, N.; Kellenberger, A.; Mihali, M. Effect of Temperature on the

Electrochemical Synthesis and Properties of Polyaniline Films. *J. Non. Cryst. Solids* **2010**, *356*, 1081–1088.

(48) Manocchi, A. K.; Baker, D. R.; Pendley, S. S.; Nguyen, K.; Hurley, M. M.; Bruce, B. D.; Sumner, J. J.; Lundgren, C. A. Photocurrent Generation from Surface Assembled Photosystem I on Alkanethiol Modified Electrodes. *Langmuir* **2013**, *29*, 2412–2419.

(49) Hogewoning, S. W.; Wientjes, E.; Douwstra, P.; Trouwborst, G.; van Ieperen, W.; Croce, R.; Harbinson, J. Photosynthetic Quantum Yield Dynamics: From Photosystems to Leaves. *Plant Cell* **2012**, *24* (5), 1921–1935.

(50) Kargul, J.; Janna Olmos, J. D.; Krupnik, T. Structure and Function of Photosystem I and Its Application in Biomimetic Solar-to-Fuel Systems. *J. Plant Physiol.* **2012**, *169* (16), 1639–1653.

(51) Nagy, L.; Magyar, M.; Szabó, T.; Hajdu, K.; Giotta, L.; Dorogi, M.; Milano, F. Photosynthetic Machineries in Nano-Systems. *Curr. Protein Pept. Sci.* **2014**, *15* (4), 363.

(52) Agostiano, A.; Ceglie, A.; Monica, M. Della; Studi, C.; Amendola, V. Current-Potential Curves of Photosystems Adsorbed on Platinized Platinum Electrodes. *Bioelectrochemistry Bioenerg.* **1983**, *10*, 377–384.

(53) Katz, E. Y.; Shkuropatov, A. Y.; Vagabova, O. I.; Shuvalov, V. A. Coupling of Photoinduced Charge Separation in Reaction Centers of Photosynthetic Bacteria with Electron Transfer to a Chemically Modified Electrode. *Biochim. Biophys. Acta - Bioenerg.* **1989**, *976*, 121–128.

(54) Katz, E. Application of Bifunctional Reagents for Immobilization of Proteins on a

Carbon Electrode Surface: Oriented Immobilization of Photosynthetic Reaction Centers. *J. Electroanal. Chem.* **1994**, *365*, 157–164.

(55) Greenbaum, E. Platinized Chloroplasts: A Novel Photocatalytic Material. *Science (80-.).* **1985**, *230* (4732), 1373–1375.

(56) Brettel, K. Electron Transfer and Arrangement of the Redox Cofactors in Photosystem I. *Biochim. Biophys. Acta* **1997**, *1318*, 322–373.

(57) Mukherjee, D.; May, M.; Vaughn, M.; Bruce, B. D.; Khomami, B. Controlling the Morphology of Photosystem I Assembly on Thiol-Activated Au Substrates. *Langmuir* **2010**, *26* (20), 16048–16054.

(58) Ocakoglu, K.; Krupnik, T.; van den Bosch, B.; Harputlu, E.; Gullo, M. P.; Olmos, J. D. J.; Yildirimcan, S.; Gupta, R. K.; Yakuphanoglu, F.; Barbieri, A.; et al. Photosystem I-Based Biophotovoltaics on Nanostructured Hematite. *Adv. Funct. Mater.* **2014**, *24* (47), 7467–7477.

(59) Shah, V. B.; Henson, W. R.; Chadha, T. S.; Lakin, G.; Liu, H.; Blankenship, R. E.; Biswas, P. Linker-Free Deposition and Adhesion of Photosystem I onto Nanostructured TiO2 for Biohybrid Photoelectrochemical Cells. *Langmuir* **2015**, *31* (5), 1675–1682.

(60) Yu, D.; Wang, M.; Zhu, G.; Ge, B.; Liu, S.; Huang, F. Enhanced Photocurrent Production by Bio-Dyes of Photosynthetic Macromolecules on Designed TiO2 Film. *Sci. Rep.* **2015**, *5*, 9375.

(61) Gizzie, E. A.; LeBlanc, G.; Jennings, G. K.; Cliffel, D. E. Electrochemical Preparation of Photosystem I - Polyaniline Films Composite Films for Biohybrid Solar Energy Conversion. *ACS Appl. Mater. Interfaces* **2015**, *7* (18), 9328–9335.

(62) Grätzel, M. Photoelectrochemical Cells. *Nature* **2001**, *414* (6861), 338–344.

(63) Baćani, M.; Novak, M.; Kokanović, I.; Babić, D. Hopping Electron Transport in Doped Polyaniline: An Experimental Verification of the Fogler-Teber-Shklovskii Model. *Synth. Met.* **2013**, *172*, 28–31.

(64) Pattantyus-Abraham, A. G.; Kramer, I. J.; Barkhouse, A. R.; Wang, X.; Konstantatos, G.; Debnath, R.; Levina, L.; Raabe, I.; Nazeeruddin, M. K.; Grätzel, M.; et al. Depleted-Heterojunction Colloidal Quantum Dot Solar Cells. *ACS Nano* **2010**, *4* (6), 3374–3380.

(65) Xu, T.; Qiao, Q. Conjugated Polymer-Inorganic Semiconductor Hybrid Solar Cells. *Energy Environ. Sci.* **2011**, *4*, 2700–2720.

(66) Gunther, D.; LeBlanc, G.; Cliffel, D. E.; Jennings, G. K. Pueraria Lobata (Kudzu) Photosystem I Improves the Photoelectrochemical Performance of Silicon. *Ind. Biotechnol.* **2013**, *9* (1), 37–41.

(67) Ciesielski, P. N.; Cliffel, D. E.; Jennings, G. K. Kinetic Model of the Photocatalytic Effect of a Photosystem I Monolayer on a Planar Electrode Surface. *J. Phys. Chem. A* **2011**, *115* (15), 3326–3334.

(68) Frolov, L.; Rosenwaks, Y.; Richter, S.; Carmeli, C.; Carmeli, I. Photoelectric Junctions Between GaAs and Photosynthetic Reaction Center Protein. *J. Phys. Chem. C* **2008**, *112*, 13426–13430.

(69) Sepunaru, L.; Tsimberov, I.; Forolov, L.; Carmeli, C.; Carmeli, I.; Rosenwaks, Y. Picosecond Electron Transfer from Photosynthetic Reaction Center Protein to GaAs. *Nano Lett.* **2009**, *9* (7), 2751–2755.

(70) Kondo, M.; Iida, K.; Dewa, T.; Tanaka, H.; Ogawa, T.; Nagashima, S.;

Nagashima, K. V. P.; Shimada, K.; Hashimoto, H.; Gardiner, A. T.; et al. Photocurrent and Electronic Activities of Oriented-His-Tagged Photosynthetic Light-Harvesting/reaction Center Core Complexes Assembled onto a Gold Electrode. *Biomacromolecules* **2012**, *13* (2), 432–438.

(71) Yan, X.; Faulkner, C. J.; Jennings, G. K.; Cliffel, D. E. Photosystem I in Langmuir−Blodgett and Langmuir−SchaeferMonolayers. *Langmuir* **2012**, *28*, 15080–15086.

(72) Yasuda, Y.; Sugino, H.; Toyotama, H.; Hirata, Y.; Hara, M.; Miyake, J. Control of Protein Orientation in Molecular Photoelectric Devices Using Langmuir-Blodgett Films of Photosynthetic Reaction Centers from Rhodopseudomonas Viridis. *Bioelectrochemistry Bioenerg.* **1994**, *34* (2), 135–139.

(73) Hermanson, G. T. *Bioconjugate Techniques*, 3rd ed.; Audet, J., Preap, M., Eds.; Elsevier, 2013.

(74) Bard, A. J.; Faulkner, L. R. *Electrochemical Methods: Fundamentals and Applications*, 2nd ed.; John Wiley & Sons, 2001.

(75) Traut, R. R.; Bollen, A.; Sun, T.-T.; Hershey, J. W. B.; Sundberg, J.; Pierce, L. R. Methyl 4-Mercaptobutyrimidate as a Cleavable Cross-Linking Reagent and Its Application to the Escherichia Coli 30S Ribosome. *Biochemistry* **1973**, *12* (17), 3266–3273.

(76) Riddles, P. W.; Blakeley, R. L.; Zerner, B. Ellman's Reagent: 5,5'-Dithiobis(2-Nitrobenzoic Acid) - a Reexamination. *Anal. Biochem.* **1979**, *94*, 75–81.

(77) Matsumoto, K.; Vaughn, M.; Bruce, B. D.; Koutsopoulos, S.; Zhang, S. Designer Peptide Surfactants Stabilize Functional Photosystem-I Membrane Complex in

Aqueous Solution for Extended Time. *J. Phys. Chem. B* **2008**, *113* (1), 75–83.

(78) Munge, B.; Das, S. K.; Ilagan, R.; Pendon, Z.; Yang, J.; Frank, H. A.; Rusling, J. F. Electron Transfer Reactions of Redox Cofactors in Spinach Photosystem I Reaction Center Protein in Lipid Films on Electrodes. *J. Am. Chem. Soc.* **2003**, *125*, 12457–12463.

(79) Kaftan, D.; Brumfeld, V.; Nevo, R.; Scherz, A.; Reich, Z. From Chloroplasts to Photosystems: In Situ Scanning Force Microscopy on Intact Thylakoid Membranes. *EMBO J.* **2002**, *21* (22), 6146–6153.

(80) Gizzie, E. A.; Niezgoda, J. S.; Robinson, M. T.; Harris, A. G.; Jennings, G. K.; Rosenthal, S. J.; Cliffel, D. E. Photosystem I-polyaniline/TiO2 Solid-State Solar Cells: Simple Devices for Biohybrid Solar Energy Conversion. *Energy Environ. Sci.* **2015**, *8* (12), 3572–3576.

(81) Beam, J. C.; LeBlanc, G.; Gizzie, E. A.; Ivanov, B. L.; Needell, D. R.; Shearer, M. J.; Jennings, G. K.; Cliffel, D. E.; Lukehart, C. M. Construction of a Semiconductor-Biological Interface for Solar Energy Conversion: P-Doped Silicon/Photosystem I/ZnO. *Langmuir* **2015**, *31*, 10002–10007.

(82) Factor, A.; Heinsohn, G. E. Polyviologens - a Novel Class of Cationic Polyelectrolyte Redox Polymers. *J. Polym. Sci. Polym. Lett. Ed.* **1971**, *9*, 289–295.

(83) Sassoon, R. E.; Gershuni, S.; Rabani, J. Charge Separation in Photolnitlated Electron-Transfer Systems with Polyviologen Polyelectrolytes as Quenchers. *J. Phys. Chem.* **1985**, *89*, 1937–1945.

(84) Tagliazucchi, M.; Amin, V. A.; Schneebeli, S. T.; Stoddart, J. F.; Weiss, E. A. High-Contrast Photopatterning of Photoluminescence within Quantum Dot Films

through Degradation of a Charge-Transfer Quencher. *Adv. Mater.* **2012**, *24*, 3617–3621.

(85) Tagliazucchi, M.; Tice, D. B.; Sweeney, C. M.; Morris-Cohen, A. J.; Weiss, E. A. Ligand-Controlled Rates of Photoinduced Electron Transfer in Hybrid CdSe. *ACS Nano* **2011**, *5* (12), 9907–9917.

(86) Yehezkeli, O.; Tel-Vered, R.; Michaeli, D.; Nechushtai, R.; Willner, I. Photosystem I (PSI)/Photosystem II (PSII)-Based Photo-Bioelectrochemical Cells Revealing Directional Generation of Photocurrents. *Small* **2013**, *9* (17), 2970–2978.

(87) Jo, M. Y.; Ha, Y. E.; Kim, J. H. Polyviologen Derivatives as an Interfacial Layer in Polymer Solar Cells. *Sol. Energy Mater. Sol. Cells* **2012**, *107*, 1–8.

(88) Jo, M. Y.; Ha, Y. E.; Kim, J. H. Interfacial Layer Material Derived from Dialkylviologen and Sol–gel Chemistry for Polymer Solar Cells. *Org. Electron.* **2013**, *14* (3), 995–1001.

(89) Do, T. T.; Hong, H. S.; Ha, Y. E.; Park, C.; Kim, J. H. Investigation of the Property Change of Polymer Solar Cells by Changing Counter Anions in Polyviologen as a Cathode Buffer Layer. *Macromol. Res.* **2015**, *23* (2), 177–182.

(90) Ciesielski, P. N. Photosystem I–Based Systems for Photoelectrochemical Energy Conversion, 2010.

(91) Ciesielski, P. N.; Scott, A. M.; Faulkner, C. J.; Berron, B. J.; Cliffel, D. E.; Jennings, G. K. Functionalized Nanoporous Gold Leaf Electrode Films for the Immobilization of Photosystem I. *ACS Nano* **2008**, *2* (12), 2465–2472.

(92) Schuster, D.; Laggner, C.; Langer, T. Why Drugs Fail - A Study on Side Effects in

New Chemical Entities. *Curr. Pharm. Des.* **2005**, *11* (27), 3545–3559.

(93) Bale, S. S.; Vernetti, L.; Senutovitch, N.; Jindal, R.; Hegde, M.; Gough, A.; McCarty, W. J.; Bakan, A.; Bhushan, A.; Shun, T. Y.; et al. In Vitro Platforms for Evaluating Liver Toxicity. *Exp. Biol. Med.* **2014**, *239*, 1180–1191.

(94) Meyer, D. F.; Gamache, P. H.; Acworth, I. N. The Application of Electrochemistry to Metabolic Profiling. In *Metabolome Analyses: Strategies for Systems Biology*; Vaidyanathan, S., Harrigan, G. G., Goodacre, R., Eds.; Springer US, 2005; pp 119–135.

(95) Chen, C.; Xie, Q.; Yang, D.; Xiao, H.; Fu, Y.; Tan, Y.; Yao, S. Recent Advances in Electrochemical Glucose Biosensors: A Review. *RSC Adv.* **2013**, *3*, 4473–4491.

(96) Kimmel, D. W.; LeBlanc, G.; Meschievitz, M. E.; Cliffel, D. E. Electrochemical Sensors and Biosensors. *Anal. Chem.* **2012**, *84* (2), 685–707.

(97) Snider, R. M.; Ciobanu, M.; Rue, A. E.; Cliffel, D. E. A Multiwalled Carbon Nanotube/dihydropyran Composite Film Electrode for Insulin Detection in a Microphysiometer Chamber. *Anal. Chim. Acta* **2008**, *609* (1), 44–52.

(98) Hiatt, L. A.; McKenzie, J. R.; Deravi, L. F.; Harry, R. S.; Wright, D. W.; Cliffel, D. E. A Printed Superoxide Dismutase Coated Electrode for the Study of Macrophage Oxidative Burst. *Biosens. Bioelectron.* **2012**, *33* (1), 128–133.

(99) Zeiger, S. L. H.; McKenzie, J. R.; Stankowski, J. N.; Martin, J. a.; Cliffel, D. E.; McLaughlin, B. Neuron Specific Metabolic Adaptations Following Multi-Day Exposures to Oxygen Glucose Deprivation. *Biochim. Biophys. Acta - Mol. Basis Dis.* **2010**, *1802* (11), 1095–1104.

(100) Snider, R. M.; McKenzie, J. R.; Kraft, L.; Kozlov, E.; Wikswo, J. P.; Cliffel, D. E.

The Effects of Cholera Toxin on Cellular Energy Metabolism. *Toxins (Basel).* **2010**, *2* (4), 632–648.

(101) Eisenstein, M. Honey, I Shrunk the Lungs. *Nature* **2015**, *519*, S16–S18.

(102) Marx, V. Organs from the Lab. *Nature* **2015**, *522*, 373–377.

(103) Kalgutkar, A. S.; Soglia, J. R. Minimising the Potential for Metabolic Activation in Drug Discovery. *Expert Opin. Drug Metab. Toxicol.* **2005**, *1* (1), 91–142.

(104) Wang, J. Electrochemical Glucose Biosensors. *Chem. Rev.* **2008**, *108*, 814–825.

(105) Bharathi, S.; Nogami, M. A Glucose Biosensor Based on Electrodeposited Biocomposites of Gold Nanoparticles and Glucose Oxidase Enzyme. *Analyst* **2001**, *126* (11), 1919–1922.

(106) Dodevska, T.; Horozova, E.; Dimcheva, N. Electrocatalytic Reduction of Hydrogen Peroxide on Modified Graphite Electrodes: Application to the Development of Glucose Biosensors. *Anal. Bioanal. Chem.* **2006**, *386* (5), 1413–1418.

(107) Sakslund, H.; Wang, J.; Lu, F.; Hammerich, O. Development and Evaluation of Glucose Microsensors Based on Electrochemical Codeposition of Ruthenium and Glucose Oxidase onto Carbon Fiber Microelectrodes. *J. Electroanal. Chem.* **1995**, *397* (1–2), 149–155.

(108) Degani, Y.; Heller, A. Electrical Communication between Redox Centers of Glucose Oxidase and Electrodes via Electrostatically and Covalently Bound Redox Polymers. *J. Am. Chem. Soc.* **1989**, *111*, 2357–2358.

(109) Rui, L. Energy Metabolism in the Liver. *Compr. Physiol.* **2014**, *4* (1), 177–197.

(110) Huang, X.-J.; Choi, Y.-K.; Im, H.-S.; Yarimaga, O.; Yoon, E.; Kim, H.-S.

Aspartate Aminotransferase (AST/GOT) and Alanine Aminotransferase (ALT/GPT) Detection Techniques. *Sensors* **2006**, *6* (7), 756–782.

(111) Mckenzie, J. R.; Cognata, A. C.; Davis, A. N.; Wikswo, J. P.; Cliffel, D. E. Real-Time Monitoring of Cellular Bioenergetics with a Multianalyte Screen-Printed Electrode. *Anal. Chem.* **2015**, *87*, 7857–7864.

(112) Zafar, M. N.; Wang, X.; Sygmund, C.; Ludwig, R.; Gorton, L. Electron-Transfer Studies with a New Flavin Adenine Dinucleotide Dependent Glucose Dehydrogenase and Osmium Polymers of Different Redox Potentials. *Anal. Chem.* **2012**, *84* (334–341), 334.

(113) Kober, E. M.; Caspar, J. V; Sullivan, B. P.; Meyer, T. J. Synthetic Routes to New Polypyridyl Complexes of Osmium(II). *Inorg. Chem.* **1988**, *27*, 4587–4598.

(114) Gunther, D.; LeBlanc, G.; Prasai, D.; Zhang, J. R.; Cliffel, D. E.; Bolotin, K. I.; Jennings, G. K. Photosystem I on Graphene as a Highly Transparent, Photoactive Electrode. *Langmuir* **2013**, *29* (13), 4177–4180.

(115) LeBlanc, G.; Winter, K. M.; Crosby, W. B.; Jennings, G. K.; Cliffel, D. E. Integration of Photosystem I with Graphene Oxide for Photocurrent Enhancement. *Adv. Energy Mater.* **2014**, *4* (9), n/a-n/a.

(116) Shao, Y.; Mirkin, M. V; Fish, G.; Kokotov, S.; Palanker, D.; Lewis, A. Nanometer-Sized Electrochemical Sensors. *Anal. Chem* **1997**, *69* (8), 1627–1634.

(117) Zoski, C. *Handbook of Electrochemistry*, 1st ed.; Elsevier, 2007.

(118) Li, Y.; Bergman, D.; Zhang, B. Preparation and Electrochemical Response of 1-3 Nm Pt Disk Electrodes. *Anal. Chem.* **2009**, *81* (13), 5496–5502.

(119) Katemann, B. B.; Schuhmann, W. Fabrication and Characterization of Needle-

Type. *Electroanalysis* **2002**, *14* (1), 22–28.

(120) Takahashi, Y.; Shevchuk, A. I.; Novak, P.; Zhang, Y.; Ebejer, N.; Macpherson, J. V; Unwin, P. R.; Pollard, A. J.; Roy, D.; Clifford, C. A.; et al. Multifunctional Nanoprobes for Nanoscale Chemical Imaging and Localized Chemical Delivery at Surfaces and Interfaces. *Angew. Chemie - Int. Ed.* **2011**, *50*, 9638–9642.

(121) McKelvey, K.; Nadappuram, B. P.; Actis, P.; Takahashi, Y.; Korchev, Y. E.; Matsue, T.; Robinson, C.; Unwin, P. R. Fabrication, Characterization, and Functionalization of Dual Carbon Electrodes as Probes for Scanning Electrochemical Microscopy (SECM). *Anal. Chem.* **2013**, *85*, 7519–7526.

(122) Michael, A. C.; Wightman, R. M.; Amatore, C. A. Microdisk Electrodes. Part I. Digital Simulation with a Conformal Map. *J. Electroanal. Chem. Interfacial Electrochem.* **1989**, *267*, 33.

(123) Lin, Y.; Trouillon, R.; Svensson, M. I.; Keighron, J. D.; Cans, A.-S.; Ewing, A. G. Carbon-Ring Microelectrode Arrays for Electrochemical Imaging of Single Cell Exocytosis: Fabrication and Characterization. *Anal. Chem.* **2012**, *84*, 2949–2954.

(124) Das, S. K.; Frank, H. A. Pigment Compositions, Cpectral Properties, and Energy Transfer Efficiencies between the Xanthophylls and Chlorophylls in the Major and Minor Pigment-Protein Complexes of Photosystem II. *Biochemistry* **2002**, *41* (43), 13087–13095.

(125) Mishra, R. K.; Ghanotakis, D. F. Selective Extraction of CP26 and CP29 Proteins Without Affecting the Binding of the Extrinsic Proteins (33, 23 and 17 kDa) and the DCMU Sensitivity of a Photosystem II Core Complex. *Photosynth.Res.* **1994**, *42*, 37–42.

(126) Lichtenthaler, H. K.; Buschmann, C. Chlorophylls and Carotenoids : Measurement and Characterization by UV-VIS. *Curr. Protoc. Food Anal. Chem.* **2001**, *F4.3.1-F4.* (Supplement 1), 1–8.

Appendix A

NANOELECTRODE FABRICATION

Introduction

Nanoelectrodes have become increasingly desirable for use in scanning electrochemical microscopy (SECM) based on their unequivocal ability to study ultrafast electrochemical reactions, elucidate heterogeneous electron transfer rate constants, probe cellular and subcellular systems, and image nanoscale environments with extremely high resolution.[116] Currently, only micron-sized (10 - 25 μm) ultramicroelectrode tips are commercially available for use in SECM applications, and although useful, are too large in diameter to effectively study systems at the single protein level. Any sub-micron sized electrodes (nanoelectrodes) must be fabricated and characterized in-house.

This Appendix describes techniques utilized to prepare a variety of nanoelectrode types, which can classified based on their core electrode material: platinum or carbon. The electrode material chosen for the nanoelectrode can offer greater versatility in application. For instance, carbon electrodes have a wider operational potential range, and are also more resistant to biofouling.[117] Thus carbon-based nanoelectrodes are most commonly used for biological applications that include *in vivo* ultrafast voltammetry of neurotransmitters, and imaging of single cells. Conversely, platinum electrodes have broad versatility in many other applications, and offer select advantages over their carbon counterparts. While protocols for fabricating carbon and platinum electrodes both rely on a laser puller, the ductility of platinum metal allows for much smaller electrode tips to be

fabricated (sub 10 nm), whereas carbon fibers are too brittle to be drawn below 1 μm. Typically, alternative methods are required to fabricate carbon nanoelectrodes (described below).

Laser pipette pulling is an effective strategy for drawing borosilicate and quartz capillaries to very fine tips. With this instrument, a CO_2 laser is focused through a parabolic mirror to uniformly heat a capillary. This capillary is secured to two pulling clamps on opposite ends, and once the glass is sufficiently softened, the pullers are activated and the capillary is rapidly drawn to a fine taper. The Sutter Instruments P-2000 laser puller allows for great user control in the resulting capillary taper by allowing independent inputs for heating power, the width of capillary that is heated, softness of the glass prior to pulling, delay time between heating pulling, and total pulling force.

For platinum electrodes, a platinum wire is first threaded through the capillary before pulling. However, in the case of carbon electrodes an empty capillary is pulled and tapered, and then backfilled with carbon to produce a conductive surface for electrochemistry. In the final step in electrode fabrication, the very finely tapered capillaries (filled with platinum or carbon) must be sealed within a larger glass body to provide structural support for later polishing and use.

The critical step for preparing Pt electrodes involves first threading a fine Pt filament though a very small quartz capillary, inserting this wired capillary into a slighting larger capillary, and then fusing the two hollow capillaries together, under heat and vacuum, to create a uniform, solid quartz body surrounding the wire. This entire process is referred to as the "sealing" step of fabrication, and is arguably most critical (Figure A.1).

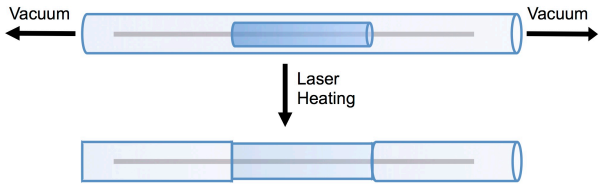

Figure A.1. Sealing of Platinum Wire for Fabrication of Platinum Nanoelectrodes. A fine platinum wire is threaded through a fine quartz capillary, and then into a larger quartz capillary. Vacuum is pulled from both ends of the larger capillary, and the center of the capillary is heated uniformly causing the overlapping quartz bodies to seal around the wire forming a solid wire/quartz assembly.

Following the sealing process, the fused capillary/Pt body is placed into the P-2000 laser puller, and pulling the activated to heat the capillary and wire uniformly and draw a fine taper and create a nanoelectrode. This method is very effective for platinum based electrodes based on the fortuitous matching of melting temperatures for quartz and platinum. The melting point for quartz is approximately 1700 °C, where as the melting point of platinum is 1768 °C. Thus when the temperature of a sealed quartz/platinum assembly approaches 1700 °C, the glass begins to soften as its melting point is reached, and the platinum becomes very ductile. Caution must be taken to not exceed the melting point of the platinum because this will cause the metal to liquefy and break. Alternatively, if a low melting point type of glass is used (i.e. borosilicate, MP = 820 °C), the glass will soften before the platinum is ductile enough to be pulled, and the wire will snap upon pulling.

Carbon as material is very brittle, and lacks ductility. Thus carbon filaments cannot be pulled to a taper using the same methods for platinum. For a carbon nanoelectrode, an empty quartz capillary is pulled to a fine taper, then a hydrocarbon gas is flowed through the capillary exiting through the taper. A handheld butane torch is then applied to the outside of the taper, heating the quartz capillary but not melting it, such

that the internal hydrocarbon gas decomposes (Figure A.2). This process fills in the inside walls of the capillary with graphitic carbon and eventually seals the capillary the very fine tapered end producing a nanoelectrode with fixed dimensions defined by the capillary taper.

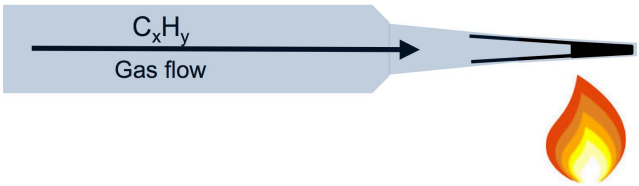

Figure A.2. Flame-assisted Carbon Nanoelectrode Fabrication. A hydrocarbon gas is flowed through a tapered quartz capillary being heated on the outside by a handheld butane torch. The anaerobic environment inside the capillary leads to thermal decomposition of the gas into conductive carbon, which plugs the taper and creates a sealed nanoelectrode.

The next step of preparing useable nanoelectrodes requires sealing the tapered capillaries within larger glass capillaries for structural support. This can be accomplished in a variety of ways; however, this task is non-trivial. The outside capillary must be carefully heated such that only it softens and seals around the taper under vacuum without melting the inner taper of electrode material. Using this strategy, the same glass type must be used for the sealing process, i.e. quartz on quartz, because mismatched materials (i.e. borosilicate on quartz) will lead to fracturing of the electrode body upon cooling due to thermal expansion coefficient disparity.

A new strategy was developed herein to seal the tapered nanoelectrodes within larger borosilicate capillaries using a high-grade insulating epoxy that upon curing has hardness and transparency similar to glass. This strategy avoids unnecessary heating and preserves the integrity of the nanoelectrode.

Specific procedures for pulling, sealing, polishing, and characterizing platinum

and carbon nanoelectrodes are presented in in detail in this Appendix.

Experimental

Platinum Nanoelectrodes

The fabrication of platinum nanoelectrodes has been previously described in a variety of publications,[116,118,119] all with minor procedural differences. Briefly, a 3 cm long segment of 25 μm platinum wire (Goodfellow, USA) was threaded through a fine capillary electrophoresis quartz tube (Polymicro Technologies) (I.D. = 75 μm, O.D. = 365 μm), cut to 1.5 cm long, and this threaded capillary was carefully centered in a larger quartz capillary (I.D. = 0.4 mm, O.D. = 1.2 mm) (Sutter Instruments).

This assembly was then loaded into the P-2000 laser puller and aligned such that the inner quartz tube and wire were precisely centered within the laser focus. The ends of the capillary were secured in the puller bars; however the puller bars were locked in place such that no physical pulling would be activated when the glass was heated. The capillary was heated using the parameters of Heat 800, Filament 3, Velocity 1, Delay 0, and Pull 0. This heating cycle was performed on the same capillary for 90 seconds, followed by 20 seconds off. This process was repeated 3 times to ensure proper sealing of the quartz/Pt microform. An image of this sealed microform is pictured in Figure A.3.

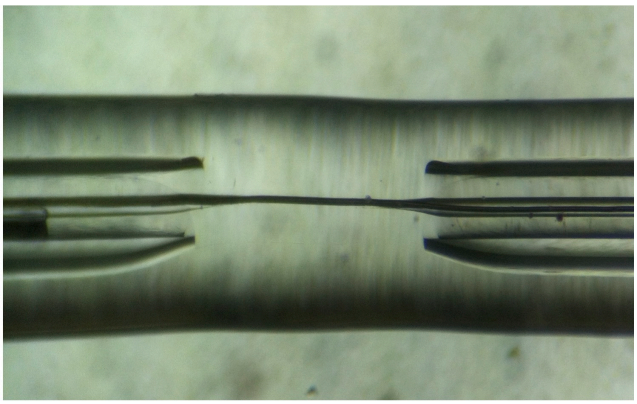

Figure A.3. Sealed Quartz/Platinum Microform. A 25 μm platinum wire is sealed within two nested quartz capillaries that were fused together under heating and vacuum.

Following the sealing process, the microform was reloaded into the P2000, and a pull sequence was carried out using the parameters: Heat 950, Filament 1, Velocity 30, Delay 100, and Pull 220. A sample of the platinum nanoelectrodes pulled using these parameters is shown in Figure A.4.

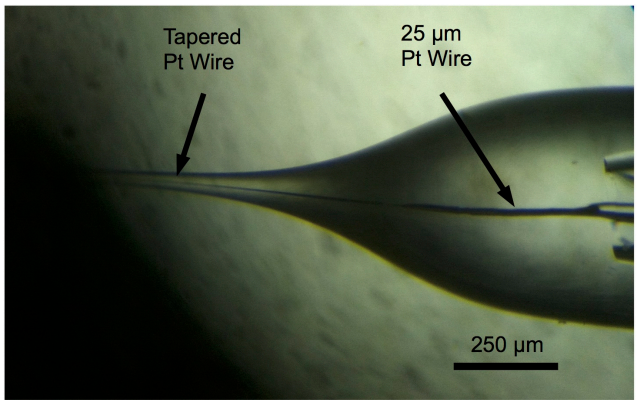

Figure A.4. Micrograph of Tapered Platinum Wire after Laser Pulling. A pulled platinum wire is shown sealed in quartz after activating a laser-heated pull sequence.

After pulling, the two new quartz/Pt tapers were removed from the pullers and visualized under stereoscope magnification. During this time the tapers were inspected for visible breaks in the Pt wire that might have occurred during the heating process. Using the untapered 25 μm wire as a reference, the diameter of the newly formed tapered wire can be estimated. This taper continues to decrease in size as a function of distance

pulled until it reaches a small enough diameter which can no longer be resolved with optical microscopy. As pictured in Figure A.4, the taper appears to be far below 1 μm in diameter, and continually decreases until it can no longer be seen.

Following visual inspection, the tapered microform was sealed into a larger capillary (Sutter Instruments, borosilicate, I.D./O.D. = 1.56/2.0 mm). The outer capillary was first sealed at one end using a standard laboratory flame. While held in an upright position with the closed end pointed downward, a very small volume of uncured epoxy (Epotek™ 301) was added, and the tapered microform was added. It is essential to use just enough epoxy to cover the delicate tapered region of the microform and some of the unpulled capillary, but not cover the open, backend of the microform, as this must be later accessed to make electrical contact with the tip. The capillary/microform conjugate was left undisturbed for 4 h at room temperature to let the epoxy set, and then moved to a 100 °C oven to fully cure overnight.

Epotek 301 was specifically chosen for this application. It is an ideal adhesive material with extremely high transmittance, so that the electrode wire may be visualized through the outer capillary, and also when fully cured, the epoxy has extremely high hardness. The hardness is key due to the polishing steps required later to expose the Pt tip. The epoxy is very glass like when fully cured, and also is electrically insulating.

A fine wire was threaded into the back of the inner capillary along with a small amount of conductive silver epoxy. Once set, this epoxy was cured at 100 °C overnight to secure a robust electrical contact with the inner 25 μm Pt wire, and subsequent nanoelectrode tip.

The nanoelectrode was exposed by grinding the closed end of the borosilicate

capillary using a series of wet sandpapers on a polishing wheel in descending roughness. Great care was taken to only expose the very tip of the Pt nanoelectrode, as polishing too far back would increase the diameter of the exposed disk. Finally, fine polishing was performed using a series of alumina powders ranging from 1 μm down to 0.05 μm.

Carbon Nanoelectrodes

Carbon nanoelectrodes were fabricated using the previously devised methods of Takahashi et al.,[120] and McKelvy et al.,[121] with minor modifications. In short, a quartz capillary (I.D. = 0.4 mm, O.D. = 1.2 mm) was pulled in the P-2000 laser puller using the parameters; Heat 760, Filament 3, Velocity 20, Delay 100, and Pull 150. One of the two resulting tapered capillaries were capped with small diameter Tygon tubing on the unpulled end. The Tygon tubing was connected to an ethylene tank, regulated such that very minimal flow was passing through the capillary and exiting through the open taper.

A handheld butane torch was held up to the tip of the capillary and a bright orange glow from inside the quartz was observed. This process is pictured in Figure A.5.

Figure A.5. Thermal Deposition of Pyrolytic Carbon in a Pulled Quartz Electrode. A handheld butane torch was used to gently heat the ethylene gas flowing inside the pulled capillary such that decomposition of the ethylene deposits thin layers of pyrolytic carbon.

This indicates the decomposition, not combustion, of the ethylene gas. This heating continued for 3-5 minutes to ensure that the open taper was completely sealed with pyrolytic carbon. The carbon/quartz microform was sealed within a larger borosilicate capillary identical to the platinum nanoelectrodes described in the previous section. Polishing was performed using a series of sandpapers on a polishing wheel to expose the carbon disk. Final polishing was accomplished using a series of alumina powders is descending sizes.

Results and Discussion

With electrode diameters less than 1 μm, the traditional method for sizing electrodes (i.e. optical microscopy) becomes ineffective. In such a case, cyclic voltammetry is used to characterize the newly fabricated electrodes. This technique actually provides several key diagnostics for the system. First, that the electrode is conductive, without any breaks in the wire from the electrical contact wire, silver epoxy, and finally to the platinum or carbon at the electrode tip. Second, the shape of the voltammogram will indicate any irregularities in electrode geometry. In bulk solution, a planar disk nanoelectrode should produce a voltammogram without a mass-transfer limited region, as the dimensions of the electrode are smaller than the diffusion plane of the analyte. Instead kinetically limited steady-state current regions are observed as the applied potential of the electrode is swept past the reduction potential of the analyte. Deviations from the flat plateau regions may indicate a recessed or "lagooned" tip buried within the glass that is blocking free diffusion of analyte. Finally, the steady-state tip current observed in a bulk solution of a reversible redox probe, such as RuHex, will behave according to Equation A.1[74]

$$I_{t,\infty} = 4nFD_O C_O^* a \quad \text{(A.1)}$$

Where $I_{T,\infty}$ is the current when the tip is submerged in bulk solution of a redox active compound (O) with unrestricted hemispherical diffusion. The variable n represents the number of electrons associated with the redox process; for hexammineruthenium(III) (RuHex) n = 1. F is Faraday's constant, D_0 is the diffusion coefficient of O (0.53 x 10^{-5} cm^2 s^{-1}),[122] and C_0^* is the bulk concentration of species O. Finally, "a" represents the radius of the electrode. Thus using Equation A.1, the size of a nanoelectrode can be determined from a voltammogram collected in a standard solution of redox probe.

For a platinum nanoelectrode fabricated using the methods described above, this analysis was carried out in a 2 μM solution of $Ru(NH_3)_6^{3-}$, and the cyclic voltammogram was collected from +0.3 to -0.4 V.

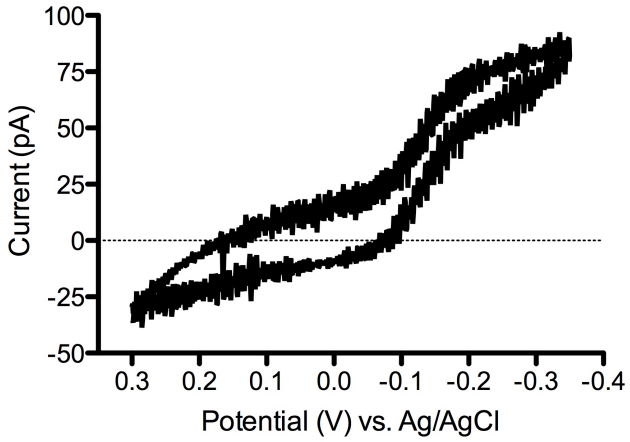

Figure A.6. Size Determination of Platinum Nanoelectrode by Cyclic Voltammetry. The newly fabricated platinum nanoelectrodes were tested in a 2 μM solution of RuHex. This successful CV indicates that there are no breaks in the wire from contact to nanoelectrode tip, and that the electrode is a polished disc without any major geometric aberrations. Additionally, the peak current, 51 pA at -0.2 V, was used for the direct determination of the working electrode size.

Via Equation A.1, the peak current (51 pA) and all known constants were used to calculate the radius of this platinum nanoelectrode as 130 nm. Qualitatively, it was all

inferred that the geometry of the electrode is mostly disk-shaped, based on the appearance of the voltammogram in Figure A.6. This analysis confirms the successful fabrication of platinum nanoelectrodes with submicrometer dimensions. Future studies will seek further optimization in pipet pulling to produce smaller tapers, as well as more delicate polishing and beveling using a Sutter Instrument BV-10 Beveler with integrated impedance meter.

Carbon electrodes were characterized using similar method to the platinum. However, these electrode sizes were considerably larger than their platinum counterparts. These electrodes typically range in diameter from 5 - 0.5 μm. Further optimization must be performed in order to produce true carbon nanoelectrodes.

Conclusions and Future Directions

In this Appendix, methods were described for the in-house fabrication of carbon and platinum nanoelectrodes. A platinum nanoelectrode was prepared and characterized with cyclic voltammetry to verify its nanoscale dimensions with an electrode radius of 130 nm. Further optimization will be performed to further decrease the size of the carbon and platinum nanoelectrodes.

The methods described herein also introduce future opportunities to develop multifunctional SECM tips with nanoscale dimensions. Using commercially available capillaries with segregated chambers, such as theta tubes, multiple nanoelectrodes could be pulled from the same capillary to produce a single glass tip with multiple channels. This was first successfully showcased through the creation of a pulled theta tube in which one of the chambers was backfilled with carbon, and the other left vacant for a hybrid Scanning Electrochemical/Scanning Ion Conductance Microscopy technique.[120] Later this

technique was adapted to separately prepare isolated carbon electrodes in a tapered theta tube, in which the two distinct channels were used for a Tip-Generator/Tip-Collector application.[121]

This strategy was largely possible due to the nature of automated laser-heated pipet pulling. One hallmark of this instrument is the retention of I.D./O.D. ratio after pulling. That is, the ratio of inner and outer diameters is conserved between the pulled taper end and the unpulled glass end. Thus, it was hypothesized that a multibarrel quartz capillary (greater than 2 chambers) could be pulled with the P-2000 laser puller and all capillaries would be tapered without losing the individual chamber isolation. Preliminary experiments, shown in Figure A.7, support this hypothesis.

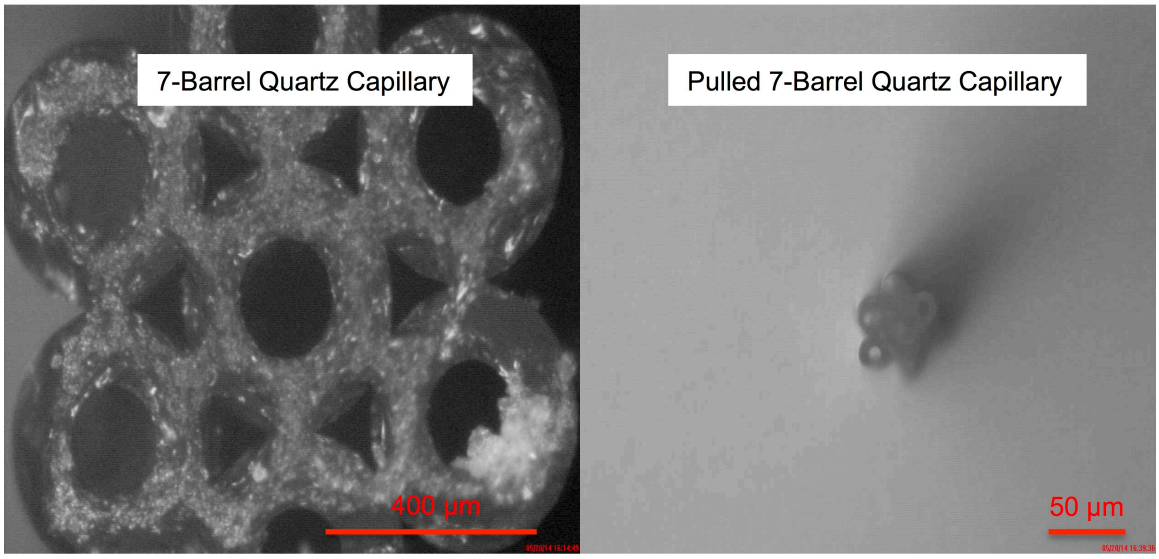

Figure A.7. Micrograph of Tapered Multibarrel Quartz Capillary. Multibarrel capillary is shown as received (left), and pulled with laser puller (right). The taper still maintains the multibarrel integrity as all independent chambers remain open and not fused.

The multibarrel quartz pipet (Sutter Instruments, 7 barrels, each barrel I.D./O.D. = 0.33/0.16 mm), was loaded into the P-2000 and pulled with the parameters of Heat 760, Filament 3, Velocity 20, Delay 100, and Pull 150. There is a clear reduction in size of

each capillary, as each inner capillary was reduced to a sub 10 μm diameter. Although, capillary bundles have been formed into multichannel SECM tips to monitor cellular exocytosis of single neuron-type cells,[123] this would be the first instance of a multibarrel SECM tip prepared using this method. This methodology with minimal optimization would provide sufficiently smaller individual electrode tips, while also affording greater reproducibility in fabrication.

With these new multibarrel electrodes, a variety of electrochemical experiments could now be enhanced through SECM. In particular, multianalyte monitoring in real time of individual cells can be accomplished with ease. Fabrication and modification of these multifunctional tips represent a powerful new tool for probing complex electrochemical systems.

Appendix B

PHOTOSYSTEM II EXTRACTION AND CHARACTERIZATION

Introduction

Photosystem II (PSII) is another key component in photosynthesis that acts in tandem with PSI. In Nature, PSII is responsible for the water splitting reactions of photosynthesis. Based on the large oxidizing potential produced by this photoactive protein, which is required to split water molecules, this protein supercomplex has attracted significant attention from researchers as a component that can be integrated into biophotovoltaics or used on the anodic side of biohydrogen fuel cells. This Appendix describes a general procedure for the extraction of PSII from spinach leaves, and also simple characterization performed on the extracted protein.

Experimental

Photosystem I (PSII) Extraction

PSII was extracted from spinach leaves using a procedure adapted from Das and Frank (2002),[124] and Mishra and Ghanotakis (1994).[125]

169 g of spinach leaves were deveined and ground into a puree in 250 mL of Grinding Medium (20 mM HEPES pH 7.6, 0.4 M NaCl, 4 mM $MgCl_2$, 5 mM EDTA, and 1 mg/mL BSA). The solution was twice filtered through cheesecloth and divided into six centrifuge tubes. This was centrifuged at 6000 x g for 8 min to precipitate chloroplasts. This pellet was washed in Wash Buffer (20 mM HEPES pH 7.6, 0.15 M NaCl, 4 mM $MgCl_2$, 1 mM EDTA, and 1 mg/mL BSA), and then centrifuged again at 500 x g for 30 s.

The supernatant containing solubilized chloroplasts was collected and centrifuged at 7,000 x g for 10 min.

The pellet was collected in EG Buffer (20 mM MES pH 6.0, 30% (v/v) ethylene glycol, 15 mM NaCl, 5 mM $MgCl_2$, 1 mM EDTA, and 1 mg/mL BSA) and centrifuged at 12,000 x g for 10 min. The pellet was resuspended in EG Buffer and centrifugation was repeated again to open the chloroplasts and precipitate thylakoid membranes. The precipitated thylakoid membranes were resuspended in a minimal amount of EG Buffer and the chlorophyll (Chl) concentration was determined using UV-Vis. Using 80:20 acetone:water as the solvent, the absorbance values at 663 nm and 646 nm were used to determine the total chlorophyll concentration in the sample following published values for Chl a and Chl b molar absorptivities.[126] Suspension Buffer (20 mM MES pH 6.0, 15 mM NaCl, and 30% (v/v) ethylene glycol) was used to dilute the thylakoid solution according to the equation below:

$$\left(\frac{3}{8}[Chl\ (mg\ mL^{-1})] - 1\right)\ x\ vol.of\ Thylakoid\ Sol.\ (mL) = vol.of\ Suspension\ Buffer\ to\ add\ (mL) \quad \text{(B.1)}$$

Triton X-100 was also added to the solution to open the thylakoid membranes by surfactant-based lysis. Triton X-100 Buffer (20 mM MES pH 6.0, 15 mM NaCl, 5 mM $MgCl_2$, 1 mM EDTA, 1 mg/mL BSA, and 20% (v/v) Triton X-100) was added according to the equation below:

$$\frac{[Chl\ (mg\ mL^{-1}]}{8}\ x\ vol.of\ Thylakoid\ Solution\ after\ Dilution = vol.of\ Triton\ X-100\ Buffer\ to\ add\ (\text{mL}) \quad \text{(B.2)}$$

Triton X-100 Buffer was added in small aliquots while the thylakoid solution incubated on a shaker rack. After incubating for 20+ min, the solution was centrifuged for

20 min at 37,000 x g. The pellet was resuspended in SMN Buffer (50 mM MES pH 6.0, 0.4 M sucrose, and 10 mM NaCl) and centrifuged again at 37,000 x g for 20 min to precipitate the PSII enriched BBY membranes. The resulting pellet was resuspended in SMN Buffer w/ OTG (50 mM MES pH 6.0, 0.4 M sucrose, and 10 mM NaCl, and 0.4% (w/v n-octyl-β-d-thioglucopyranoside) in order to solubilize individuals PSI complexes.

The resulting solution was characterized by UV-Vis to determine the chlorophyll concentration which was then diluted to 0.5 mg/mL Chl total with SMN Buffer w/ OTG and incubated in the dark at 4° C for 10 min. This was then centrifuged at 40,000 x g for 10 min. The supernatant, containing solubilized PSII core complexes, was then diluted by 50% with SMN Buffer w/ $MgCl_2$ (50 mM MES pH 6.0, 0.4 mM sucrose, 10 mM NaCl, and 30 mM $MgCl_2$). This was then incubated for 5 min, and centrifuged at 40,000 x g for 20 min. The supernatant was collected, after the free LHC-II complexes were precipitated, and the supernatant was diluted with an equal volume of PEG Buffer (50 mM MES pH 6.0, and 20% (w/v) polyethylene glycol $M_n \approx 6{,}000$).

This solution was centrifuged a final time at 40,000 g for 30 min to precipitate the desired PSII-LHC-II complexes. The final pellet was suspended in Suspension Buffer and stored at -80° C in 1 mL aliquots for later use.

PSII Oxygen Evolution Assay

The oxygen evolution activity was measured for the extracted PSII in order to determine the viability of this protein and verify the presence of active OECs in the PSII supercomplex. This assay was performed by combining 2 mL of PSII with 33 mL of assay buffer (20 mM MES pH 6.0, 10 mM $CaCl_2$, 10 mM $MgCl_2$). Ferricyanide was added as an electron acceptor to the PSII solution to a final concentration of 1 mM. A stir

bar was added to this assay solution, then N_2 was purged through the PSII solution, and a Clark-type dissolved oxygen sensor was sealed over the top of the apparatus.

Dissolved oxygen measurements were recorded every 2 min over the course of the 50 minute experiment. The samples were kept in the dark for the first 10 minutes, then illuminated with red light (>633 nm cutoff) for 30 min, and then returned to the dark for the final 10 minutes.

Results and Discussion

Polyacrylamide Gel Electrophoresis

PSII extracted using the methods presented in this Appendix were analyzed by SDS-PAGE in order to identify the presence of certain polypeptide subunits. 8-12% Bis-Tris NuPage™ precast gel cassettes (Invitrogen) were used in MES running buffer. Commassie staining was performed to reveal the isolated protein bands. Presented in Figure B.1 is the subunit separation performed by SDS-PAGE.

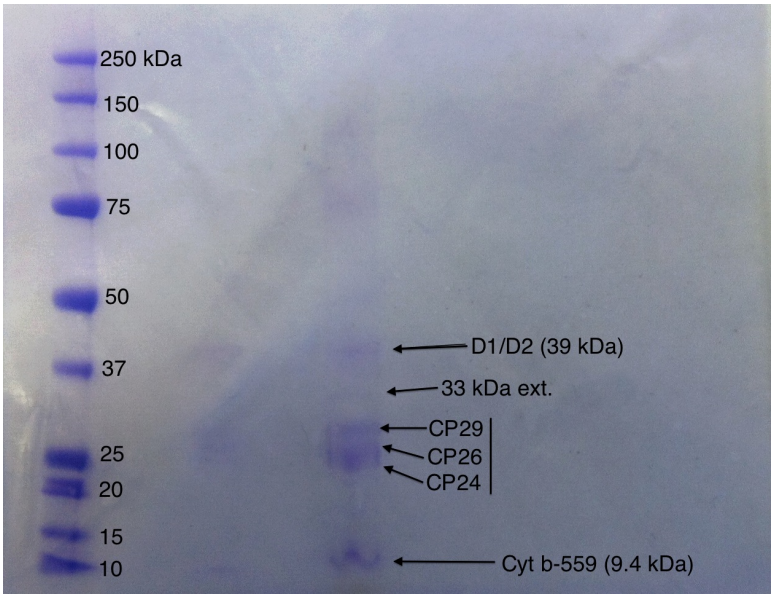

Figure B.1. SDS-PAGE of PSII Extracted from Spinach Leaves. Polypeptide subunits typical of PSII are presented in the commassie stained gel.

From Figure B.1, the bands corresponding to the D1/D2 heterodimer of PSII are found near 40 kDa. Other smaller chlorophyll-containing polypeptide subunits of the PSII supercomplex are present, i.e. CP29, CP26, CP24. This analysis indicates the successful collection and purification of PSII.

Oxygen Evolution Assay

Additional characterization of the extracted PSII was performed by measuring photoactivated oxygen evolution from the sample. An increase in dissolved oxygen for a PSI sample during a period of illumination indicates catalytic water splitting, and thus intact Mn_4Ca_5O oxygen-evolving centers.

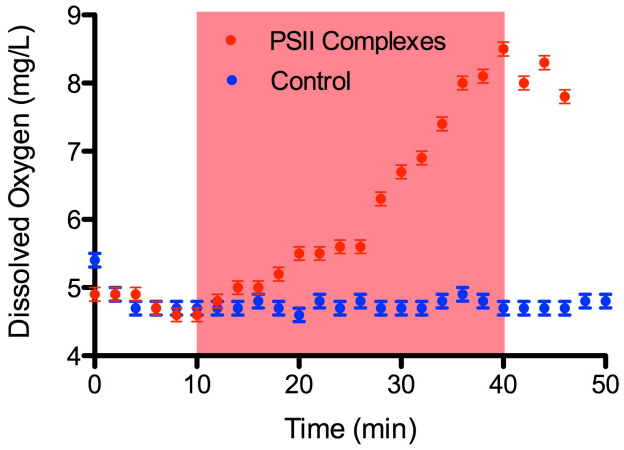

Figure B.2. **Oxygen Evolution Assay for Extracted PSII**. The water splitting activity of PSII was evaluated using an oxygen evolution assay using a Clark-type electrode. 1 mM ferricyanide was used as the electron acceptor in this assay.

From Figure B.2, the increase in dissolved oxygen can be seen during periods of illumination, from 20-40 min. A negative control containing only buffer and ferricyanide was used for comparative purposes (blue). The dissolved oxygen detected in the PSII sample (red) increased dramatically under red light illumination. A linear relationship in this oxygen concentration was identified and the slope of this plot from 20-40 min was calculated to be 0.135 ± 0.009 mg O_2 L^{-1} min^{-1}. With a concentration of 0.008789 mg

mL^{-1} Chl in the final diluted assay solution, the rate of oxygen evolution was can be normalized to value of 28.8 μmol h^{-1} mg Chl^{-1}. Although this value is much lower than typically obtained oxygen evolution rates for PSII harvest elsewhere, this data still indicates the presence of active PSII supercomplexes with intact oxygen evolving centers.

Evan A. Gizzie

Curriculum Vitae

7330 Stevenson Center Ln
Vanderbilt University
Nashville, TN 37235-1822
(615) 322-5013 (Office/Lab)
(561) 305-8556 (Cell)
evan.a.gizzie@vanderbilt.edu

Education

Vanderbilt University — Nashville, TN
Ph.D. Chemistry — December 2016 (Expected)

University of Central Florida — Orlando, FL
B.S. Chemistry with Biology Minor — May 2011

Research Experience

Graduate Research Assistant, Vanderbilt Univ. — August 2011 - Present
Advisor: Prof. David E. Cliffel

Thesis: *Enhancing Electron Transfer at the Protein-Electrode Interface: Applications in Bioderived Solar Energy Conversion and Electrochemical Biosensors*

Principal Research Efforts:

- Developed a novel organic polymer-protein composite material, for low-cost, scalable solar energy conversion.
- Created new *in situ* method for orienting photosynthetic proteins on electrodes surfaces for enhanced light harvesting and photocurrent generation.
- Constructed enzymatic biosensor platform for metabolite sensing in acetaminophen-rich, *in vitro* liver-on-chip systems.

Technical Expertise:

- Surface analysis, electroanalytical techniques; optical spectroscopies (e.g. UV-Vis/fluorescence, FT-IR, Raman); spectroscopic ellipsometry; atomic emission spectroscopy; sensor/assay development; bioconjugation; surface functionalization; scanning probe methods (e.g. AFM, STM); thin-film deposition; nanomaterial syntheses; protein extraction, purification and characterization; mass spectrometry (MALDI-TOF and ESI); transition metal complex synthesis and purification; ^{1}H-NMR and ^{13}C-NMR; HPLC, column, and TLC-based separations.

Undergraduate Research Assistant, UCF — August 2010 – May 2011
Advisor: Prof. Diego J. Diaz

Principal Research Efforts:

- Electrochemical quartz crystal microbalance studies on the long-term performance of novel platinum nanoparticle catalysts and membranes in direct methanol fuel cells.

Evan A. Gizzie

Curriculum Vitae

Industrial Experience

Chemical Analyst – Student Intern — Lockheed Martin MFC, Orlando, FL
Printed Wiring Technology Laboratory — February 2008 – December 2010

Principal Responsibilities:

- Worked closely with prototype engineers to manufacture circuit boards under strict delivery deadlines. Manufacturing tasks included: photolithography, electrolytic and electroless plating, hydrogen fluoride and/or ammoniacal etching, and QC.
- Analyzed and maintained various chemical processing baths used in the electrochemical plating of prototype circuit boards.
- Managed packaging, inventory, and handling of industrial chemical waste products.

Leadership Experience

Community Outreach:

Vanderbilt Summer Academy – Demo Leader — June 2013 – 2016

Lead various hands-on demonstrations with middle school students, in which students assembled hydrogen fuel cell powered model cars, or synthesized colloidal gold nanoparticles in varying sizes.

VINSE High School Field Trips – Demo Leader — March 2013 – March 2015

Guided high school chemistry students during a visit to Vanderbilt, and worked with teams of students to construct simple dye-sensitized solar cells by extracting photoactive pigments from blackberries

Mentoring Experience:

Graduate Student Mentor – High School Student — August 2015 – May 2016

Worked with a High School senior from Franklin High School (Franklin, TN) to extract photosynthetic proteins and construct a low cost solar cell using only "high school level" expertise. The results from this work are currently being prepared into an instructional demo that will be disbursed to local High School science teachers, and subsequently submitted to *J. Chem. Ed.*

Research Experience for Undergrads (REU) — Summer 2013 - Present

Served as graduate student mentor to 4 undergraduate students placed in the Cliffel research lab, through the Research Experience for Undergrads (REU) program, over the course of three summers. Through this program, students with little or no research experience were exposed to life in academic research labs. Mentoring involved intensive training of students in proper use of the scientific method, inquiry-based research, hypothesis formation/testing, and experimental design, as well as technical training on effective laboratory techniques and instrument usage.

Graduate Student Mentor – Vanderbilt Students — Spring 2013 - Present

Mentored 3 different Vanderbilt undergraduate chemistry students with their various independent research projects while in the Cliffel group.

Honors and Awards

- Vanderbilt University Frederic LeRoy Conover Graduate Research Fellowship (Summer 2015)

- Vanderbilt University Mitchum E. Warren Graduate Research Fellowship (Spring 2015)
- Artwork featured on the cover of Langmuir Vol. 35, Issue 37 (September 2014)
- Student Travel Grant, 224th Electrochemical Society Meeting, San Francisco, CA, Sponsored by the ECS Physical and Analytical Electrochemistry Division (November 2013)
- Dean's List, University of Central Florida (Spring 2008, Fall 2009)
- President's Honor Roll, University of Central Florida (Fall 2007)
- Pegasus Bronze Scholarship, University of Central Florida (Fall 2007)
- Florida Bright Futures Scholarship (Fall 2007 – Spring 2011)

Society Memberships and Professional Affiliations

- Vanderbilt Institute for Integrative Biosystems Research and Education (VIIBRE) (2012-Present)
- Vanderbilt Institute of Nanoscale Science and Engineering (VINSE) (2011-Present)
- Society of Electroanalytical Chemistry (2013-2015)
- Electrochemical Society (2011-2015)
- American Chemical Society (2009-2015)

Workshops, Short Courses, and Other Continuing Education

- Roundtable Research Discussion with Prof. Jeremy Nicholson, Imperial College of London. Sponsored by the Warren Endowment Lecture Series. Vanderbilt University, Nashville, TN. November 9, 2015.
- *Federal STEM Policy & Advocacy: an Inside the Beltway Look.* Sponsored by the Vanderbilt University Office of Federal Relations. Washington D.C. October 15-16, 2015.

Presentations

10. "An Electrochemical Platform for Real-Time Metabolic Profiling in Liver-on-Chip Systems" Poster Presentation. Southeast/Southwest Joint Regional Meeting of the American Chemical Society. Memphis, TN. October 4, 2015.
9. "Strategies for Constructing Solid-State PSI-based Solar Energy Conversion Devices" Poster Presentation. TN-SCORE 2015 Annual Meeting. Nashville, TN. June 18, 2015.
8. "Side-Selective Modification of Photosynthetic Proteins for Highly Oriented Active Layers in Biological Solar Energy Conversion Applications" Oral Presentation. Pittcon 2015. New Orleans, LA. March 10, 2015.
7. "Development of an acetaminophen-insensitive, amperometric, multianalyte biosensor for liver-on-a-chip platforms" Poster Presentation. Southeast Regional Meeting of the American Chemical Society. Nashville, TN. October 17, 2014.
6. "Electrochemical Studies of Photosystem I/Polymer/Semiconductor Interfaces for Biohybrid Solar Energy Conversion" Oral Presentation. Pittcon 2014. Chicago, IL. March 5, 2014.

5. “Electrochemical Preparation of Polyaniline-Photosystem I Composite Films for Biohybrid Solar Energy Conversion.” Poster Presentation. 14th Annual VINSE Nanoscience and Nanotechnology Forum. Nashville, TN. November 13, 2013.
4. “Electrochemical Preparation of Polyaniline-Photosystem I Composite Films for Biohybrid Solar Energy Conversion.” Poster Presentation. 224th Meeting of the Electrochemical Society. San Francisco, CA. October 30, 2013.
3. “Immobilization of Photosystem I within Conductive Polyaniline Networks via Electrochemical Polymerization.” Poster Presentation. TN-SCORE 2013 Annual Meeting. Nashville, TN. June 10, 2013.
2. “Entrapment of Photoactive Proteins in Conductive Thin-Film Polymer Networks.” Oral Presentation. Pittcon 2013. Philadelphia, PA. March 19, 2013.
1. "Synthesis of Thin Films of MBx on Hard and Soft Supports by CPCD and Liquid Reduction of PbPt Catalysts for DFAFC" Poster Presentation. TN-SCORE Thrust 2 meeting. June 14, 2011.

Invited Symposia

3. “Fostering Interdisciplinary Collaboration: a Comprehensive Guide to Establishing Successful Scientific Relationships” Vanderbilt University Chemistry Forum Seminar Series. Nashville, TN. October 8, 2015.
2. “Photosystem I – Polyaniline Composites: New Materials for Solid-State Biohybrid Solar Energy Conversion” Vanderbilt Institute of Nanoscale Science and Engineering (VINSE) Summer NanoSeminar. Nashville, TN. June 12, 2015.
1. “Electrochemical Preparation of Polyaniline-Photosystem I Composite Films for Biohybrid Solar Energy Conversion” ECS Electrochemical Energy Summit (E2S). San Francisco, CA. October 27, 2013.

Publications:

Refereed Publications:

7. Gizzie, E. A.; Cliffel, D. E. “An Acetaminophen Insensitive, Amperometric, Multianalyte, Biosensor for Liver-on-Chip Platforms” Analytical Chemistry **2016**, *In Preparation*.
6. Gizzie, E. A.; Niezgoda, J. S.; Robinson, M. T.; Harris, A. G.; Jennings, G. K.; Rosenthal, S. J.; Cliffel, D. E. “Photosystem I-Polyaniline/TiO_2 Solid-State Solar Cells: Simple Devices for Biohybrid Solar Energy Conversion” Energy & Environmental Science **2015**, 8, 3572.
5. Beam, J. C.; LeBlanc, G.; Gizzie, E. A.; Ivanov, B. L.; Needell, D. R.; Shearer, M. J., Jennings, G. K.; Lukehart, C. M.; Cliffel, D. E. “Construction of a Semiconductor-Biological Interface for Solar Energy Conversion: p-doped Silicon/Photosystem I/Zinc Oxide” Langmuir **2015**, 31, 10002.
4. Gizzie, E. A.; LeBlanc G.; Jennings. G. K.; Cliffel, D. E. “Electrochemical Preparation of Photosystem I-Polyaniline Composite Films for Biohybrid Solar Energy Conversion” ACS Applied Materials and Interfaces **2015**, 7, 9328.
3. Darby, E.; LeBlanc, G.; Gizzie, E. A.; Jennings. G. K.; Cliffel, D. E. "Photoactive Films of Photosystem I on Transparent Reduced Graphene Oxide Electrodes" Langmuir **2014**, 30, 8990.

2. LeBlanc, G.; Gizzie, E. A.; Yang, S.; Jennings, G. K. "Photosystem I Protein Films at Electrode Surfaces for Solar Energy Conversion" Langmuir **2014**, 30, 10990.
1. LeBlanc, G.; Chen, G.; Gizzie, E. A.; Jennings, G. K.; Cliffel, D. E. “Enhanced Photocurrents of Photosystem I Films on p-Doped Silicon” Advanced Materials **2012**, 24, 5959.

Published Proceedings:

1. Gulka, C. P.; Gizzie E. A.; Cliffel, D. E.; Wright, D. W. “Electrochemical Detection of 2,4,6-Trinitrotoluene at Colloidal Gold Nanoparticle Film Assemblies” In Nanotechnology to Aid Chemical and Biological Defense; NATO Science for Peace and Security Series A: Chemical and Biology; Camesano, T. A., Ed.; Springer Netherlands, **2015**; pp 147-160.